

May 2018

A Numerical Model of an Axial Wind Turbine

Andrew Liam Poland
polanda@unlv.nevada.edu

Follow this and additional works at: <https://digitalscholarship.unlv.edu/thesesdissertations>

 Part of the [Mechanical Engineering Commons](#)

Repository Citation

Poland, Andrew Liam, "A Numerical Model of an Axial Wind Turbine" (2018). *UNLV Theses, Dissertations, Professional Papers, and Capstones*. 3311.
<https://digitalscholarship.unlv.edu/thesesdissertations/3311>

This Thesis is brought to you for free and open access by Digital Scholarship@UNLV. It has been accepted for inclusion in UNLV Theses, Dissertations, Professional Papers, and Capstones by an authorized administrator of Digital Scholarship@UNLV. For more information, please contact digitalscholarship@unlv.edu.

A NUMERICAL MODEL OF AN AXIAL WIND TURBINE

By

Andrew Poland

Bachelor of Science in Engineering – Mechanical Engineering
University of Nevada, Las Vegas
2014

A thesis submitted in partial fulfillment
of the requirements for the

Master of Science in Engineering – Mechanical Engineering

Department of Mechanical Engineering
Howard R. Hughes College of Engineering
The Graduate College

University of Nevada, Las Vegas
May 2018



Thesis Approval

The Graduate College
The University of Nevada, Las Vegas

April 11, 2018

This thesis prepared by

Andrew Poland

entitled

A Numerical Model of an Axial Wind Turbine

is approved in partial fulfillment of the requirements for the degree of

Master of Science in Engineering – Mechanical Engineering
Department of Mechanical Engineering

Yi-Tung Chen, Ph.D.
Examination Committee Chair

Kathryn Hausbeck Korgan, Ph.D.
Graduate College Interim Dean

Hui Zhao, Ph.D.
Examination Committee Member

William Culbreth, Ph.D.
Examination Committee Member

Jichun Li, Ph.D.
Graduate College Faculty Representative

Abstract

A NUMERICAL MODEL OF AN AXIAL WIND TURBINE

By

Andrew Poland

Dr. Yi-Tung Chen, Committee Chair

Professor of Mechanical Engineering

University of Nevada, Las Vegas

Since the beginning of the industrial revolution, there has never been more of a constant in the world than that of the demand for energy. For years a stable source has been fossil fuels, but with the growing impacts of global warming, it is important to look for renewable sources. Wind energy's use has become more and more prevalent throughout the world.

This preliminary work runs through the creation of a three-dimensional numerical model of a conventional wind turbine that was created using ANSYS-Fluent[®] commercial software. This work provides the base wind turbine and a blade element and momentum theory (BEMT) based MATLAB[®] code that can create the blade coordinates if the wind turbine design is modified. The numerical simulations created in this work are compared with the results of the bare wind turbine simulations and the experimental power generation data obtained from (Ohya et al., 2008). The geometry consists of a large one-third cylindrical enclosure with an interior rotating mesh around the turbine blade with periodic boundary conditions on either side. The torque of the blade can be calculated and compared to the original experimental power production values. Three comparison speeds are chosen; four, six, and eight meters per second based on physical data available. In experiments done on a bare wind turbine, the power values compare very well to the

expected results from the research group from Japan. For 4, 6, and 8 m/s wind speeds, the percent differences in power production between the actual results and numerical results were 0.81%, 3.39%, and 5.23% different respectively. The values produced numerically were all higher than the experimental data, which should be the case because general wind turbine losses that are briefly introduced in Section 1.3 are not considered in this study.

It is the hope that this work will be continued further by having another researcher to work on a shrouded numerical model by benchmarking it according to the experimental flanged diffuser results from a research team in Japan that performed many experiments regarding shrouding on wind turbines. It is the hope that shrouding is added because adding a shroud to a normal wind turbine can almost quintuple power production compared standard wind turbines (Ohya et al., 2008).

Acknowledgements

I would like to thank Dr. Yi-Tung Chen for his continued advising throughout the creation of this numerical simulation. I would also like to thank Dr. Wenxiao Chu for his advice on numerical methods.

Table of Contents

Abstract	iii
Acknowledgements	v
Table of Contents	vi
List of Tables	viii
List of Figures	ix
Nomenclature	xiii
Introduction	1
1.1 Wind Turbine Literature Review	1
1.2 Computational Modeling Literature Review	11
1.3 General Turbine Losses	24
1.4 Objectives	26
1.5 Organization	27
The Blade Element and Momentum Theory	28
2.1 Method and Procedure	28
2.2 MATLAB [®] Implementation	31
2.3 Translation from Text Coordinates to CAD	44
Numerical Model	47
3.1 Numerical Model Settings	47
3.2 Numerical Model Boundary Conditions	49
3.3 Two-dimensional Airfoil Testing	51
3.4 Three-dimensional Mesh Generation	56
3.5 Mesh Independent Study	58

Results and Discussions	67
4.1 Initial 6 m/s mesh testing	67
4.2 Initial 4 m/s Mesh Testing	78
4.3 Initial 8 m/s Mesh Testing	85
4.4 Final Results for All Wind Speeds	91
Conclusions and Future Work.....	103
5.1 Conclusions.....	103
5.2 Future Work	103
Appendix A: BEMT MATLAB [®] Code	105
Bibliography	112
Curriculum Vitae	119

List of Tables

Table 1: Pros and cons of VAWTs, HAWTs, and additional diffusers	7
Table 2: Summary of power, rotating speed, and torque for bare vs. shrouded wind turbine	32
Table 3: NACA 63-210 airfoil coordinates data.....	34
Table 4: Operating conditions and physical properties.....	47
Table 5: Mesh investigation.....	59
Table 6: Point comparison 1.5e-5 m vs. 3e-5 m first layer thickness	60
Table 7: Point comparison to 9e-4 m vs. 3e-3 m blade sizing	61
Table 8: Point comparison to 7e-4 m vs. 9e-4 m blade sizing	62
Table 9: Point comparison 0.04 m vs. 0.05 m refinement sizing.....	63
Table 10: Point comparison 0.035 m vs. 0.04 m refinement sizing.....	64
Table 11: Torque percent difference per mesh tested	65
Table 12: Summary of torque for multiple wind speeds.....	92

List of Figures

Figure 1: 2017 wind energy production breakdown	1
Figure 2: HAWT example (PEXELS, 2018)	2
Figure 3: Savonius rotor example (“The Benefits of the Helix Wind Turbine - UAT Group,” n.d.)	3
Figure 4: Darrius turbine example (“Sky Harvest to acquire vertical axis wind turbine technology and manufacturing facilities,” 2013).....	3
Figure 5: Shrouded HAWT from Ohya et al. (2008).....	4
Figure 6: Shrouded VAWT example (“Millennium Wind Turbine,” 2015)	5
Figure 7: Horizontal axis wind turbine with shroud	9
Figure 8: BEMT flow chart.....	31
Figure 9: Power generation for bare wind turbine from Ohya et al. (2008)	32
Figure 10: AOA, flow inlet angle, and pitch of turbine blade vs. rotor position	38
Figure 11: Axial induction factor (a), angular induction factor (a'), thrust coefficient (C_t) vs. rotor position.....	40
Figure 12: Lift and drag coefficients vs. rotor position	41
Figure 13: Power vs. wind velocity	42
Figure 14: Top view of blade coordinates	43
Figure 15: Front view of blade coordinates	44
Figure 16: Front view wind turbine blade geometry	45
Figure 17: Side view wind turbine blade geometry	46
Figure 18: Stationary enclosure	49
Figure 19: Rotating blade enclosure	50

Figure 20: Side view of blade enclosure and sketch view	50
Figure 21: Two-dimensional computational domain	53
Figure 22: Two-dimensional mesh	53
Figure 23: y^+ airfoil.....	55
Figure 24: Pressure contour for 63-210 airfoil	55
Figure 25: Front view of mesh.....	57
Figure 26: Side view of mesh	58
Figure 27: Points for mesh independent study.....	59
Figure 28: Torque vs. node count	66
Figure 29: y^+ blade surface (3e-3 m)	68
Figure 30: y^+ blade surface (9e-4 m)	69
Figure 31: y^+ blade surface (7e-4 m)	69
Figure 32: Velocity in stationary frame contour for 0.2 m slice in y-direction (3e-3 m).....	70
Figure 33: Velocity in stationary frame contour for 0.2 m slice in y-direction (9e-4 m).....	71
Figure 34: Velocity in stationary frame contour for 0.2 m slice in y-direction (7e-4 m).....	71
Figure 35: Pressure contour for 0.2 m slice in y-direction (3e-3 m).....	72
Figure 36: Pressure contour for 0.2 m slice in y-direction (9e-4 m).....	73
Figure 37: Pressure contour for 0.2 m slice in y-direction (7e-4 m).....	74
Figure 38: Velocity in stationary frame in y-z plane (3e-3)	75
Figure 39: Velocity in stationary frame in y-z plane (9e-4)	75
Figure 40: Velocity in stationary frame in y-z plane (7e-4 m)	76
Figure 41: Pressure contour in y-z plane (3e-3 m)	76
Figure 42: Pressure contour in y-z plane (9e-4 m)	77

Figure 43: Pressure contour in y-z plane (7e-4 m)	78
Figure 44: y^+ blade surface (9e-4 m)	79
Figure 45: y^+ blade surface (7e-4 m)	80
Figure 46: Velocity in stationary frame contour for 0.2 m slice in y-direction (9e-4 m)	80
Figure 47: Velocity in stationary frame contour for 0.2 m slice in y-direction (7e-4 m)	81
Figure 48: Pressure contour for 0.2 m slice in y-direction (9e-4 m).....	81
Figure 49: Pressure contour for 0.2 m slice in y-direction (7e-4 m).....	82
Figure 50: Velocity in stationary frame in y-z plane (9e-4 m)	83
Figure 51: Velocity in stationary frame in y-z plane (7e-4 m)	83
Figure 52: Pressure contour in y-z plane (9e-4 m)	84
Figure 53: Pressure contour in y-z plane (7e-4 m)	84
Figure 54: y^+ blade surface (9e-4 m)	85
Figure 55: y^+ blade surface (7e-4 m)	86
Figure 56: Velocity in stationary frame contour on 0.2 m slice in y-direction (9e-4 m).....	87
Figure 57: Velocity in stationary frame contour on 0.2 m slice in y-direction (7e-4 m).....	87
Figure 58: Pressure contour on 0.2 m slice in y-direction (9e-4 m)	88
Figure 59: Pressure contour on 0.2 m slice in the y-direction (7e-4 m)	89
Figure 60: Velocity in the stationary frame in y-z direction (9e-4 m).....	89
Figure 61: Velocity in the stationary frame in the y-z plane (7e-4 m)	90
Figure 62: Pressure contour in y-z plane (9e-4 m)	90
Figure 63: Pressure contour in y-z plane (7e-4 m)	91
Figure 64: Streamline of velocity in stationary frame for 4 m/s.....	93
Figure 65: Streamline of velocity in stationary frame for 6 m/s.....	94

Figure 66: Streamline of velocity in stationary frame for 8 m/s.....	94
Figure 67: y^+ blade surface in x, y, and z directions (4 m/s)	95
Figure 68: y^+ blade surface in x, y, and z directions (6 m/s)	95
Figure 69: y^+ plot for blade surface in x, y, and z, directions (8 m/s)	96
Figure 70: Velocity in stationary frame contour on 0.2 m slice in y-direction (4 m/s)	96
Figure 71: Velocity in stationary frame contour on 0.2 m slice in y-direction (6 m/s)	97
Figure 72: Velocity in stationary frame contour on 0.2 m slice in y-direction (8 m/s)	97
Figure 73: Pressure contour on 0.2 m slice in y-direction (4 m/s).....	98
Figure 74: Pressure contour of 0.2 m slice in y- direction (6 m/s)	99
Figure 75: Pressure contour of 0.2 m slice in y-direction (8 m/s)	99
Figure 76: Velocity in stationary frame contour in y-z plane (4 m/s)	100
Figure 77: Velocity in stationary frame contour in y-z plane (6 m/s)	100
Figure 78: Velocity in stationary frame contour in y-z plane (8 m/s)	101
Figure 79: Pressure contour in y-z plane (4 m/s).....	102
Figure 80: Pressure contour in y-z plane (6 m/s).....	102
Figure 81: Pressure contour in y-z plane (8 m/s).....	102

List of Nomenclature

α_n	Element specific angle of attack (degree)
$\alpha_{\text{optimal},n}$	Angle of attack value where element specific C_l/C_d is maximum (degree)
δ	Diffuser opening angle (degree)
\circ	(degree)
$\theta_{p,n}$	Element specific pitch (degree)
θ_t	Angle of twist (degree)
λ	Tip-speed-ratio
λ_n	Element specific tip-speed-ratio
μ	Dynamic viscosity (kg/(m-s))
μ_t	Turbulent viscosity
ρ	Density (kg/m ³)
σ'_n	Element specific blade solidity
ϕ_n	Relative wind inlet angle
ϕ	General flow variable
$\bar{\phi}$	Mean of ϕ
ϕ'	Fluctuation of ϕ
ω	Angular velocity (rad/s, RPS)
a_n	Element specific axial induction factor
a'_n	Element specific angular induction factor
c	Chord length (m)
C_d	Coefficient of drag
C_l	Coefficient of lift
$C_{l_{\text{max}},n}$	Section coefficient of lift where C_l/C_d is maximum
c_n	Element specific chord length (m)
C_w	Power coefficient
D_{dif}	Diffuser entrance diameter (m)
D_h	Hub diameter (m)
D_r	Rotor diameter (m)
dF_{thrust}	Thrust contribution per element (N)
dQ	Torque contribution per element (N-m)
$F_{t,n}$	Tip loss correction factor
$F_{h,n}$	Tip loss correction factor
F_n	Combined loss correction factor
H	Flange height (m)
I	Turbulence intensity (%)
L_{dif}	Diffuser length (m)
L_{hub}	Hub length (m)
p	Pressure (Pa)
P	Power (W)
r_n	Element specific radius (m)

SAF	Shroud amplification factor ($U_{\text{Blade}}/ U_{\infty}$)
t	Time (s)
T	Temperature (K)
u	x-velocity (m/s)
U_{Blade}	Wind velocity seen by blade (m/s)
U_{∞}	Freestream velocity (m/s)
v	y-velocity (m/s)
\vec{v}	Velocity vector (m/s)
w	z-velocity (m/s)
Z_b	Number of blades

Introduction

1.1 Wind Turbine Literature Review

Wind turbines are not a new concept, so why research them? In 2017, there was 539,581 MW in wind energy produced worldwide (Global Wind Energy Council, 2018). Even a small growth for efficiency in wind turbines can lead to a big benefit to renewable energy for the world. The distribution of the wind power in 2017 worldwide is shown in Figure 1.

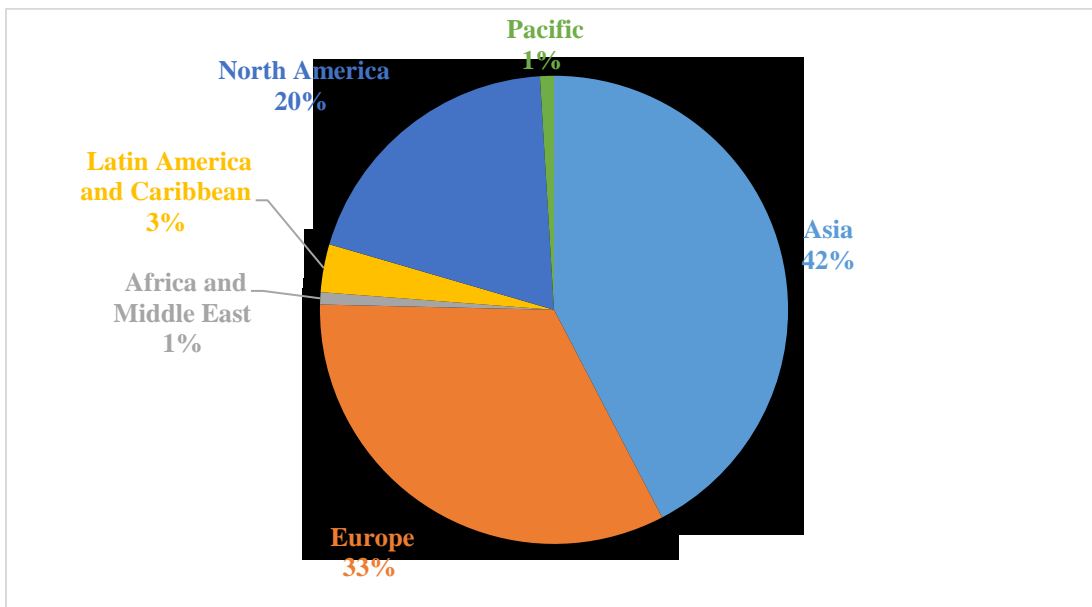


Figure 1: 2017 wind energy production breakdown

China is first in the world for production of wind energy at 178,096 MW with the United States being second in production at 89,077 MW produced (Global Wind Energy Council, 2018).

There are multiple forms of wind turbines, broken up into four categories; Horizontal Axis Wind Turbines (HAWTs), Vertical Axis Wind Turbines (VAWTs), and shrouded versions of either of the previous two types.

Large HAWTs like one of the largest wind turbines on the market- the V164-9.5 MW from MHI Vestas Offshore Wind- has a 164-meter rotor diameter that can produce up to 9.5 MW of

power at wind speeds above around 12 m/s to as high as 25 m/s (“Innovations | Offshore Wind Turbines | MHI Vestas™,” 2018). An example of a HAWT is pictured in Figure 2.



Figure 2: HAWT example (PEXELS, 2018)

These large diameters need a lot of space to be maximized. Unfortunately, there is also a lot of noise generation from wind turbines. In urban environments HAWTs have difficulties as far as low performance when placed on building tops due to skewed flows experienced in those environments (Krishnan & Paraschivoiu, 2016).

VAWTs are divided between two types, Savonius rotors and Darrieus turbines pictured in Figures 3 and 4.



Figure 3: Savonius rotor example (“The Benefits of the Helix Wind Turbine - UAT Group,” n.d.)

Savonius rotors, Figure 3, are drag driven while Darrieus turbines, Figure 4, are lift driven. Lift driven turbines generally have higher power coefficients (Thé & Yu, 2017; Chen et al., 2015; Eriksson et al., 2008). Darrieus rotor VAWTs are generally more suitable for urban locations due to their capability of handling the skewed fields that buildings can generate compared to open expanses - where HAWTs are more dominant (Chen et al., 2015; Balduzzi et al., 2012).



Figure 4: Darrieus turbine example (“Sky Harvest to acquire vertical axis wind turbine technology and manufacturing facilities,” 2013)

Generally, HAWTs have higher power coefficients compared to VAWTs (Mertens, 2003; Riegler, 2003; Thé & Yu, 2017). VAWTs generally have less moving parts, are quieter, are insensitive to wind direction, and are more capable at handling skewed flows compared to HAWTs (Alam & Golde, 2013; Ali et al., 2011).

Shrouding has been shown to almost quintuple power production compared standard HAWTs (Ohya et al., 2008). The geometry is shown in Figure 5 and will be gone into further detail toward the end of this section.

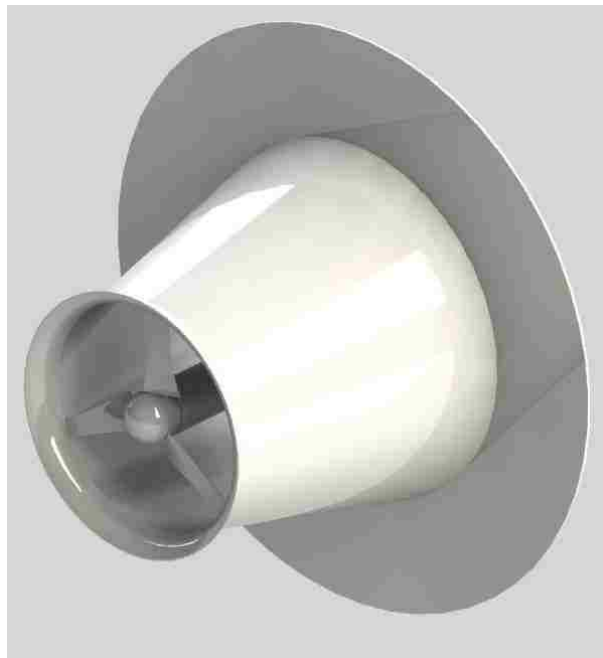


Figure 5: Shrouded HAWT from Ohya et al. (2008)

A research group created a diffuser shroud design for a VAWT that is mounted to the tops of buildings. Using the $k-\epsilon$ turbulence model with enhanced wall function, the group ran tests on an 8'x8'x8' previously created prototype that had a ramp and door in the front to draw more air into the turbine. The angle of the door was investigated as well as adding a flange at the rear of the apparatus similar to the work of Ohya et al. (2008). Overall the group was able to increase the C_w

from 0.14 for the original design to 0.34 - an increase by a multiple of 2.43 times the original turbine (Krishnan & Paraschivoiu, 2016).

An example of a shrouded VAWT is pictured in Figure 6. Note that the diffuser is meant to funnel wind and increase the velocity seen by the blades to rotate the turbine faster to create more power production.

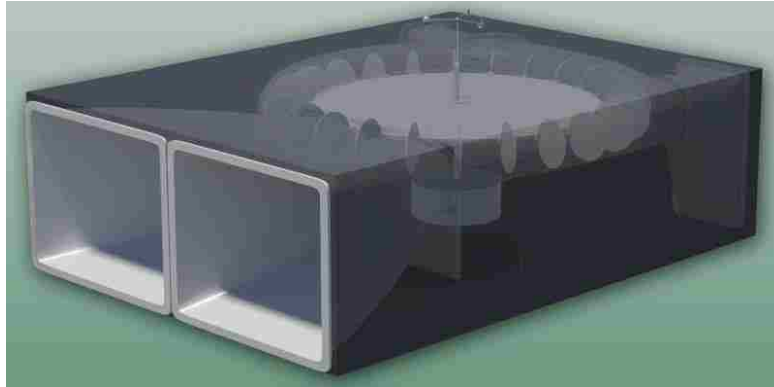


Figure 6: Shrouded VAWT example (“Millennium Wind Turbine,” 2015)

Traditional wind turbines are not the only turbines that can benefit from shrouding, hydro turbines that are shrouded can produce 3.1 times the power compared to conventional hydro turbines (Gaden & Bibeau, 2010). There are many more challenges for hydro turbines such as spatial requirements, low power densities and other issues associated with water as a working fluid such as its high density. A hydro turbine was simulated using the $k-\epsilon$ model using ANSYS-CFX[®]. Although the turbine blade was not modeled, the momentum source method was used to mimic the presence of a turbine blade. The diffuser was modeled in such a way that it had a flat section that had the turbine blade eventually opening up into a diffuser similar.

The shrouded effect on turbines has been experimented on for a number of decades. Lilley and Rainbird studied the effect of ducting on windmills analytically using rotor disc theory. The theoretical results showed an increase of the power output by as much as 65% compared to a traditional windmill (Lilley & Rainbird, 1956).

In a project for the Grumman Aerospace Corporation, diffuser geometry consisted of a large diffuser angle of 60 degrees with an area ratio of 2.78 with multiple slots at the front and toward the rear of the diffuser to generate about twice the power of a conventional wind turbine system (Gilbert et al., 1978).

Gilbert and Forman did more testing of diffusers in a 2x3 m wind tunnel with an untwisted, constant chord, wind turbine, with three blades. The results of the testing showed an improvement up to 3.4 times the power based on the Betz limit (Gilbert & Foreman, 1983).

A 7.3 m diameter wind turbine was fitted with a diffuser to augment the power that is produced and was originally developed by the Grumman Aerospace Corporation under K.M. Gilbert (Phillips et al., 1999). The main features of the shroud were multiple slots at the entrance and towards the rear along with a small flange at the outlet. Overall, experimental and numerical results showed inlet velocity improvements.

Igra developed multiple iterations of diffusers. The first design was an interesting diffuser geometry that consisted a converging intake similar to the inlet shroud of Ohya et al. (2008) with a straight section at the turbine blades, leading into a diffuser, and eventually leading to 3 rings consisting of the NACA 1412 airfoil. The second consisted of multiple airfoils separated, but the tail regions leading into one another. The final design of the paper consisted of a single airfoil as the diffuser. The main idea behind the geometries was to try and create a pressure difference between the front and rear of the turbine to increase the air velocity seen by the turbine blades for increased power production (Igra, 1981).

Bet & Grassmann (2003) made a diffuser similar to the work of Igra (1981) by modeling it after a singular airfoil and modifying it two a series of two airfoils. The group simulated it in

Star-CD[®] diffuser calculations and pressure simulations. The turbine used was a propeller with 36 blades with radius 0.56. Overall the group increased the power by a multiple of 2.

The pros and cons of HAWTs, VAWTS and the shrouded versions of both are summarized in Table 1.

Table 1: Pros and cons of VAWTs, HAWTs, and additional diffusers

Type:	VAWT	Shrouded VAWT	HAWT	Shrouded HAWT
Pros:	<ul style="list-style-type: none"> • Able to handle skewed flows. • Less moving parts. • Quieter because of lower tip speed ratio (TSR). • Less sensitive to wind direction. 	<ul style="list-style-type: none"> • Increase in power output. • Noise reduction. 	<ul style="list-style-type: none"> • Can have large scale power production. 	<ul style="list-style-type: none"> • Increase in power output. • Noise Reduction.
Cons:	<ul style="list-style-type: none"> • Relatively low power production. 	<ul style="list-style-type: none"> • More structure needed to support extra thrust load. • More expensive. • Large scale less feasible. 	<ul style="list-style-type: none"> • Loss of performance in skewed flows. • Generate more noise • Sensitive to wind direction (yaw) • More moving components 	<ul style="list-style-type: none"> • More structure needed to support extra thrust load. • More expensive. • Large scale less feasible.

As mentioned, researchers in Japan developed a flanged diffuser that, at peak production, was able to quintuple power production compared standard HAWTs (Ohya et al., 2008). to increase the power output by as much as five times that of a traditional wind turbine (Ohya et al., 2008). Since power generation for wind turbines is directly related to the cubic wind speed, a small increase in the velocity seen by the blades can lead to dramatic increases in power generation. The team investigated different types of shroud geometries- nozzles, diffusers, cylinders- and discovered that a diffuser type shroud created the most wind speed augmentation

as seen by the rotor. The diffuser without a rotor created an increase in inlet velocity by a factor of about 1.8. Next the team augmented the diffuser with several modifications. A curved nozzle was attached to the diffuser entrance followed by a flange at the rear of the diffuser. Both aspects were tested separately and then tested together. When together the velocity can increase between 1.6 and 2.4 times the incoming velocity.

The results show that the combination with a sufficient L_{dif}/D_{dif} produced the best results. The highest length to diffuser ratio of 4.5, there was an overall amplification of about 2.4 times the wind velocity compared to about 2 times for just a diffuser with an inlet shroud. For the diffuser being modeled in this work, the average shroud amplification factor (SAF) turned out to be about 1.3 at the rotor compared to a traditional wind turbine that registered only 0.8 resulting in about a power generation increase by a factor of 4.29 (Ohya et al., 2008). The fundamental reasoning why the wind speed is amplified is because of a high pressure region being created at the front of the diffuser and a low pressure region being created at the rear of the diffuser, driving in more flow through the diffuser, as well as the decrease between the diffuser inlet area compared to the nozzle inlet area. The shroud that was created were based around a set of geometry relations and are summarized in Figure 7.

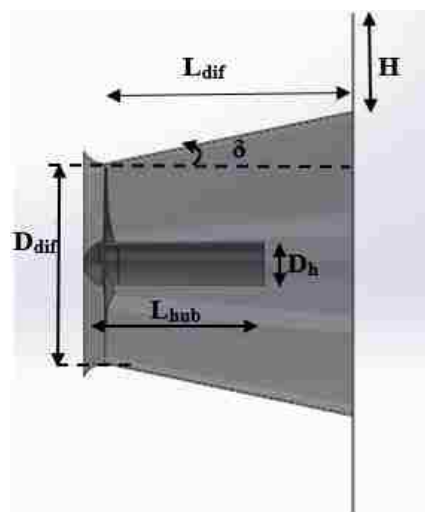


Figure 7: Horizontal axis wind turbine with shroud

D_{dif} is not the diameter of the rotor or entrance diameter of the inlet shroud, but the diffuser inlet entrance. H is the flange height and δ is the diffuser inlet angle. L_{dif} is the length of the diffuser and similarly L_{hub} is the length of the entire hub from blade to generator enclosure.

The team experimented with the shroud geometries over a number of years and ultimately determined the optimal geometry of the shroud equipped with a wind turbine to have the dimensions of L_{dif}/D_{dif} of 1.25, H to D_{dif} ratio of 0.5, L_{hub} of 75 % of L_{dif} , A_{ratio} of 2.35, and D_{hub} to D_{dif} ratio of 22 %. While running at an optimal tip speed ratio of 4.2 (Ohya et al., 2004; Ohya et al., 2008; Abe & Ohya, 2004; Inoue et al., 2002).

The inlet specifications were not listed in Ohya et al. (2008), but in a previous work by the research team performing wind tunnel testing on flanged diffusers, the experiment apparatus had similar dimensional relationships, with the inlet shroud being about 14% larger than the diffuser inlet diameter (Abe et al., 2005). Compared to the current shroud, the inlet shroud should have an entrance diameter of 0.8208 meters.

In the same work by Abe et al. (2004), the team experimented with a 2D model that tried to model the entire system asymmetrically using the disk loading method to model the blades produced reasonable result with some inconsistencies at the blade tip and underestimation of inlet wind velocities. In a prior work, the team also made a 2D computational model similar to Abe et al. (2005), with the difference of not having the blade hub in the model and instead having a load in that area to experiment with the opening angle of the diffuser (Abe & Ohya, 2004).

A separate team also investigated flanged diffusers computationally using the Spalart Allmaras and $k-\epsilon$ RNG turbulent models in ANSYS-Fluent[®]. The model was very similar to Abe

& Ohya (2004) except there is merely a geometric load in place of the rotor to obstruct the flow in the shroud to observe the shrouding impact on flow velocity (Mansour & Meskinkhoda, 2014).

Kannan et al. (2013) also did testing on the diffuser without modeling the blades. The group was mainly concerned with diffuser geometry and expanded upon adding other obstructions to the flow to try and increase the velocity through the diffuser using two-dimensional simulations.

To get a better understanding of design of normal bare wind turbines, an article regarding numerical and experimental analysis of small wind turbines was reviewed. The article has a clear method of optimization. First the given sizing geometry, the group uses the 1-D blade element and momentum theory (BEMT) to design an initial optimized shape of the turbine blade using a NACA 4415 airfoil. From that point the model is tested in a computational domain with the dominant characteristics being a maximum skewness of less than 0.85 and a y^+ value less than 1 with a tetrahedral mesh being converted to a polyhedral mesh to reduce cell count. The model made use of a moving reference frame to generate a steady state solution. The solver preferences used a Courant number between 50 and 100, relaxation factors between 0.2 and 0.25, as well as second-order upwind discretization for all equations. Based on the numerical results, two blades were constructed and then tested in a 0.5 x 0.5 x 1.2 meter wind tunnel. For the first rotor, there were blockage effects that lead to the numerical model producing larger power generation compared to the experimental data. For the second rotor, which was a reduced diameter, the computational results compared reasonable well to experimental data (Lanzafame et al., 2016).

Over the course of surveying an article was found relating to 3D modeling of a shrouded wind turbine using a Reynolds-averaged Navier-Stokes (RANS) solver. The group analyzed the computational work of Ohya et al. (2008) and believed that the swirl effects are not correctly

modeled using the rotor disk theory. The group set out to design their own shrouded wind turbine with a geometry far different from the research group from Japan. The blade was a National Renewable Energy Laboratory (NREL) Phase IV wind turbine blade with an S809 airfoil tested with a 2D structured C-shape mesh to compare to available NREL data. The shroud was initially generated by extruding a NACA 0006 airfoil at a specific angle of attack (AOA). The 3D simulation comes together with an overset mesh of the entire wind turbine blade-except for the hub, another C-shape mesh for the shroud, all combined in a half-cylindrical domain with periodic boundary conditions. The team compares several different airfoils for the shroud-Eppler E423, Selig S122, a modified NACA 0006, and an FX 74-CL5-140 airfoil. Of the shrouds tested, the Selig S122 provided the largest flow rate amplification (Aranake et al., 2015). Overall the group was primarily concerned with shroud geometry, but the journal article provides insight into mesh construction.

1.2 Computational Modeling Literature Review

A research group experimented numerically the impacts of shrouding on rooftop VAWTs using a moving mesh transient scheme using the $k-\varepsilon$ turbulence model with enhanced wall treatment and generated reasonable results (Krishnan & Paraschivoiu, 2016).

Another group has developed a method of performing fluid structure interaction (FSI) by simulating an NREL 5 MW offshore wind turbine. The model boundary conditions consisted of one third of a cylinder with periodic boundary conditions on either side as the enclosure while modeling a single blade of the turbine. Overall the group's results compared well to other results (Bazilevs et al., 2011).

RANS models are a popular choice in industry for modeling turbulent fluid flow. For a Newtonian fluid that is steady state, incompressible, and in the laminar region, the general Navier-Stokes equations are as such (Bird et al., 2007):

Continuity:

$$\vec{\nabla} \cdot \vec{v} = 0 \quad (1)$$

Momentum:

$$\rho \left(u \frac{\partial u}{\partial x} + v \frac{\partial u}{\partial y} + w \frac{\partial u}{\partial z} \right) = -\frac{\partial p}{\partial x} + \mu \left(\frac{\partial^2 u}{\partial x^2} + \frac{\partial^2 u}{\partial y^2} + \frac{\partial^2 u}{\partial z^2} \right) + \rho g_x \quad (2)$$

$$\rho \left(u \frac{\partial v}{\partial x} + v \frac{\partial v}{\partial y} + w \frac{\partial v}{\partial z} \right) = -\frac{\partial p}{\partial y} + \mu \left(\frac{\partial^2 v}{\partial x^2} + \frac{\partial^2 v}{\partial y^2} + \frac{\partial^2 v}{\partial z^2} \right) + \rho g_y \quad (3)$$

$$\rho \left(u \frac{\partial w}{\partial x} + v \frac{\partial w}{\partial y} + w \frac{\partial w}{\partial z} \right) = -\frac{\partial p}{\partial z} + \mu \left(\frac{\partial^2 w}{\partial x^2} + \frac{\partial^2 w}{\partial y^2} + \frac{\partial^2 w}{\partial z^2} \right) + \rho g_z \quad (4)$$

When the flow is turbulent, the RANS equations are used. They are based on the assumption that while there are fluctuations in the flow, the fluctuations will oscillate about a mean value (Malalasekera & Versteeg, 2006). The mean general flow property is defined below.

$$\bar{\phi} = \frac{1}{\Delta t} \int_0^{\Delta t} \phi(t) dt \quad (5)$$

where,

$$\phi = \bar{\phi} + \phi' \quad (6)$$

The Navier-Stokes equations are transformed into the equations below (Malalasekera & Versteeg, 2006).

Continuity:

$$\frac{\partial \bar{u}}{\partial x} + \frac{\partial \bar{v}}{\partial y} + \frac{\partial \bar{w}}{\partial z} = 0 \quad (7)$$

Momentum:

$$\begin{aligned}
& \frac{\partial(\bar{u}^2)}{\partial x} + \frac{\partial(\bar{u}\bar{v})}{\partial y} + \frac{\partial(\bar{u}\bar{w})}{\partial z} \\
= & -\frac{1}{\rho} \frac{\partial \bar{p}}{\partial x} + \nu \left[\frac{\partial^2 \bar{u}}{\partial x^2} + \frac{\partial^2 \bar{u}}{\partial y^2} + \frac{\partial^2 \bar{u}}{\partial z^2} \right] + \frac{1}{\rho} \left[\frac{\partial \overline{\rho u'^2}}{\partial x} + \frac{\partial \overline{\rho u'v'}}{\partial y} + \frac{\partial \overline{\rho u'w'}}{\partial z} \right]
\end{aligned} \tag{8}$$

$$\begin{aligned}
& \frac{\partial(\bar{u}\bar{v})}{\partial x} + \frac{\partial(\bar{v}^2)}{\partial y} + \frac{\partial(\bar{v}\bar{w})}{\partial z} \\
= & -\frac{1}{\rho} \frac{\partial \bar{p}}{\partial y} + \nu \left[\frac{\partial^2 \bar{v}}{\partial x^2} + \frac{\partial^2 \bar{v}}{\partial y^2} + \frac{\partial^2 \bar{v}}{\partial z^2} \right] + \frac{1}{\rho} \left[\frac{\partial \overline{\rho v'u'}}{\partial x} + \frac{\partial \overline{\rho v'^2}}{\partial y} + \frac{\partial \overline{\rho v'w'}}{\partial z} \right]
\end{aligned} \tag{9}$$

$$\begin{aligned}
& \frac{\partial(\bar{u}\bar{w})}{\partial x} + \frac{\partial(\bar{v}\bar{w})}{\partial y} + \frac{\partial(\bar{w}^2)}{\partial z} \\
= & -\frac{1}{\rho} \frac{\partial \bar{p}}{\partial z} + \nu \left[\frac{\partial^2 \bar{w}}{\partial x^2} + \frac{\partial^2 \bar{w}}{\partial y^2} + \frac{\partial^2 \bar{w}}{\partial z^2} \right] + \frac{1}{\rho} \left[\frac{\partial \overline{\rho w'u'}}{\partial x} + \frac{\partial \overline{\rho w'v'}}{\partial y} + \frac{\partial \overline{\rho w'^2}}{\partial z} \right]
\end{aligned} \tag{10}$$

where the negatives of $\overline{\rho u'^2}$, $\overline{\rho v'^2}$, and $\overline{\rho w'^2}$ are the normal stresses and the negatives of $\overline{\rho u'v'}$, $\overline{\rho u'w'}$, and $\overline{\rho w'v'}$ are the shear stresses known as the Reynolds stresses. Turbulence models like the k-ε model utilize an assumption originally created by Boussinesq to equate the Reynolds stresses proportionally to the mean rates of deformation with the general formulation being shown below in tensor notation (Malalasekera & Versteeg, 2006).

$$\tau_{ij} = -\overline{\rho u'_i u'_j} = \mu_t \left(\frac{\partial \bar{u}_i}{\partial x_j} + \frac{\partial \bar{u}_j}{\partial x_i} \right) - \frac{2}{3} \rho \left(\frac{1}{3} (\overline{u'^2} + \overline{v'^2} + \overline{w'^2}) \right) \delta_{ij} \tag{11}$$

When other scalar variables are present such as temperature, the transport equation for an arbitrary scalar function such as the flow variable, $\bar{\phi}$, becomes:

$$\begin{aligned}
& \frac{\partial \bar{u}\bar{\phi}}{\partial x} + \frac{\partial \bar{v}\bar{\phi}}{\partial y} + \frac{\partial \bar{w}\bar{\phi}}{\partial z} \\
= & \frac{\Gamma}{\rho} \left(\frac{\partial^2 \bar{\phi}}{\partial x^2} \right) + \left(\frac{\partial^2 \bar{\phi}}{\partial y^2} \right) + \left(\frac{\partial^2 \bar{\phi}}{\partial z^2} \right) - \left[\left(\frac{\partial \overline{u'\phi'}}{\partial x} \right) + \left(\frac{\partial \overline{v'\phi'}}{\partial y} \right) + \left(\frac{\partial \overline{w'\phi'}}{\partial z} \right) \right] \\
& + S
\end{aligned} \tag{12}$$

Say the scalar variable is temperature, the equation turns into the energy equation where the general flow variable turns into a T and Γ is expressed as the general thermal conductivity divided by the specific heat.

A research group created a critical review of many of the RANS methods available in ANSYS along with other solvers using Hybrid RANS and LES Models (Thé & Yu, 2017). The models gone over in this journal article that were of the most interest for this work were the ANSYS RANS solvers: Spalart-Allmaras, k - ϵ models, k - ω SST model.

The Spalart-Allmaras turbulence model that makes use of only one equation was originally created by Boeing to simulate airfoils (Spalart & Allmaras, 1992; Thé & Yu, 2017). The model's weakness is flows that involve boundary layer separation as the model gives an inaccurate surface pressure distribution (Song & Perot, 2015; Thé & Yu, 2017; You et al., 2013). The Spalart-Allmaras turbulence model was used to simulate the flow conditions on a VAWT with the results yielding significant differences compared to experimental results (Nini et al., 2014; Pope et al., 2010; Thé & Yu, 2017).

The two equation k - ϵ turbulence model solves the RANS equations along with two additional equations. The equations that are used with the RANS equations are the turbulence energy, k and the energy dissipation, ϵ (Launder, 1972). The kinetic energy is obtained from an exact equation, but the ϵ transport equation is more of an empirical formulation (ANSYS Inc., 2011). The k - ϵ model is only for fully turbulent flows because its main assumption is that the molecular viscosity effects are insignificant for turbulent flows (ANSYS Inc., 2011). There are also other versions of the k - ϵ turbulence model; the Realizable and Renormalization Group (RNG) models. It is a very highly used model for computational fluid dynamics (CFD) problems because of its ease of use and robustness. Although the model is highly used, it has its weaknesses. The k - ϵ

turbulence model is unable to capture vortex shedding as well as flow separation because they require more resolution of the boundary layer- the characteristics mentioned are very important in wind turbine aerodynamics (Thé & Yu, 2017). The inabilities of the model cause it to sometimes over predict aerodynamic performance of wind turbines.

The group specified a variety of practices for meshing and boundary conditions to achieve accuracy. When employing a multiple reference frame mesh in which one region is rotating and another region is stationary, the interfaces need to match in order to provide accuracy. Adding a blunt trailing edge at 98% chord length to avoid orthogonality issues was proven to be acceptable in RANS simulations for an NREL Phase VI rotor (Song & Perot, 2015). For inlet conditions a turbulent viscosity ratio of around 10 and a uniform velocity is acceptable (Thé & Yu, 2017; Tu et al., 2012).

The steady state, incompressible turbulent kinetic energy equation (k) is shown below for the standard k-ε turbulence model (ANSYS Inc., 2011):

$$\begin{aligned} & \rho \left(\frac{\partial k u}{\partial x} + \frac{\partial k v}{\partial y} + \frac{\partial k w}{\partial z} \right) \\ = & \left[\frac{\partial}{\partial x} \left(\left(\mu + \frac{\mu_t}{\sigma_\epsilon} \right) \frac{\partial k}{\partial x} \right) + \frac{\partial}{\partial y} \left(\left(\mu + \frac{\mu_t}{\sigma_\epsilon} \right) \frac{\partial k}{\partial y} \right) + \frac{\partial}{\partial z} \left(\left(\mu + \frac{\mu_t}{\sigma_\epsilon} \right) \frac{\partial k}{\partial z} \right) \right] + G_k \\ & + G_b a g - \rho \epsilon + S_k \end{aligned} \quad (13)$$

where S_k is a source term. The μ_t term is turbulent viscosity. The σ_ϵ term is the turbulent Prandtl number. The G_k term is the turbulent kinetic energy produced from the average velocity gradients. The G_b term is the buoyancy caused creation of turbulent kinetic energy.

$$\begin{aligned} G_k = & -\rho \left(\overline{u'u'} \frac{\partial u}{\partial x} + \overline{u'v'} \frac{\partial v}{\partial x} + \overline{u'w'} \frac{\partial w}{\partial x} + \overline{v'u'} \frac{\partial u}{\partial y} + \overline{v'v'} \frac{\partial v}{\partial y} + \overline{v'w'} \frac{\partial w}{\partial y} + \overline{w'u'} \frac{\partial u}{\partial z} \right. \\ & \left. + \overline{w'v'} \frac{\partial v}{\partial z} + \overline{w'w'} \frac{\partial w}{\partial z} \right) \end{aligned} \quad (14)$$

$$G_b = -\frac{1}{\rho} \left(\frac{\partial \rho}{\partial T} \right)_p \left[g_x \frac{\mu_t}{Pr_t} \frac{\partial T}{\partial x} + g_y \frac{\mu_t}{Pr_t} \frac{\partial T}{\partial y} + g_z \frac{\mu_t}{Pr_t} \frac{\partial T}{\partial z} \right] \quad (15)$$

where Pr_t is 0.85.

$$\mu_t = \frac{\rho C_\mu k^2}{\varepsilon} \quad (16)$$

where C_μ is a model defined constant.

The epsilon equation (ε) is as shown below:

$$\begin{aligned} & \rho \left(\frac{\partial \varepsilon u}{\partial x} + \frac{\partial \varepsilon v}{\partial y} + \frac{\partial \varepsilon w}{\partial z} \right) \\ = & \left[\frac{\partial}{\partial x} \left(\left(\mu + \frac{\mu_t}{\sigma_\varepsilon} \right) \frac{\partial \varepsilon}{\partial x} \right) + \frac{\partial}{\partial y} \left(\left(\mu + \frac{\mu_t}{\sigma_\varepsilon} \right) \frac{\partial \varepsilon}{\partial y} \right) + \frac{\partial}{\partial z} \left(\left(\mu + \frac{\mu_t}{\sigma_\varepsilon} \right) \frac{\partial \varepsilon}{\partial z} \right) \right] \\ & + C_{1\varepsilon} \frac{\varepsilon}{k} (G_k + C_{3\varepsilon} G_b) - C_{2\varepsilon} \rho \frac{\varepsilon^2}{k} + S_\varepsilon \end{aligned} \quad (17)$$

where σ_ε is a turbulent Prandtl number, $C_{1\varepsilon}$, $C_{2\varepsilon}$, $C_{3\varepsilon}$ are model constants and S_ε is a source term.

The empirical model constants are defined below (ANSYS Inc., 2011; Launder & Spalding, 1972).

$$C_{1\varepsilon} = 1.44, C_{2\varepsilon} = 1.92, \sigma_\varepsilon = 1.3, \sigma_k = 1, C_\mu = 0.09$$

where $C_{3\varepsilon}$ is not explicitly stated, but calculated by Fluent where the equation is below and u is perpendicular to gravitational acceleration and v is parallel to it (ANSYS Inc., 2011)

$$C_{3\varepsilon} = \tanh \left| \frac{v}{u} \right| \quad (18)$$

The $k-\omega$ Shear Stress Transport (SST) turbulence model is a blend of the $k-\omega$ and $k-\varepsilon$ models. The model has the robustness that the $k-\varepsilon$ turbulence model has for handling free stream flow coupled with the near wall strengths of the $k-\omega$ turbulence model (Menter, 1994; Menter et. al, 2003; Thé & Yu, 2017). The model became the first RANS solver to fully simulate a wind

turbine in three-dimensional space (Hansen et al., 1997; Sorensen & Hansen, 1998; Thé & Yu, 2017).

Based on the work of David Wilcox, the k - ω model-another two equation RANS based turbulence model as used in ANSYS-Fluent[®] uses the general equations shown for steady state and incompressible fluid flow (ANSYS Inc., 2011; Wilcox, 1998). The turbulent kinetic energy equation (k) is as such:

$$\rho \left(\frac{\partial k u}{\partial x} + \frac{\partial k v}{\partial y} + \frac{\partial k w}{\partial z} \right) = \frac{\partial}{\partial x} \left(\Gamma_k \frac{\partial k}{\partial x} \right) + \frac{\partial}{\partial y} \left(\Gamma_k \frac{\partial k}{\partial y} \right) + \frac{\partial}{\partial z} \left(\Gamma_k \frac{\partial k}{\partial z} \right) + G_k - Y_k + S_k \quad (19)$$

where Γ_k is the effective diffusivity of k .

$$\Gamma_k = \mu + \frac{\mu_t}{\sigma_k} \quad (20)$$

where the turbulent Prandtl number is a model constant of 2 and the turbulent viscosity is defined by (21).

$$\mu_t = \frac{\alpha^* \rho k}{\omega} \quad (21)$$

where the damping coefficient α^* is a low Reynolds number correction shown below and is a combination of a few correction factors based around the turbulent Reynolds number.

$$\alpha^* = \frac{\alpha_\infty^* \left(\frac{\beta_i}{3} + \frac{\rho k}{6\mu\omega} \right)}{1 + \frac{\rho k}{6\mu\omega}} \quad (22)$$

where β_i is a model constant and is 0.072. α_∞^* is equal to 1 for high-Reynolds numbers and S_k is a source term. G_k has the same meaning and equation as in the k - ϵ turbulence model.

Y_k is the dissipation of k because of turbulence.

$$Y_k = \rho \beta^* f_\beta^* k \omega \quad (23)$$

Where β^* is defined below.

$$\beta^* = \frac{\beta_\infty \left(\frac{4}{15} + \left(\frac{\rho k}{R_\beta \mu \omega} \right)^4 \right)}{\left(1 + \left(\frac{\rho k}{R_\beta \mu \omega} \right)^4 \right)} [1 + 1.5 * F(M_t)] \quad (24)$$

where R_β and β_∞ are model constants of 8 and 0.09 respectively. $F(M_t)$ is a piecewise function for the compressibility based on Mach number.

$$F(M_t) = \begin{cases} 0 & \text{for } \sqrt{\frac{2k}{\gamma RT}} \leq 0.25; \\ \sqrt{\frac{2k}{\gamma RT}} - 0.0625 & \text{for } \sqrt{\frac{2k}{\gamma RT}} > 0.25 \end{cases} \quad (25)$$

In this work the Mach number is well below 0.25 and is thus incompressible, making the factor zero.

f_β is also a piecewise function defined below.

$$f_\beta = \begin{cases} 1 & \text{for } X_k \leq 0; \\ \frac{1 + 680X_k^2}{1 + 400X_k} & \text{for } X_k > 0 \end{cases} \quad (26)$$

where,

$$X_k = \frac{1}{\omega^3} \left(\frac{\partial k}{\partial x} + \frac{\partial k}{\partial y} + \frac{\partial k}{\partial z} \right) \left(\frac{\partial \omega}{\partial x} + \frac{\partial \omega}{\partial y} + \frac{\partial \omega}{\partial z} \right) \quad (27)$$

The term above is applied if both gradients of k and ω are aligned in the same direction.

The specific dissipation rate equation (ω) is as such:

$$\rho \left(\frac{\partial \omega u}{\partial x} + \frac{\partial \omega v}{\partial y} + \frac{\partial \omega w}{\partial z} \right) = \frac{\partial}{\partial x} \left(\Gamma_\omega \frac{\partial \omega}{\partial x} \right) + \frac{\partial}{\partial y} \left(\Gamma_\omega \frac{\partial \omega}{\partial y} \right) + \frac{\partial}{\partial z} \left(\Gamma_\omega \frac{\partial \omega}{\partial z} \right) + G_\omega - Y_\omega + S_\omega \quad (28)$$

where Γ_ω is the effective diffusivity of ω and calculated similarly to Γ_k , with the turbulent Prandtl number another model constant that is 2 like the turbulent Prandtl number for Ω .

S_ω is a source term. G_ω is the turbulent energy created from mean velocity gradients.

$$G_\omega = \frac{\alpha\omega G_k}{k} \quad (29)$$

where α is defined by the equation below and is dependent on the turbulent-Reynolds number:

$$\alpha = \frac{\frac{\alpha_\infty}{\alpha^*} \left(\alpha_0 + \frac{\rho k}{\mu\omega R_\omega} \right)}{1 + \frac{\rho k}{\mu\omega R_\omega}} \quad (30)$$

where R_ω is a model constant defined to be 2.95. α_0 is a model constant defined as 0.111. Like α^* , the α and α_∞ values are equal to 1 at high-Reynolds numbers. Y_ω is the dissipation of ω because of turbulence.

$$Y_\omega = \rho\beta f_\beta \omega^2 \quad (31)$$

where,

$$f_\beta = \frac{1 + 70X_\omega}{1 + 80X_\omega} \quad (32)$$

where,

$$X_\omega = \left| \frac{\Omega_{ij}\Omega_{jk}S_{ki}}{(\beta_\infty^*\omega)^3} \right| \quad (33)$$

where the mean rate of rotation tensor is,

$$\Omega_{ij} = \frac{1}{2} \left(\frac{\partial u_i}{\partial x_j} - \frac{\partial u_j}{\partial x_i} \right) \quad (34)$$

and the other tensors are,

$$\Omega_{jk} = \frac{1}{2} \left(\frac{\partial u_j}{\partial x_k} - \frac{\partial u_k}{\partial x_j} \right) \quad (35)$$

$$S_{ki} = \frac{1}{2} \left(\frac{\partial u_i}{\partial x_k} + \frac{\partial u_k}{\partial x_i} \right) \quad (36)$$

and,

$$\beta = \beta_i [1 - 1.5 \frac{\beta_i^*}{\beta_i} F(M_t)] \quad (37)$$

where the values of the constants inside of the equation have previously been defined (ANSYS Inc., 2011; Wilcox, 1998).

The k- ω Shear-Stress Transport (SST) turbulence model is described as follows (ANSYS Inc., 2011; Menter, 1994).

The steady state and incompressible, turbulent kinetic energy equation (k) is shown below.

$$\left(\frac{\partial k u}{\partial x} + \frac{\partial k v}{\partial y} + \frac{\partial k w}{\partial z} \right) = \frac{\partial}{\partial x} \left(\Gamma_k \frac{\partial k}{\partial x} \right) + \frac{\partial}{\partial y} \left(\Gamma_k \frac{\partial k}{\partial y} \right) + \frac{\partial}{\partial z} \left(\Gamma_k \frac{\partial k}{\partial z} \right) + \widetilde{G}_k - Y_k + S_k \quad (38)$$

The steady state and incompressible, specific dissipation rate equation (ω) is shown below.

$$\begin{aligned} & \rho \left(\frac{\partial \omega u}{\partial x} + \frac{\partial \omega v}{\partial y} + \frac{\partial \omega w}{\partial z} \right) \\ & = \frac{\partial}{\partial x} \left(\Gamma_\omega \frac{\partial \omega}{\partial x} \right) + \frac{\partial}{\partial y} \left(\Gamma_\omega \frac{\partial \omega}{\partial y} \right) + \frac{\partial}{\partial z} \left(\Gamma_\omega \frac{\partial \omega}{\partial z} \right) + G_\omega - Y_\omega + D_\omega + S_\omega \end{aligned} \quad (39)$$

The equations are very similar to the k- ω turbulence model with the exception of the \widetilde{G}_k and D_ω terms and some other differences. The turbulent viscosity equation was modified from the original k- ω turbulence model along with the turbulent Prandtl numbers in the effective diffusivity equation from the standard model.

$$\mu_t = \frac{\rho k}{\omega} \frac{1}{\max \left[\frac{1}{a^*}, \frac{SF_2}{a_1 \omega} \right]} \quad (40)$$

$$\sigma_k = \frac{1}{\frac{F_1}{\sigma_{k,1}} + \frac{1 - F_1}{\sigma_{k,2}}} \quad (41)$$

$$\sigma_\omega = \frac{1}{\frac{F_1}{\sigma_{\omega,1}} + \frac{1 - F_1}{\sigma_{\omega,2}}} \quad (42)$$

where, a^* is from the original k - ω equation, a_1 is a model constant that is equal to 0.31, S is the strain rate magnitude, represented in tensor notation in (43).

$$S = \sqrt{\left(\frac{\partial u_j}{\partial x_i} + \frac{\partial u_j}{\partial x_i}\right)\left(\frac{\partial u_j}{\partial x_i} + \frac{\partial u_j}{\partial x_i}\right)} \quad (43)$$

$\sigma_{k,1}$, $\sigma_{k,2}$, $\sigma_{\omega,1}$, $\sigma_{\omega,2}$ are model constants equal to 1.176, 1, 2, and 1.168 respectively. F_1 is a blending function to tradeoff between the useful parts of the k - ε and k - ω models.

$$F_1 = \tanh\left(\left(\min\left[\max\left(\frac{\sqrt{k}}{0.09\omega}, \frac{500\mu}{\rho y^2\omega}\right), \frac{4\rho k}{\sigma_{\omega,2}D_{\omega}^+y^2}\right]\right)^4\right) \quad (44)$$

The y value is the distance between the point and the next surface with D_{ω}^+ representing is the absolute part of the D_{ω} term.

$$D_{\omega}^+ = \max\left[\frac{2\rho}{\sigma_{\omega,2}\omega}\left(\frac{\partial k}{\partial x}\frac{\partial \omega}{\partial x} + \frac{\partial k}{\partial y}\frac{\partial \omega}{\partial y} + \frac{\partial k}{\partial z}\frac{\partial \omega}{\partial z}\right), 10^{-10}\right] \quad (45)$$

The G_{ω} term was also modified and is based on the value of \widetilde{G}_k .

$$G_{\omega} = \frac{\alpha}{v_t}\widetilde{G}_k \quad (46)$$

The \widetilde{G}_k term is still the turbulent kinetic energy generation caused by the mean velocity gradients, but has been modified to choose the minimum value between the original standard k - ω G_k term and a term that is highly dependent on the turbulent Reynolds number based on the presence of the β^* term that is the same as the original k - ω model constant that was already discussed.

$$\widetilde{G}_k = \min(G_k, 10\rho\beta^*k\omega) \quad (47)$$

α is still evaluated in the same expression as the standard model, but the α_{∞} term moved from being a constant to variable based on the expression shown.

$$\alpha_{\infty} = F_1\alpha_{\infty,1} + (1 - F_1)\alpha_{\infty,2} \quad (48)$$

where,

$$\alpha_{\infty,1} = \frac{\beta_{i,1}}{\beta_{\infty}^*} - \frac{0.41^2}{\sigma_{\omega,1}\sqrt{\beta_{\infty}^*}} \quad (49)$$

$$\alpha_{\infty,2} = \frac{\beta_{i,2}}{\beta_{\infty}^*} - \frac{0.41^2}{\sigma_{\omega,2}\sqrt{\beta_{\infty}^*}} \quad (50)$$

where $\beta_{i,1}$ and $\beta_{i,2}$ are model constants equal to 0.075 and 0.0828 respectively.

The Y_k term is evaluated similar to the way it was in the standard model, however there is no piecewise function f_{β^*} , the term is a constant value of 1 for the k- ω SST turbulence model. The Y_{ω} term was modified in a similar way for the f_{β^*} term, but the β_i equation transformed into a variable where it was previously a constant in the standard model.

$$\beta_i = F_1\beta_{i,1} + (1 - F_1)\beta_{i,2} \quad (51)$$

D_{ω} is defined as a cross-diffusion term.

$$D_{\omega} = 2(1 - F_1)\rho \left(\frac{1}{\omega\sigma_{\omega,2}} \right) \left(\frac{\partial k}{\partial x} \frac{\partial \omega}{\partial x} + \frac{\partial k}{\partial y} \frac{\partial \omega}{\partial y} + \frac{\partial k}{\partial z} \frac{\partial \omega}{\partial z} \right) \quad (52)$$

RANS solvers are highly used to predict wind turbine performance, but there is a flaw in the RANS methods for vortex shedding and highly separated flow. Even with the flaw, the RANS solvers can often predict key performance characteristics such as power production (Thé & Yu, 2017). For this work, the solver of choice is the k- ω SST turbulence model.

The solver schemes used in ANSYS-Fluent[®] are also important and will be discussed in Chapter 3.

The discretization of these equations in the computational domain is also important. The first-order upwind scheme discretizes cells for use in the RANS equations with respect to the neighboring cells. The idea is that the center cell is representative of the average value throughout the whole cell meaning that the interface quantities in between nodes have the same values as the cell. For example, in a 1-D problem, the interface between node two and node one will have the value of node two-the upwind node. The scheme generates a stable solution, but

only has first-order accuracy relative to the Taylor series truncation error and can cause false diffusion. False diffusion is the spreading of transported properties with a diffusion like presence (ANSYS Inc., 2011; Malalasekera & Versteeg, 2006).

A second-order upwind scheme is similar to the first-order scheme, but it achieves second-order accuracy through another Taylor series expansion of the central cell. Whereas in the first order approach the leading node determined the interface value, in the second order approach, the interface value is found from the center cell result and the scalar result of the gradient of the cell in front and the displacement vector between the front cell centroid and the interface centroid (ANSYS Inc., 2011; Barth & Jespersen, 1989).

The quadratic upstream interpolation for convective kinetics (QUICK) scheme is more suited for structured hexahedral meshes that can bring better than second-order accuracy and up to third-order Taylor series accuracy on a uniform structured mesh and can dramatically reduce the presence of false diffusion, but it has the drawback of being conditionally stable-primarily caused by negative flow in the system. The QUICK scheme makes use of a quadratic upstream weighted interpolation for cell interface values. The points that define the quadratic are the upstream interface and the node values outside of the previous interface (Malalasekera & Versteeg, 2006). In ANSYS, the QUICK schemes are based on a similar principle, where they are modified by the weighted average of second-order upwind and central interpolations of a flow variable with a curvature correction with a constant of $1/8$. Since QUICK schemes are more suited for structured hexahedral meshes as previously stated, ANSYS-Fluent[®] allows for its use in unstructured meshes by utilizing a second-order upwind scheme for interfaces of non-hexahedral cells and partition boundaries for parallel processing (ANSYS Inc., 2011; Leonard & Mokhtari, 1990).

1.3 General Turbine Losses

There are several loss factors equated to the generator that are not taken into account from calculations. Using results from a 5 MW wind turbine the generator efficiency of a wind was broken down into several key loss components within the generator mainly mechanical and electrical. The mechanical losses are gear loss, bearing loss and windage loss. Gear loss is power lost by the gearing from turbine to generator, and is dependent on the number of stages in the gearbox (q).

$$P_g = 0.01qP_{mR} \quad (53)$$

Bearing loss is the power lost due to mechanical friction from rotor rotation.

$$P_{bl} = \frac{\gamma M_r D_r}{2} \omega \quad (54)$$

where γ is the friction coefficient, M_r is equal to the sum of the weight of the rotor and about half of the weight of the generator (De Kooning et al., 2016).

Windage loss is caused by friction of air going over the rotor.

$$P_{wl} = K_w \omega^2 \quad (55)$$

where K_w is dependent on the rotor shape, the rotor length and rotating speed. Other losses include the electrical losses known as iron, copper, stray load, power converter, and transformer losses. Iron loss involves of eddy current loss and hysteresis loss. Copper losses are resistance losses in the copper winding coils. Stray load loss is a loss by variation of load. Transformer loss is a resistance loss. Overall the total efficiency for a 5 MW wind turbine was around 95% past the rated output speed. For flows at the cut in speed and other ramp up speeds, the efficiency was variable ranging from 0 at the cut in speed to about 90% (Tamura, 2012). The rating of the wind turbine used in this work was 500 W- a difference in magnitude by 5 orders- meaning that

applying the losses associated with the large wind turbine to the wind turbine is not really straightforward.

De Kooning et al. (2016) that was trying to improve power generation by incorporating rotating speed control based on inefficiencies of wind turbines for small scale and medium scale wind turbines rated at 300 kW and below. In the group's MATLAB[®] based simulation, it was determined that mechanical efficiency was mainly dependent on torque and was around 96% for high torque values and around 70% for low torque values. The generator efficiency for relatively high constant speed, torque and power was found to be between 70% and 80% (De Kooning et al., 2016). The work of the group was for a turbine with a diameter of 2.54 meters- 3.63 times the size of the wind turbine that this research is concerned with.

Grauers (1996) tried to characterize generator efficiencies for three different types of generators at multiple wind speeds for 500 kW systems. System 1 consisted of a four pole induction generator that has a gearbox. System 2 consisted of a multiple speed synchronous generator that has a gear box and frequency converter. System 3 consists of a directly driven multiple speed generator with a frequency converter. The overall efficiencies that were calculated included friction and windage losses as well. The average wind speeds were broken up into several categories from low to medium to high with the average wind speeds for each of those being 5.3 m/s, 6.6 m/s, and 7.8 m/s. The wind speed regions are somewhat similar to the range of this research; 4-8 m/s wind speeds. For low wind speed, system 3 had the highest average efficiency of 86.4%, with system 1 and 2 having efficiencies of 82% and 84% respectively. For medium wind speed, system 3 had the highest average efficiency yet again at 88.8% with systems 1 and 2 having 87.3% and 86.8% efficiencies respectively. For high wind speeds, system 3 had the highest average efficiency at 89.9% efficiency while systems 1 and 2

had 89.7% and 88.1% efficiencies respectively. For the operation at the rated load of each generator, system 1 was 93.8%, system 2 was at 90.6%, and system 3 was at 91.6% (Grauers, 1996). The scope of this research is mainly of interest because it is undetermined which generator was used in the original experiment from Ohya et al. (2008) and it is being used to attempt to estimate the efficiency of the wind turbine power generation. The average efficiencies for system 1, 2, and 3 were 86.3, 86.3, and 88.36 respectively.

Overall the general losses for the research of this project can only be roughly estimated. It is understood that the low amount of torque created by the system could have an impact on the mechanical efficiency. Higher rotational speed creates more iron losses however lower torque results in less copper losses (De Kooning et al., 2016). Without exact characteristics of the turbine that was used in the experiment along with the added rotating speed and wind speed from the shroud, the general efficiency losses of the wind turbine in this research can only be roughly estimated. On the low end if generator efficiencies are around 0.7 and mechanical efficiencies are 0.7, the overall efficiency would be reduced to 0.49. However, on the high end, if generator efficiencies are within 90% and mechanical efficiencies are within 96%, then the overall efficiency would be 0.864. If the performance is similar to the generator experiments, then efficiency of the system could be on the order of 87% conditionally based on the generator type for the experiment. There is a broad range for the efficiency, but it is mainly because most of the inefficiencies present are hard to measure even when the wind turbine is available and also can change based on operating conditions, especially with the added complications of the shroud.

1.4 Objectives

There are two primary objectives of this work. First, the blade element and momentum theory (BEMT) is used to find the blade geometry for a wind turbine. Second, this work uses

computational fluid dynamic (CFD) modeling to verify the blade geometry by comparing the torque results from the numerical model with the available experimental data.

1.5 Organization

This work is broken up into two parts. Part I, Chapter 2, goes over the blade element and momentum theory (BEMT) and its MATLAB[®] implementation into a code that computes blade coordinates and chord distribution of the wind turbine. Part II, Chapters 3 and 4, goes over the adaptation of Part I into a three-dimensional domain formed into a numerical model using ANSYS-Fluent[®] to test the effectiveness of the BEMT code by comparing the results of torque to experimental data. Chapter 3 primarily goes over the specifications of numerical model developed in ANSYS-Fluent[®]. Chapter 4 goes over the results of the numerical model and compares the torque values generated by the model to the experimental power production. Chapter 5 concludes the results and recommends future work.

The Blade Element and Momentum Theory

2.1 Method and Procedure

The blade element and momentum theory (BEMT) is based on the idea of modeling a wind turbine as a control volume that is a thin rotor disk and using linear momentum conservation to solve key parameters of a thin blade segment. The theory's makes certain assumptions: fluid flow is steady state, incompressible, homogeneous, with no frictional drag, uniform thrust over entire rotor area, an infinite number of blades, and the far upstream and far downstream pressures are equal to the same environmental pressure. The biggest shortcoming with this method is the infinite number of blades assumption as it translates to no 3D flow effects, primarily that each blade segment is not affected by its neighbor. To reduce the effects of the bold assumptions, there are multiple correction factors that will be discussed later. The overall method from "Wind Energy Explained: Theory, Design, and Application" by Manwell et al. (2002) is described as follows:

1. Choose the amount of power needed from blade.
2. Choose initial λ . For power generation, lambda should be between 4 and 10.
3. Choose number of blades based on λ . For a lambda greater than 4, 1-3 blades are appropriate.
4. Select airfoil.
5. Obtain lift and drag curves for airfoil chosen and find AOA of maximum lift to drag ratio value for each segment.
6. Divide the blade into N elements, typically about 10 to 20.
7. Find initial λ_n values.

$$\lambda_n = \lambda \left(\frac{r_n}{0.5D_r} \right) \quad (56)$$

8. Find initial ϕ_n values.

$$\phi_n = \frac{2}{3} \arctan\left(\frac{1}{\lambda_n}\right) \quad (57)$$

9. Find theoretical chord distribution.

$$c_n = \frac{8\pi r_n (1 - \cos(\phi_n))}{Z_b c_{l_{max,n}}} \quad (58)$$

10. Obtain the twist of the blade and find θ_n for each segment.

11. Adjust the initial values of ϕ_n .

$$\phi_n = \theta_{p,n} + \alpha_{\text{optimal},n} \quad (59)$$

12. For ease of assembly, linearize c_n and θ_t if possible.

13. Find σ'_n .

$$\sigma'_n = \frac{Z_b c_n}{2\pi r_n} \quad (60)$$

14. Given the initial conditions there are two ways to solve for the blade geometry.

a. The first solving scheme involves solving for C_l and alpha iteratively or graphically. For brevity this method is not included.

b. The second solving scheme involves iteratively solving for the axial and angular induction factors.

15. Following the second solving scheme. Using initial ϕ_n values find initial values for a_n and a'_n .

$$a_n = \frac{1}{1 + \frac{4 \sin^2 \phi_n}{(\sigma'_n c_{l_{\max},n}) \cos(\phi_n)}} \quad (61)$$

$$a'_n = \frac{1 - 3a_n}{4a_n - 1} \quad (62)$$

16. With initial values, iterations begin with re-solving for ϕ_n

$$\phi_n = \arctan\left(\frac{1 - a_n}{(1 + a'_n)\lambda_n}\right) \quad (63)$$

17. Find adjusted α_n .

$$\alpha_n = \phi_n - \theta_{p,n} \quad (64)$$

18. Calculate $C_{l,n}$ and $C_{d,n}$ from α_n

19. Compute tip loss factor $F_{t,n}$ (Manwell et al., 2002).

$$F_{t,n} = \frac{2}{\pi} \arccos\left(e^{\frac{(-\frac{Z_b}{2})(1 - \frac{r_n}{0.5D_r})}{\frac{r_n}{0.5D_r} \sin(\phi_n)}}\right) \quad (65)$$

20. There is actually a secondary loss factor to account for loss of torque at the hub known as the hub loss factor $F_{h,n}$ that is not listed in the reference textbook (Liu & Janajreh, 2012).

$$F_{h,n} = \frac{2}{\pi} \arccos\left(e^{\frac{(-\frac{Z_b}{2})(r_n - 0.5D_h)}{r_n \sin(\phi_n)}}\right) \quad (66)$$

21. The hub and tip losses are multiplied together to form one correction term F_n .

$$F_n = F_{t,n} F_{h,n} \quad (67)$$

22. With the added correction, the solution method follows “Wind Energy Explained: Theory, Design, and Application” by Manwell et al. (2002), yet again. The next step is to find the local thrust coefficient $C_{T,n}$.

$$C_{T,n} = \frac{\sigma'_n(1 - a_n)^2(C_{l,n} \cos(\phi_n) + C_{d,n} \sin(\phi_n))}{\sin^2(\phi_n)} \quad (68)$$

23. For each blade section, if the local thrust coefficient is less than 0.96, then the new value of the axial induction factor is calculated from (68).

$$a_n = \frac{1}{1 + \frac{4F_n \sin^2 \phi_n}{\sigma'_n C_{l,n} \cos \phi}} \quad (69)$$

24. For each blade section, if the local thrust coefficient is greater than 0.96, then the new value of the axial induction factor is determined from equation (69).

$$a_n = \frac{1}{F_n} (0.143 + \sqrt{(0.0203 - 0.6427(0.889 - C_{T,n}))}) \quad (70)$$

25. Calculate the angular induction factor.

$$a'_n = \frac{1}{\frac{4F_n \cos \phi_n}{\sigma'_n C_{l,n}} - 1} \quad (71)$$

26. The previous ten steps are iterated until a convergence criterion is reached such as a difference between the current value and the past value of $1e-6$.
27. Next the power coefficient, thrust per element, and torque per element can be determined from the equation below.

$$C_p = \frac{8}{\lambda N} \sum_{n=1}^n F_n \sin^2(\phi_n) (\cos(\phi_n) - \lambda_n \sin(\phi_n)) (\sin(\phi_n) + \lambda_n \cos(\phi_n)) \left(1 - \frac{C_{d,n}}{C_{l,n}} \cot \phi_n\right) \lambda_n^2 \quad (72)$$

$$dF_{\text{thrust}} = 4F_n \rho U_\infty^2 a_n (1 - a_n) \pi r dr \quad (73)$$

$$dQ = 4F_n a'_n (1 - a_n) \rho U_\infty \pi r^3 \omega dr \quad (74)$$

28. Adjustments may be required to get desired values. (Manwell et al., 2002)

The above steps are summarized in Figure 8:

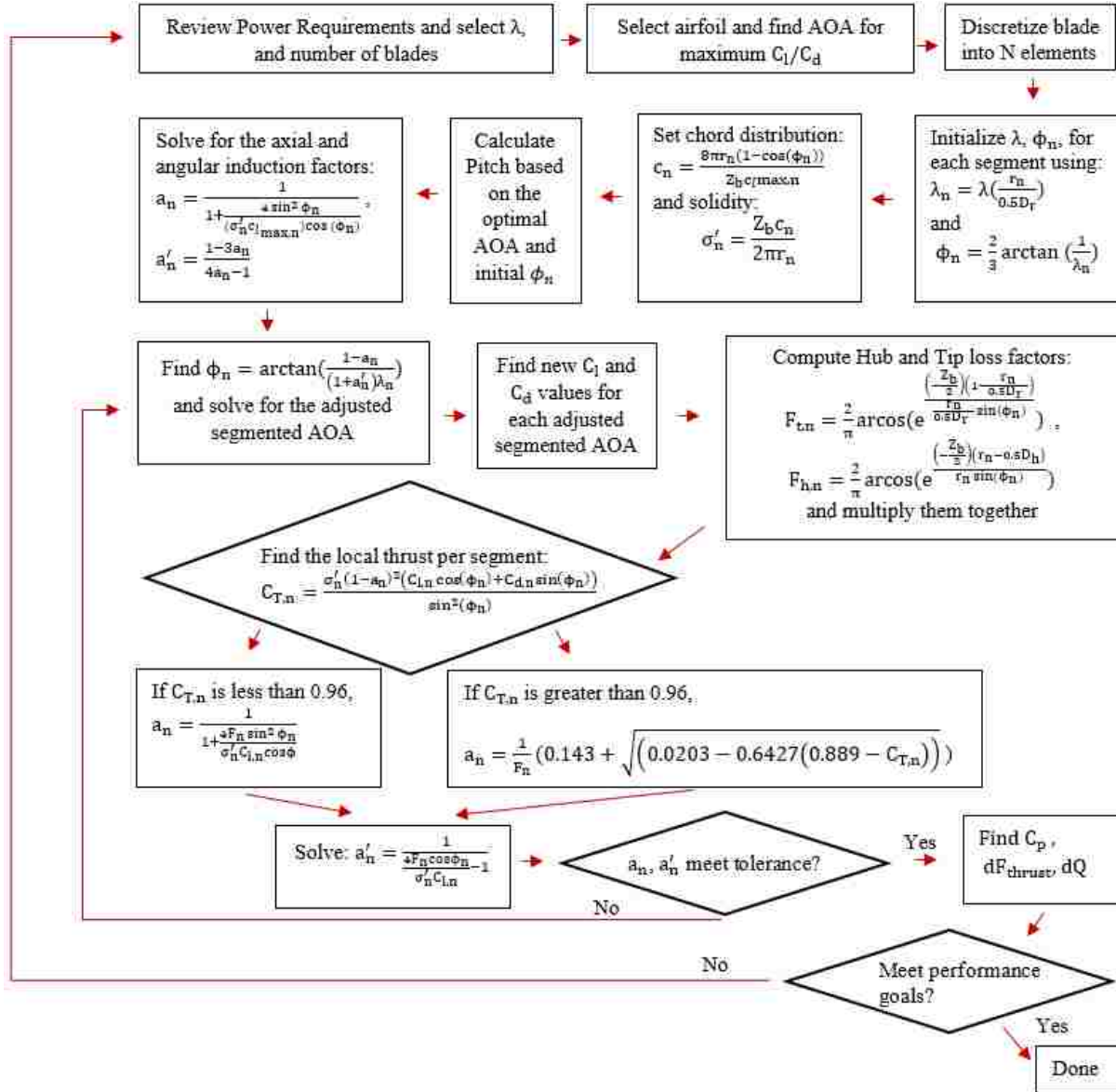


Figure 8: BEMT flow chart

It should be noted that because of the assumptions that are made, the BEMT has an uncertainty of about 20% for blade loading (Snel, 2003; Thé & Yu, 2017).

2.2 MATLAB® Implementation

The entire MATLAB® code is included in Appendix A. The MATLAB® code follows the same construction as the flow chart shown in Section 2.1. The power requirements were set to be

identical to the experimental power performance from Ohya et al. (2008), shown in Figure 9 where the power coefficient is equal to 0.35.

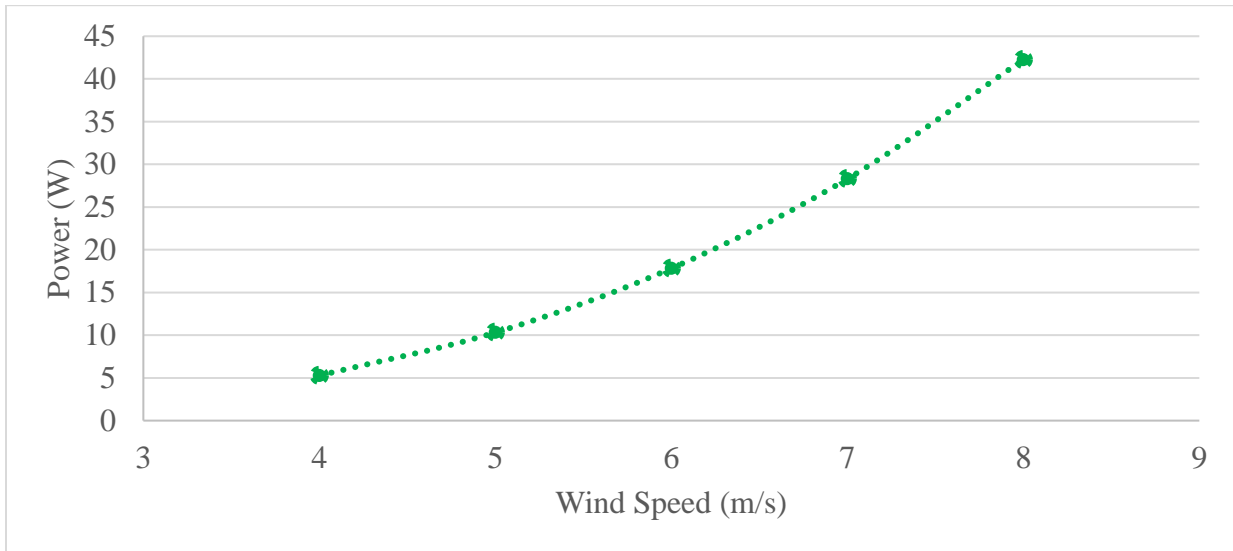


Figure 9: Power generation for bare wind turbine from Ohya et al. (2008)

Based on the data above, the comparative parameters that the results of the numerical model in this work will be compared to are summarized in Table 2.

Table 2: Summary of power, rotating speed, and torque for bare vs. shrouded wind turbine

Wind Speed (m/s)	Bare Power (W)	Bare ω (rad/s)	Bare Torque (N-m)
4	5.280	48	0.110
5	10.312	60	0.171
6	17.820	72	0.247
7	28.297	84	0.336
8	42.240	96	0.440

The shrouded data in the table above is based on the actual experimental results from Ohya et al. (2008). The torque and rotating speeds are estimates based on the tip-speed-ratio (TSR). As

mentioned the optimal TSR for the shrouded turbine was 4.2. To compensate for the extra incoming velocity caused by the shroud, the rotating speed will increase along with the velocity. The shroud amplification factor (SAF) from Ohya et al. (2008) was around 1.3 for the shrouded wind turbine compared to 0.8 for the bare wind turbine producing a power increase by a factor of about 4 to 5. Based on the value of four for a conservative estimate and power is related to the cubic wind speed, the SAF in the code and table was chosen to be 1.59- the cubed root of the power increase. The shrouded portion of the data will be left for future work, so the data of concern is the bare power and torque. The rotating speed and torque were also found from the 0.35 power coefficient curve for the bare wind turbine using the traditional TSR equation without any amplification factors being applied. For this work, only three wind speeds are simulated due to either low power generation for lower speeds or lack of data for higher wind speeds- 4 m/s, 6 m/s, and 8 m/s. The code is run for the value of 6 m/s to generate the blade for all numerical simulations.

The airfoil used in the experiments by Ohya et al. (2008) was not specifically mentioned other than saying it was a 63-2 type airfoil. However, the airfoil was discovered to be a NACA 63-210 airfoil in another work on shrouded wind turbine testing that reference Ohya et al. (2008) work (Kosasih & Tondelli, 2012).

The NACA 6 series digits meaning is a more complex airfoil compared to other NACA airfoils. For the NACA 63-210 airfoil, the first digit indicates the series, the second digit indicates distance from the leading edge in tenths of a chord to the minimum pressure, the third digit indicates the design lift in tenths, and the final two digits give the thickness in percentage of chord (Abbott et al., 1945). Overall the NACA 63-210 airfoil has the minimum pressure occur at 30% chord, the design lift coefficient is 0.2, the maximum thickness is 10% chord at 35% chord

length, and the maximum camber is 1.1% at 60% chord length (Abbott et al., 1945; “NACA 63-210 AIRFOIL (n63210-il),” 2018).

The coordinates for the airfoil were taken from a website run by the University of Illinois at Urbana-Champaign (UIUC) airfoil coordinates website (University of Illinois at Urbana-Champaign, 2018). The coordinates are summarized in the Table 3.

Table 3: NACA 63-210 airfoil coordinates data

Upper airfoil		Lower airfoil	
x	y	x	y
0	0	0	0
0.00430	0.00876	0.00570	-0.0078
0.00669	0.01107	0.00831	-0.0097
0.01162	0.01379	0.01338	-0.0117
0.02398	0.01939	0.02602	-0.0157
0.04886	0.02753	0.05114	-0.0212
0.07382	0.03372	0.07618	-0.0252
0.09882	0.03877	0.10118	-0.0284
0.14890	0.04665	0.15110	-0.0332
0.19902	0.05240	0.20098	-0.0365
0.24917	0.05647	0.25083	-0.0386
0.29933	0.05910	0.30067	-0.0397
0.34951	0.06030	0.35049	-0.0397
0.39968	0.06009	0.40032	-0.0387
0.44985	0.05861	0.45015	-0.0367
0.50000	0.05599	0.50000	-0.0339
0.55013	0.05235	0.54987	-0.0305
0.60024	0.04786	0.58976	-0.0264
0.65032	0.04264	0.64968	-0.0220
0.70036	0.03684	0.69964	-0.0174
0.75038	0.03061	0.74962	-0.0127
0.80036	0.02414	0.79964	-0.0082
0.85030	0.01761	0.84970	-0.0042
0.90021	0.01212	0.89979	-0.0009
0.95010	0.00530	0.94990	0.0012
1	0	1	0

The airfoil coordinates were used by another website that utilized the command window based panel method software known as Xfoil to generate the lift and drag coefficients for the 63-210 airfoil based on the coordinates from Table 3 (“NACA 63-210 AIRFOIL (n63210-il),” 2018). Xfoil was developed by Drela and Youngren (2000) for to model subsonic airfoils. It should be noted that the use of Xfoil to generate lift and drag data is commonly used with BEMT codes, examples of which being from Hsiao et al. (2013) and Zhu et al. (2014). Based on the velocity, the maximum chord length of approximately 0.12 meters, and the standard operating conditions for air at standard sea level, the Reynolds number was estimated to be around 50,000. Due to the nature of the low Reynolds number, experimental testing data in that range was very difficult to find, and only Reynolds number of approximately 1,000,000 had data for lift and drag (Ilk, 1947). Some validation testing was done using ANSYS-Fluent[®] with the results of which being in Section 3.3. From the lift and drag coefficient data from the Xfoil predictions, sixth order polynomials were created to simulate the lift and drag. The polynomials generated for lift and drag were $C_l = 1e-06\alpha^6 - 3e-05\alpha^5 - 0.0001\alpha^4 + 0.002\alpha^3 + 0.0068\alpha^2 + 0.0697\alpha - 0.0365$ and $3e-08\alpha^6 + 2e-07\alpha^5 + 9e-06\alpha^4 - 8e-05\alpha^3 + 3e-05\alpha^2 + 0.0018\alpha + 0.0216$ respectively. The coefficient of determination for the lift was 0.9903 and drag was 0.9745. The maximum lift value was 9.75 degrees for the data with the minimum value being -8.5.

Following Figure 8’s progression, the blade is discretized into 50 segments to get a reasonable resolution between 2D segments. Next the axial induction factor, angular induction factor, along with the bare power coefficient, torque per segment, thrust per segment, and the loss factor matrices are initialized to be zeroes matrices of 2 by 50 dimensions. A blank matrix to contain the blade coordinates is also initialized.

Next the lift and drag data mentioned already is entered to find the maximum lift to drag ratio. Based on the optimal alpha value, the initial AOA matrix is set from a value slightly above the optimal angle of attack to 95% of the optimal AOA. The larger value at the base of the airfoil is done because it is known that larger angles of attack are present at the base due to the need for structure over lift- mainly because at the base, the moment arm of the airfoil turning the blade is so low that it is less impactful on the running of the turbine blade. The value of 95% of the optimal airfoil at the tip of the blade is mainly for improved convergence because the data is limited to a maximum AOA of 9.75 degrees. Once the AOA matrix is initialized, the lift and drag coefficients are calculated to polynomials already mentioned. With the values of alpha, the coefficients of lift and drag calculated, the segmented TSR, and segmented flow inlet angle can be calculated using the initial equations in step four of the BEMT flow chart as shown in Figure 8. The chord distribution is calculated along with the blade solidity. As a check to verify the Reynolds number is within the operating range for the majority of the blade segments, the Reynolds number is calculated for each segment. The twist is calculated based on the optimal AOA and initialized phi values. Following step seven of the flow chart, the initial values of the angular and axial induction factors are calculated.

Because MATLAB[®] index arrays start at 1 instead of zero, the first iteration value is set to one. The maximum number of iterations is set utilizing a MATLAB[®] based function called maxit. The maxit condition is set to 5000 to limit the total number of iterations to 5000 total iterations. The initialized values are then fed into a while 1 loop that continues the iterations until the 1e-6 tolerance value is met for the axial induction factor and angular induction factor. The code is also terminated if the value of phi becomes imaginary.

Based on the initialized values, the new flow inlet angle is calculated. There are two correction values applied at the first value and second value due to the nature of the values having no torque based on the tip and hub loss factors. The correction factors interpolate the initial value and final value to maintain the blade coordinates at the tip and hub. The new AOA is then calculated and the lift and drag coefficients are calculated yet again.

The hub and tip losses are then calculated followed by the segmented thrust coefficient. Like step 11 of the BEMT flow chart, the thrust coefficient value goes through an if statement that identifies if the segmented thrust coefficient is greater than or equal to 0.96- the value is such because it indicates where the BEMT model begins to break down. A value of 1 for the thrust coefficient indicates that the axial induction factor is 0.5 meaning that the flow velocity has dropped to zero behind the rotor (Manwell et al., 2002). The axial induction factor is solved based on the value of thrust coefficient based on the equations discussed in Section 2.1.

Once the new axial and angular induction factors are calculated, the power coefficient is then determined for the power coefficient and torque are calculated according by summing up the sectional lift and power coefficients.

Next, a measure to improve convergence is added. It is well known that the BEMT method runs into convergence issues frequently. To alleviate this, the values of the current and previous induction factors are averaged together. If the tolerances for the new values of the axial and angular induction factors match the absolute tolerance of $1e-6$, then the while 1 loop breaks. If the solution is not within tolerance, then the new axial induction factors are used to find the new flow inlet angle and the whole process is repeated again.

Once the solution has converged, the AOA, flow inlet angle, and pitch are plotted as shown in Figure 10.

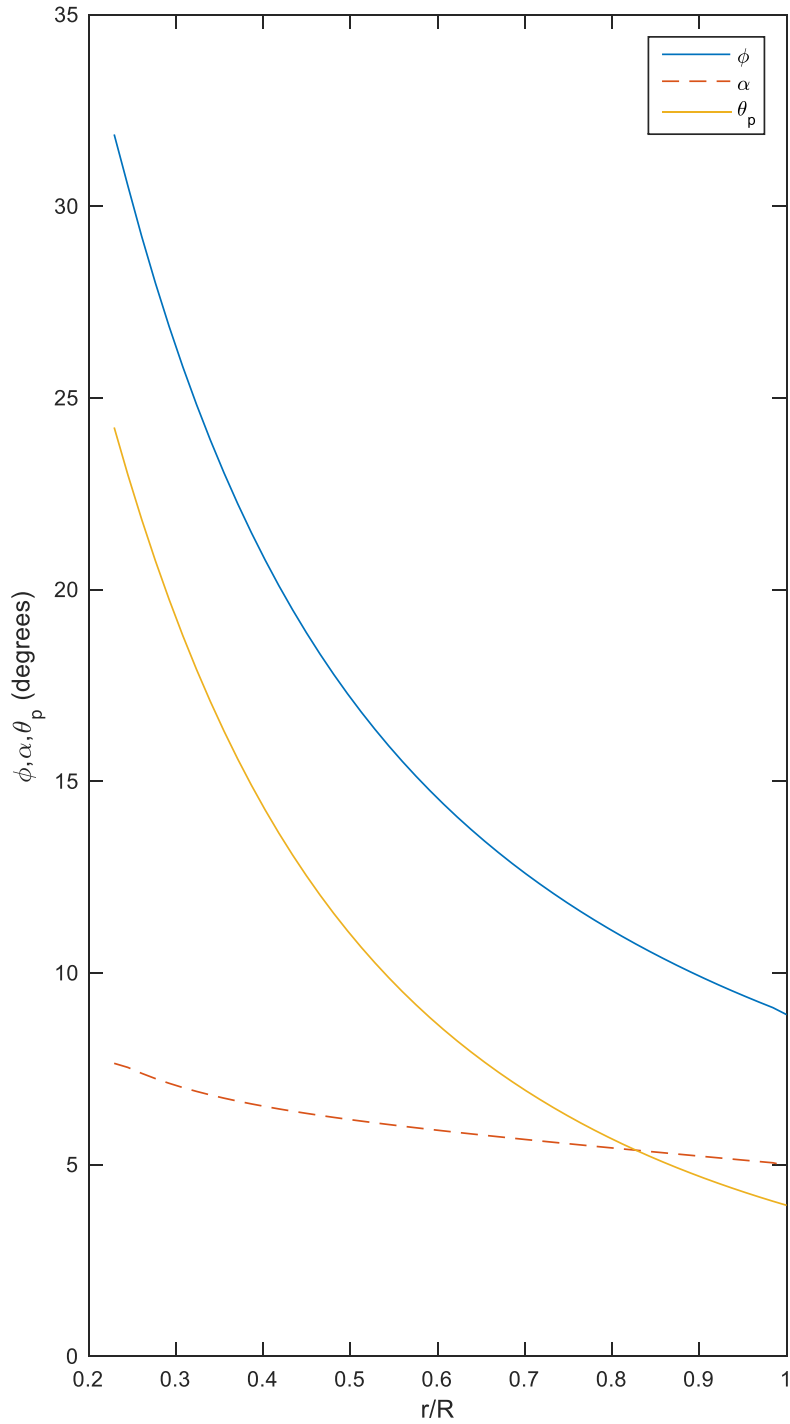


Figure 10: AOA, flow inlet angle, and pitch of turbine blade vs. rotor position

The angle of attack is higher at the base of the blade and tapers off at the tip from 7.644 degrees to 4.9745 with the average AOA being around 5.99 degrees. Compared to the optimal angle of

attack of 5.25 degrees, the angles seem reasonable. The trends of pitch and flow inlet angle decreasing as the blade tapers to the tip is also consistent with other wind turbines. In a related work from the research group in Japan for a rotor that was only about half the size of the current wind turbine- a 0.388 m rotor diameter-the blade settings were consistent for the angle of attack, but the angle of twist was around 30 degrees compared to the MATLAB[®] output of 20.29 degrees and the flow inlet angle ranged from about 50 degrees to 18 from the base to tip. The differences are most likely attributed to the different rotor diameter and tip-speed-ratio used- 2.8 compared to the value used in the code of 4.2 (Abe et al., 2005).

The next output of the code was a check of the axial and angular induction factors along with the thrust coefficient as shown in Figure 11.

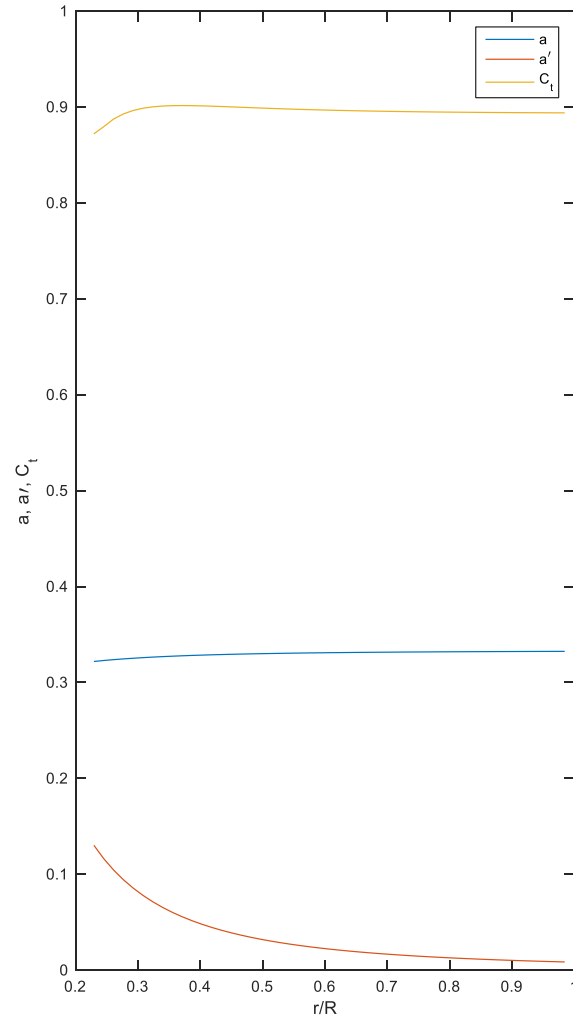


Figure 11: Axial induction factor (a), angular induction factor (a'), thrust coefficient (C_t) vs. rotor position

As mentioned previously, the BEMT breaks down when the thrust coefficient equals 1, indicating that there is reversed flow behind the turbine blade. The thrust coefficient shown in Figure 11 remains around 0.9 meaning that the theory is still plausible. The optimal value for the axial induction factor is around one-third based on the Betz limit, which makes the values shown in Figure 11 reasonable (Manwell et al., 2002). Ideally, in a rotor without wake rotation, the angular induction factor is close to zero. The chord distribution used in the code is meant for a blade with some wake rotation, so the results are consistent.

Next the lift and drag components were plotted as a general check to ensure that lift was not negative at any point of the blade and that drag wasn't significant at any portion of the blade.

The lift and drag coefficients are shown in Figure 12.

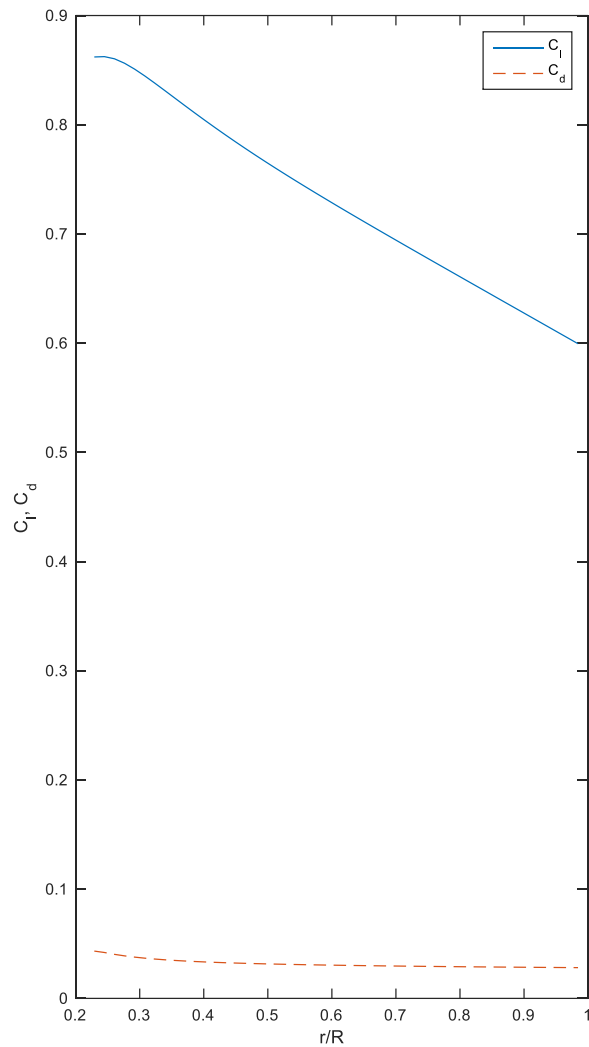


Figure 12: Lift and drag coefficients vs. rotor position

The downward slope of the lift curve can be attributed to the decreasing chord length from the base to the tip of the blade. The drag is relatively stable throughout most of the angles of attack, so the relatively flat shape is consistent. Based on the average of both the lift and drag

coefficients across the wingspan, the average lift coefficient should be 0.727 and the average drag coefficient should be 0.0316 creating an average lift to drag ratio of about 23.

The next plot produced is a power check shown in Figure 13 to show the amount of power generated by standard BEMT practices- for the bare wind turbine approximation.

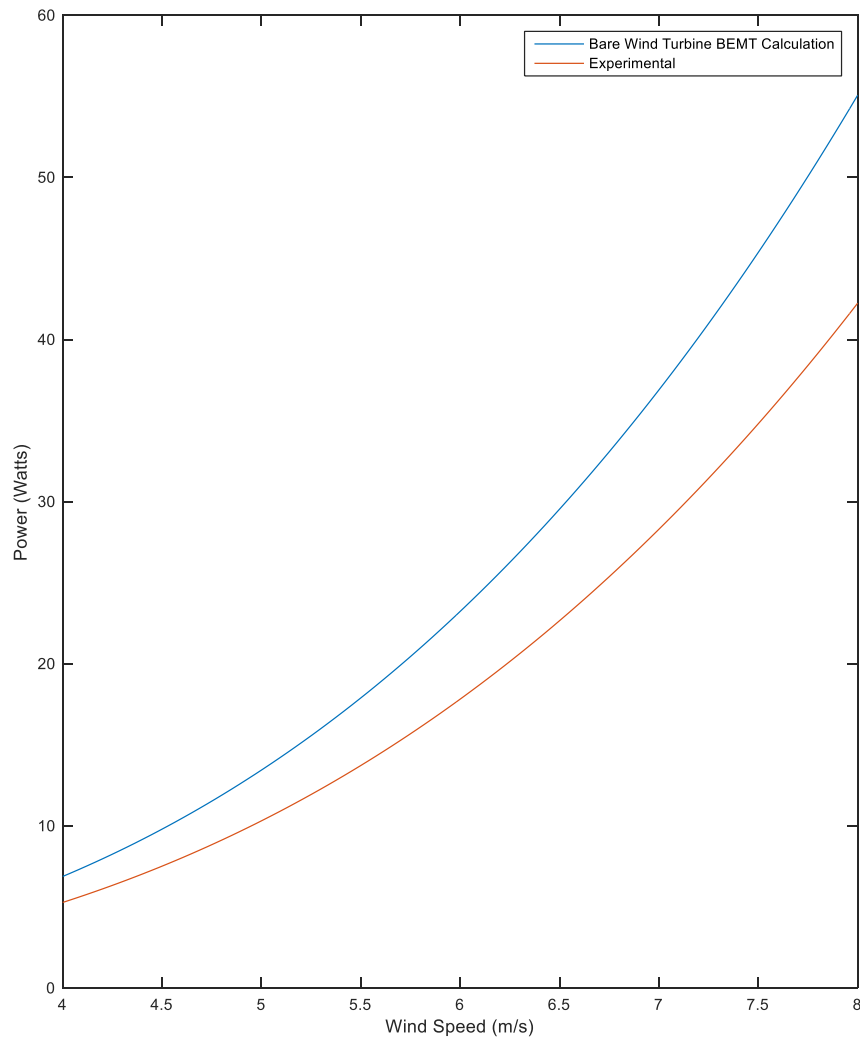


Figure 13: Power vs. wind velocity

As mentioned previously the BEMT has a wide range of error, due to the assumptions made. The green line represents the experimental power consistent with a power coefficient of 0.35. The blue line represents the approximation by the BEMT code for power generated by a bare wind turbine. The power coefficient associated with the BEMT approximation is 0.4563 which shows

a 30.4 percent difference from the actual result. Numerical results are typically larger than the actual results, and given the large uncertainty of the BEMT method, the result appears reasonable.

Next in the code, the various outputs such as torque and power for a wind speed of 6 m/s as well as rotating speed for both the bare wind turbine are given to be compared to the simulation. The outputs are shown at the end of Appendix A.

Next the base NACA 63-210 blade coordinates are multiplied by the local chord length calculated previously for each section. The new coordinates are then aligned to have the center at 0.25 chord length to become the pitch axis, a practice that is common for turbine blades (Bazilevs et al., 2011; Jonkman et al., 2009). Once each segment is set with a chord about its new aerodynamic center, the coordinates are transformed to align with the local pitch for each segment. The results are shown in Figures 14 and 15 shows the top view and side view of the blade coordinates.

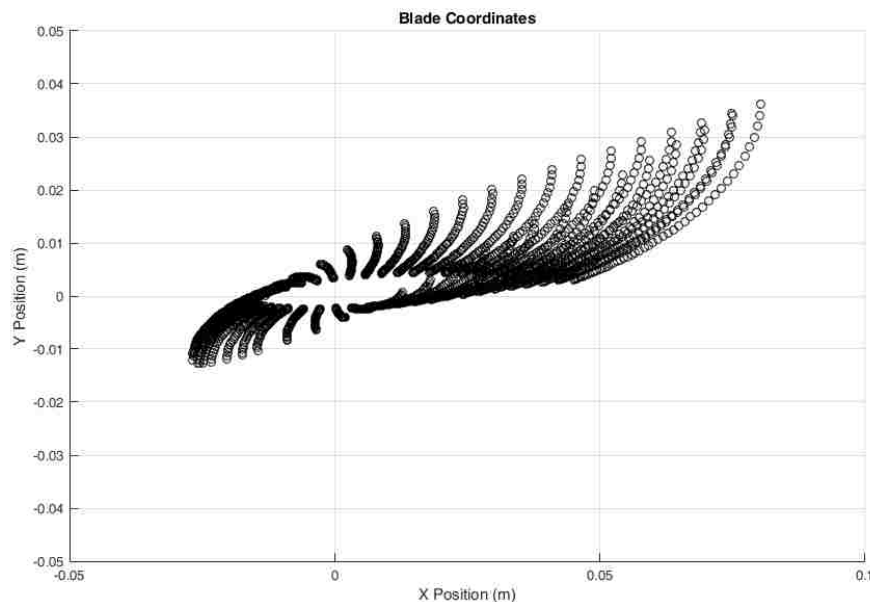


Figure 14: Top view of blade coordinates

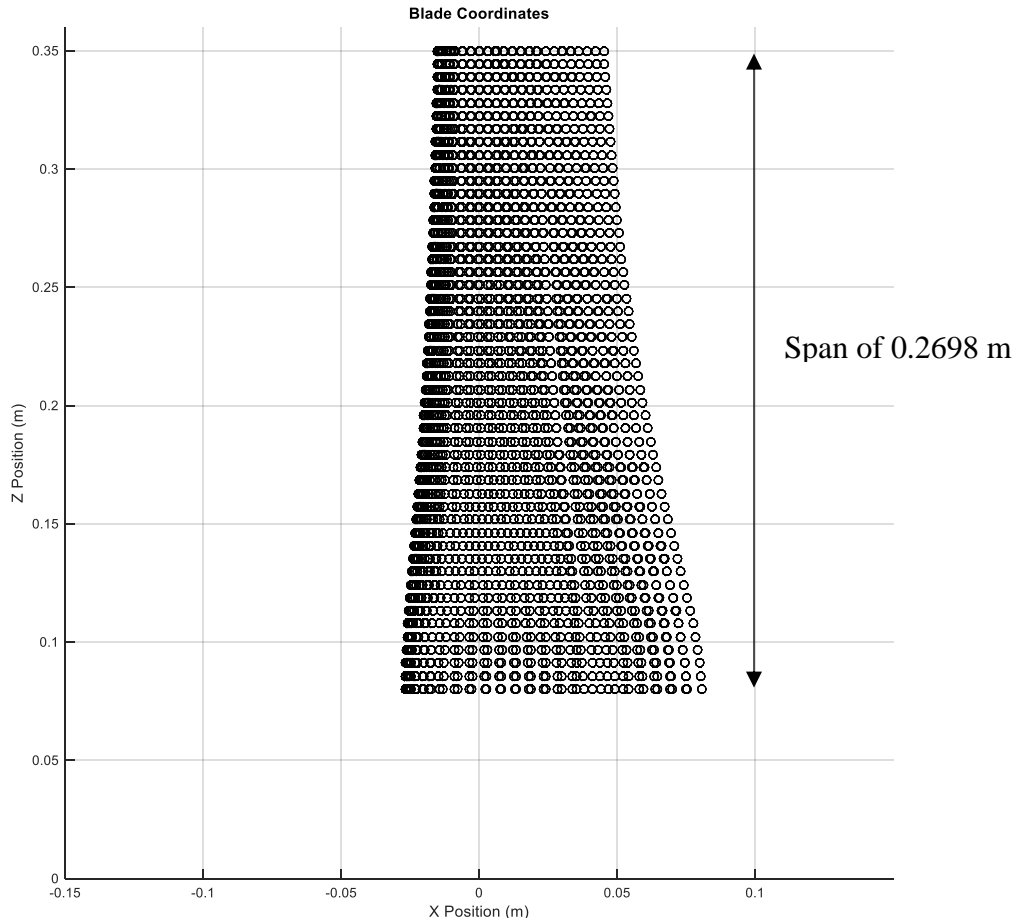


Figure 15: Front view of blade coordinates

Once the transformations are made to the blades, the blade segments are broken up into their upper and lower sections into text files that will be imported into SolidWorks[®] in Section 2.3

2.3 Translation from Text Coordinates to CAD

The overall blade construction was created using SolidWorks[®]. The MATLAB[®] code generates 100 individual text files consisting of the upper and lower blade coordinates for each segment. The loft feature is used to bring all of the blade segments together into one piece. No manipulation of the coordinates is necessary because the code has already transformed the angle based on rotation about the aerodynamic center- which is taken to be 25% of the chord length for each segment (Bazilevs et al., 2011). At the center point, at the base of the blade, the connection

point from the blade to the hub is mounted. The height of the mount is $1e-3$ meters about the hub. The height is chosen such that it eliminates a pinch point that rendered the blade very difficult to mesh. The subtraction of the mount height from blade has almost no effect on torque or power production relative to BEMT calculations. As with all the blade geometry, the hub was designed to closely relate to the geometry of the research group in Japan- resulting in a dome at the front of the hub. The full blade is shown in Figures 16 and 17.

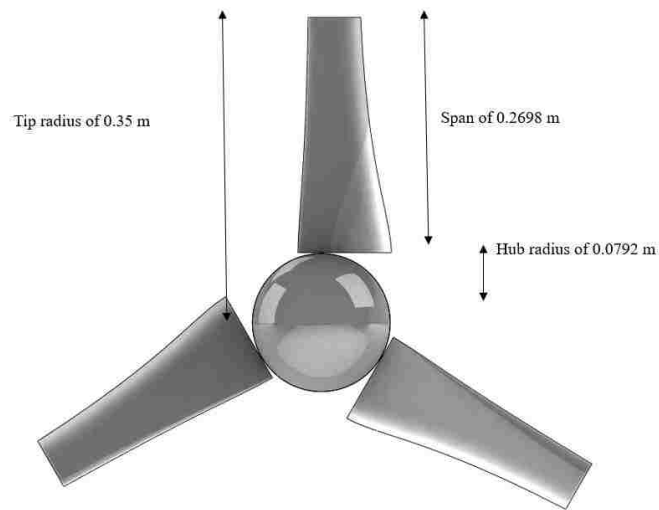


Figure 16: Front view wind turbine blade geometry

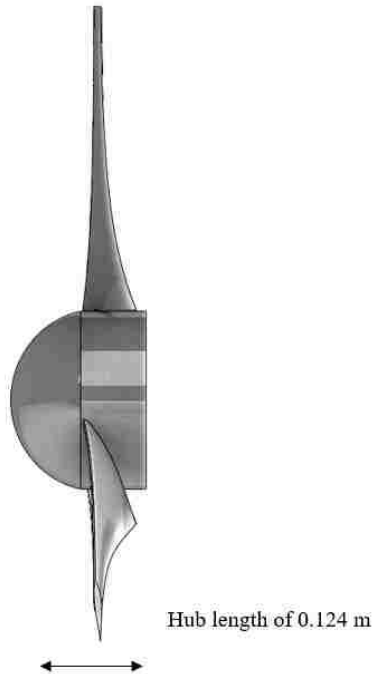


Figure 17: Side view wind turbine blade geometry

The turbine blade has a tip diameter of 0.7 m, a hub diameter of 0.154 m. The span of the blade is based on the tip radius of 0.35 m subtracted from the hub with an additional 0.001 space in between the two for a cylindrical blade support. There was a dome added to the front to direct flow to the blades. The point that anchors the hub to the blade itself is the aerodynamic center of a quarter chord length that defines the axis of rotation of the blade.

Numerical Model

3.1 Numerical Model Settings

Given the limited test data, three speeds will be chosen to show how well the numerical simulation models the experimental system of Ohya et al. (2008). The selected three speeds are 4, 6, and 8 m/s. There was not significant experimental data generated past approximately 9 m/s and values of 3 m/s and below are too close to zero to produce reasonable results.

The optimal tip-speed-ratio (TSR) specified by Ohya et al. (2008) was 4.2. Based on that value and the wind speed, the rotating speed was determined and is summarized in Table 4 along with the conditions for air at standard sea level.

Table 4: Operating conditions and physical properties

Case	1	2	3
U_{∞} (m/s)	4	6	8
ω_{bare} (rad/s)	48	72	96
μ (kg/m-s)	1.7894e-5	1.7894e-5	1.7894e-5
ρ (kg/m ³)	1.225	1.225	1.225

where intensity is defined as:

$$I = 0.16(\text{Re}_{DH})^{-\frac{1}{8}} \quad (75)$$

and Re_{DH} is defined as:

$$\text{Re}_{DH} = \frac{\rho UD}{\mu} \quad (76)$$

The individual turbulence intensities for velocities of 4, 6, and 8 m/s respectively were all left at 10- which is the ANSYS-Fluent[®] default value, which is consistent with similar cases (Thé & Yu, 2017; ANSYS inc., 2011).

As mentioned previously, the model selected was the $k-\omega$ SST turbulence model in ANSYS-Fluent[®]. The model was chosen because of its resolution of the boundary layer and robustness. The generalities of the solver are pressure-based and steady state.

The scheme that was chosen for the solution method was a coupled scheme. The coupled algorithm generally converges in fewer iterations than the semi-implicit method for pressure linked equations (SIMPLE) algorithm. The SIMPLE algorithm assumes an initial pressure, the momentum equation is solved from the guessed value of pressure, the mass flux is determined and a correction is applied to it to obey continuity, the velocity components are corrected, plugged back into the corrected mass flux equation where the pressure correction is determined, the original guessed pressure is corrected with the pressure correction term multiplied by the under-relaxation factor, the result is a pressure and mass flux that obeys continuity, and is then reiterated until the residuals are satisfied at a specified tolerance (ANSYS Inc., 2011). The coupled algorithm is a pressure-velocity coupling method similar to SIMPLE, but the momentum and continuity equations together by implicit discretization momentum equations' gradient terms along with the face mass flux (ANSYS Inc., 2011).

For spatial discretization of equations, the gradient was set to Green-Gauss node based due to its recommendation for tetrahedral meshes from ANSYS-Fluent[®]. The default discretization for pressure, standard, was used over other options of discretization. The pressure staggering option (PRESTO) was considered and tested, but due to the unstructured nature of the mesh, the attempts would always lead to divergences in continuity. To compare the standard scheme to the second-order scheme, a test with the same mesh was run using the two discretization schemes for pressure producing only a difference of about 0.18% leading to the idea that the accuracy of standard compared to a second-order upwind discretization scheme is very similar.

The discretization of the momentum equations makes use of the QUICK scheme due to its greater than second-order accuracy.

The under-relaxation factors were left as the defaults except for pressure and momentum, which were reduced to 0.3 to ensure a smoother convergence.

3.2 Numerical Model Boundary Conditions

Given the periodic nature of the system only one-third of a full rotation needs to be modeled resulting in the geometry shown in the figure below. The stationary enclosure is shown in Figure 18.

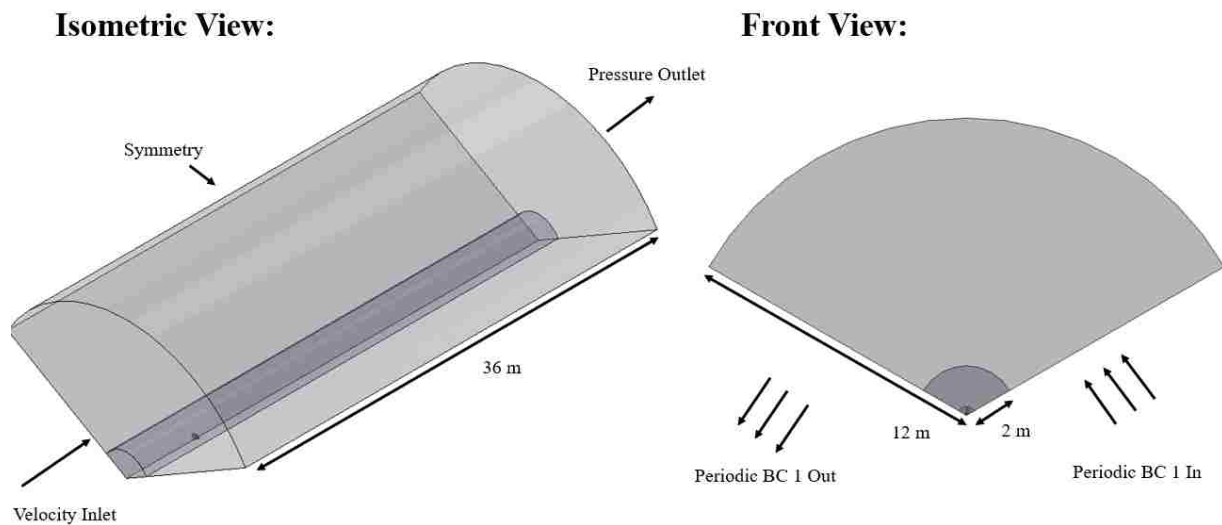


Figure 18: Stationary enclosure

The stationary enclosure has a radius of 12 m, an entrance length of 6 m, an exit length of 30 m- where the distances for the entrance and exit length are relative to the blade center. There is also an inner refinement cylinder that has a radius of 2 m.

The boundary conditions are as follows. The inlet condition is set as a velocity inlet with an inlet speed of one of the three test cases going in the negative z-direction. The turbulent intensity is, as mentioned previously, left at the default value. The outlet condition is set as a pressure outlet with a gauge pressure of zero to combine with the operating pressure of 101325 Pa to

create a general atmospheric condition. The radial equilibrium pressure distribution option is used to accommodate for the pressure distribution that accounts for rotation. The top condition is a symmetry condition to prevent wall effects.

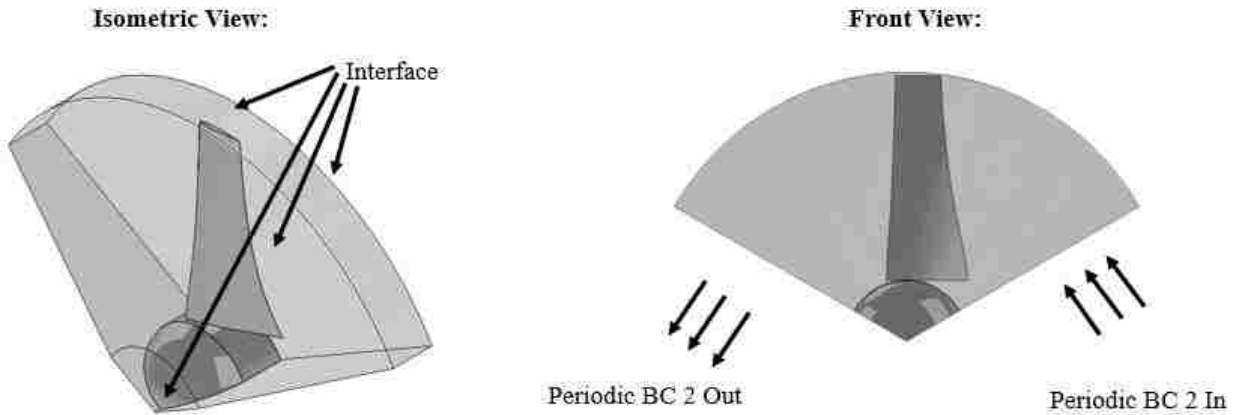


Figure 19: Rotating blade enclosure

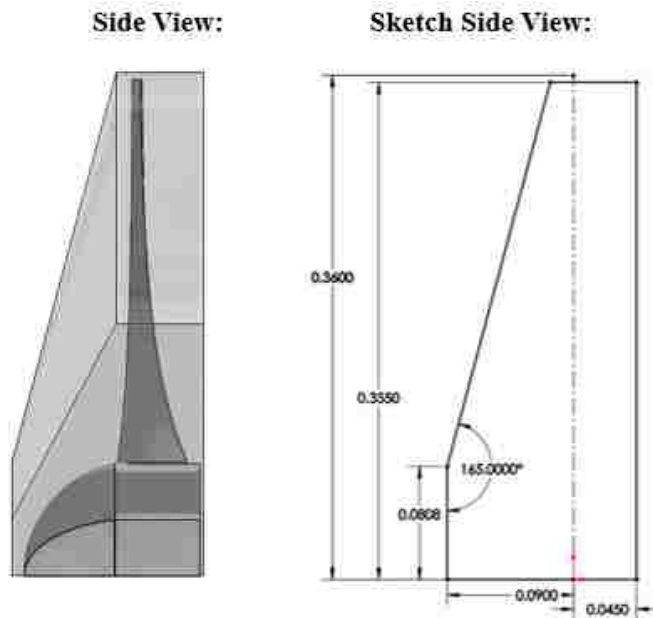


Figure 20: Side view of blade enclosure and sketch view

The rotating blade enclosure shown in Figure 19 consists of one turbine blade that has a radius of 0.35 m. Figure 20 goes into the dimensions of the blade enclosure. The enclosure radius is 0.355 m and was selected so that this current work could have a shroud added to it in future work

easily. The rotating blade enclosure has a maximum thickness at the base of 0.135 m to allow the hub that is 0.124 m to not have any direct interaction with the inlet and outlet interfaces. The reasoning for the non-cylindrical shape is to try and have as little of the flow disturbed by the rotating frame as possible to be more in line with the actual flow path of a wind turbine.

The conditions are set up as an interface in ANSYS-Fluent[®] where the rotating blade enclosure meets the stationary main enclosure. The inner cylinder is a refinement that will be discussed further in Section 3.4. The right and left periodic boundary conditions for the stationary enclosure and rotating enclosure are separate periodic boundary conditions that have matching conditions to compensate for the meshes on either periodic plane not being identical with an offset of 120 degrees. The rotating enclosure is set to frame motion with a rotating speed consistent with the case wind speed. The blade surface inside the rotating enclosure is given a rotate with respect to the reference zone, meaning that it is rotating at the same speed as the rotating enclosure. The interface between the rotating and stationary zones creates non-slip walls with one being rotating and one being stationary. The non-slip wall touching the rotating enclosure is also given a rotation like the blade surface.

3.3 Two-dimensional Airfoil Testing

2D airfoil testing was done to find a reasonable value for the first layer thickness to create a y^+ value of 1 to satisfy the near wall requirements of the $k-\omega$ SST turbulence model. The $k-\omega$ SST turbulence model was chosen to make sure that the transition from two-dimensional testing to three-dimensional testing would not have any major differences due to a model change.

To get a y^+ value of one, generic relations for flow over a flat plate are applied (White, 2003).

$$\text{Re}_x = \frac{U_\infty \rho c}{\mu} \quad (77)$$

where, Re_x specifies the Reynolds number for a particular length- which in this case is the chord length. Next the skin friction coefficient is found.

$$C_f = \frac{0.026}{Re_x^{\frac{1}{7}}} \quad (78)$$

Once the skin friction coefficient is known, the shear stress at the wall can be calculated.

$$\tau_{wall} = \frac{C_f \rho U_{\infty}^2}{2} \quad (79)$$

Once the shear stress at the wall is known the friction velocity is calculated.

$$U_{\tau} = \sqrt{\frac{\tau_{wall}}{\rho}} \quad (80)$$

With the friction velocity known, the first layer thickness can be estimated.

$$\text{First layer thickness} = \frac{y^+ \mu}{U_{\tau} \rho} \quad (81)$$

The physical properties of air are described in Section 3.1. The characteristic length of 0.0603 m to match the section at the tip of the turbine that will see the highest speeds. For a wind speed of 6 m/s, the rotating speed is 72 rad/s producing a tip velocity of 25.2 m/s. The approximate first layer thickness for the tip was found to be 1.16e-5 m. At the base of the blade, the rotating speed would be about 6 m/s. For the maximum chord thickness of 0.118 m at the base, the first layer thickness is calculated as being 4.47e-5 m. Because the first layer thickness is such a small size at the tip, a slight compromise was made to average the first layer thickness for the whole airfoil in initial testing producing a value of 3e-5 m.

Two-dimensional testing was done on an airfoil with the chord length of 0.118 m - the thickest chord length of the blade - at a Reynolds number of 50000 to verify the first layer thickness of 3e-5 m produced reasonable results.

The domain of testing shown in Figure 21 was a C-shape mesh that was 8 m in diameter with a downstream region of 4 m. The airfoil quarter chord is at the center of the enclosure.

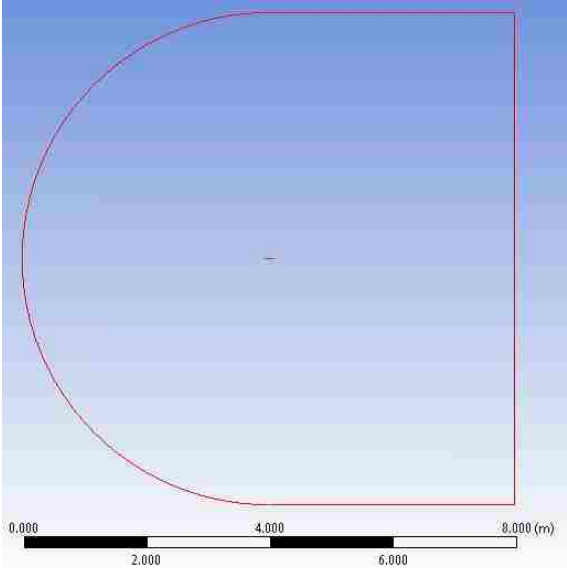


Figure 21: Two-dimensional computational domain

The mesh shown in Figure 22 is an unstructured triangular mesh that has an enclosure refinement sizing of 0.009 m, an edge sizing of $7e-4$ m for the blade, and a first layer thickness of $3e-5$ m. The mesh consisted of 743,542 nodes and 1,480,169 elements.

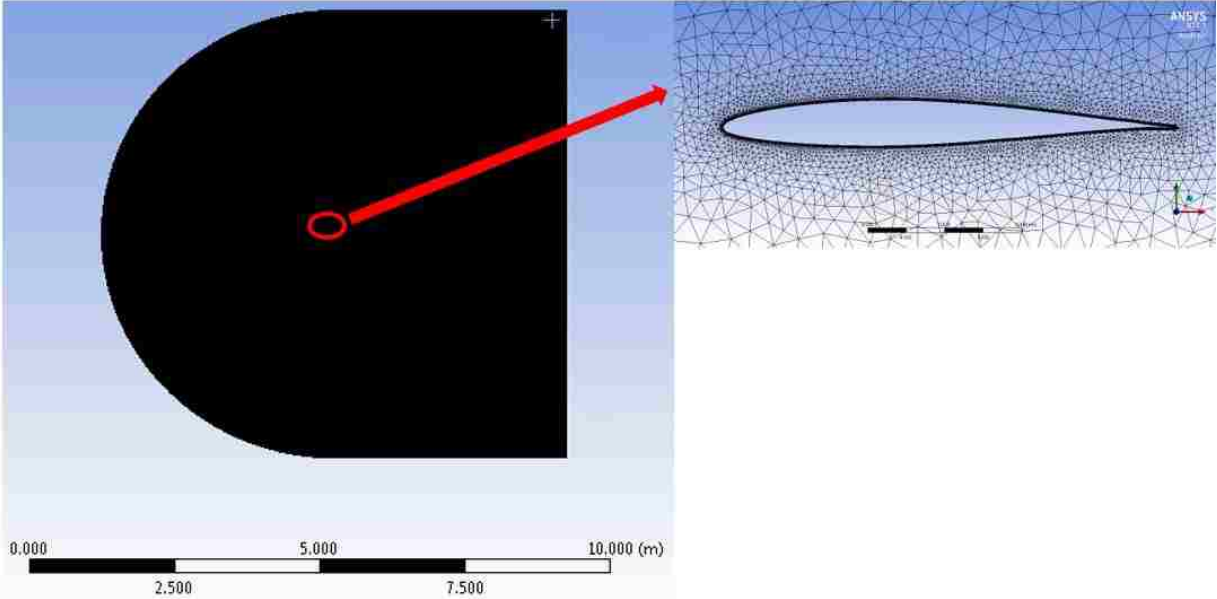


Figure 22: Two-dimensional mesh

The $k-\omega$ shear-stress-transport (SST) turbulence model was chosen for the simulation. The solution method settings solving scheme used was the coupled scheme with spatial discretization of the gradient being least squares cell based and discretization of pressure being standard. The spatial discretization of momentum and all other categories was QUICK. The flow Courant number was set to 5 and the default relaxation factors were used. The Xfoil prediction for the maximum lift coefficient was 5.25 degrees creating a lift coefficient of 0.6853 and a drag coefficient of 0.02044 (“NACA 63-210 AIRFOIL (n63210-il),” 2018). To simulate the flow at a Reynolds number of 50,000 for NACA 63-210 airfoil with a chord length of 0.118 m, the inlet flow was set to 6.208 m/s coming in at an angle of 5.25 degrees creating a flow of 6.18 m/s in the x direction and 0.568 m/s in the y-direction.

The solution was run to a convergence of $1e-6$ producing a lift and drag coefficient of 0.67159 and 0.024316. The percent difference between the Xfoil prediction and the ANSYS-Fluent[®] prediction was 2% for the lift coefficient and 18.96% for the drag. The lift coefficient aligns nicely with the Xfoil value although the drag value is a bit over produced.

The y^+ for the airfoil shown in Figure 23 was well below one for most of the blade with the exception to the leading edge which rose to as high as 1.9. The values are within the specifications of the $k-\omega$ SST turbulence model and can be applied to three-dimensional testing.

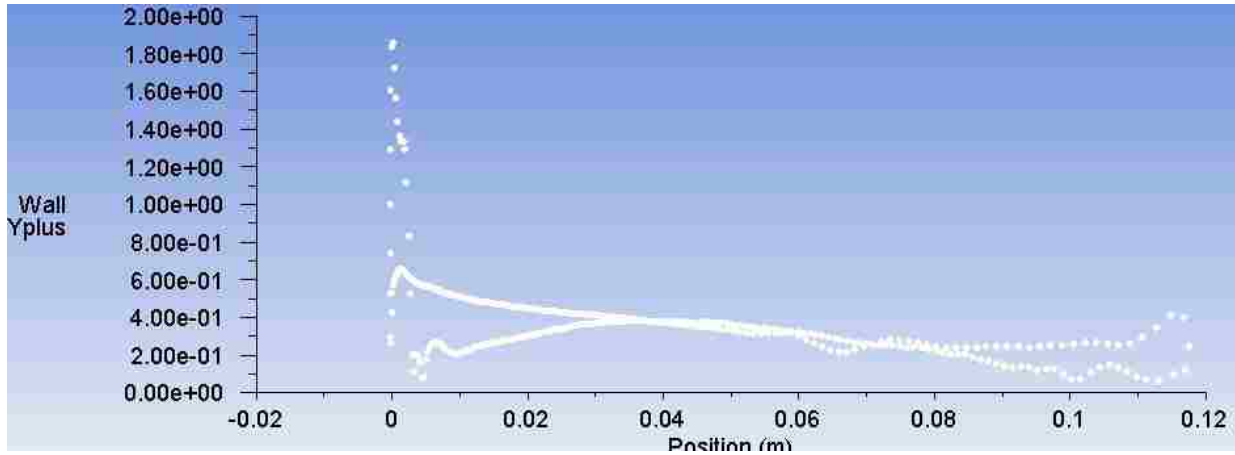


Figure 23: y^+ airfoil

The pressure contour is shown in Figure 24. The suction side encompasses a large portion of the upper airfoil while the high-pressure zone appears to be concentrated towards the nose of the airfoil. It will be seen in the Chapter 4, that this is a consistent trend with some of the changes because of the rotating motion.

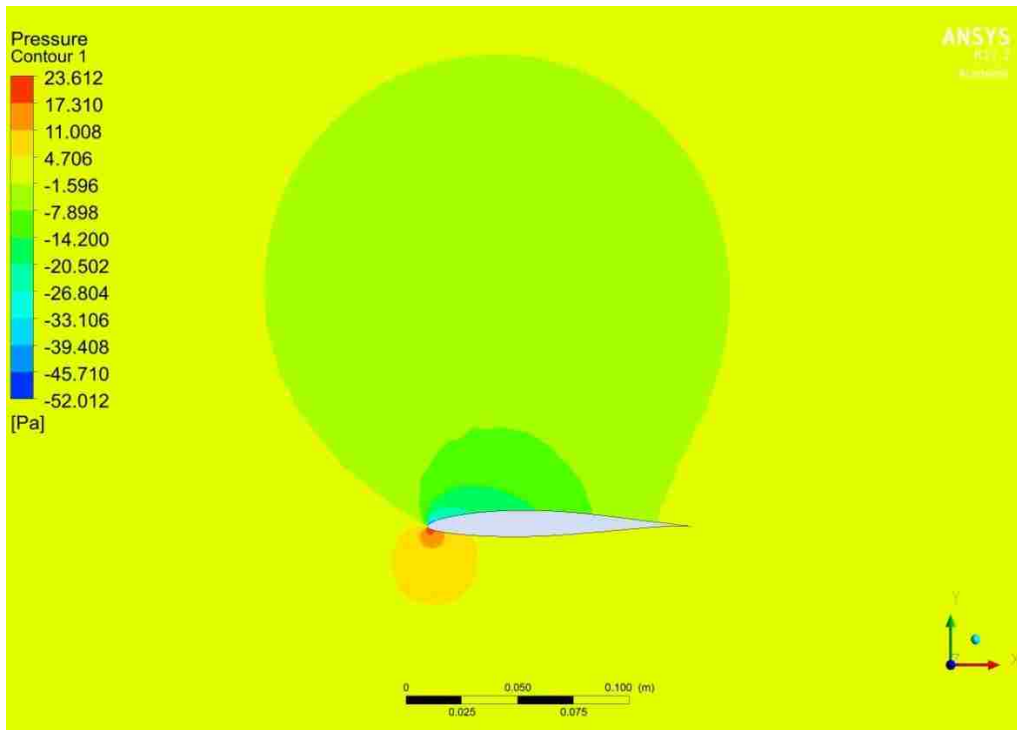


Figure 24: Pressure contour for 63-210 airfoil

3.4 Three-dimensional Mesh Generation

The following is a description of the unstructured mesh set up for the geometry described in Section 3.2. When dealing with interface boundary conditions, it is important that there are similar sizes between both surfaces to avoid any issues. The two interfaces between the rotating blade enclosure and stationary enclosure were both given a hard face element sizing of $3e-3$ m. To mesh the interfaces better, a face meshing condition was applied to the both top faces of the blade enclosure interface to create a more structured and exact interaction. A face meshing condition in ANSYS-Fluent[®] creates a structured mesh on a face. The blade surface is set up with an element size of $3e-3$ m to match the boundaries of the interface. An interior body sizing for the rotating blade enclosure is set at $3e-3$ m for the same reason. There is another face sizing condition that is set for the front and rear faces of the airfoil of the turbine. The sizes tried for the blade refinement were $3e-3$ m, $9e-4$ m, and $7e-4$ m. To improve the quality of the mesh on the blade surface further, a face meshing is applied to the two refined faces of the airfoil of the wind turbine. Next to get the y^+ value of around one that is required when using the $k-\omega$ SST turbulence model, an inflation layer is applied to the entire blade surface. Based on the calculations made for y^+ in Section 3.3, a value of $3e-5$ m was chosen. Another size of $1.5e-5$ m was also tested and is described more in Section 3.5. The maximum number of inflation layers was set to 10 to get full coverage of the entire blade surface. The final condition of the mesh was the refinement cylinder sizing. The refinement cylinder is treated as a body of influence for the stationary enclosure which means that the sizing selected for the refinement cylinder is only applied to the overlapping regions of the refinement cylinder and stationary enclosure. A refinement size was set to three different values, 0.05 m, 0.04 m, and 0.035 m.

There are also some general conditions in the defaults and sizing section of the mesh that were modified. The target skewness was set to be 0.6. Given the unstructured nature of the mesh, reducing skewness is important to avoid numerical diffusion. Given the non-symmetric nature of the NACA 63-210 airfoil and its slight curves near the trailing edge, the max defeature size was set to $1e-5$ m. the max defeature size indicates the max size that the numerical modeler can simplify the geometry. For example, if the max defeature size was set to 1 m, then the numerical modeler could modify all the faces present that have features finer than that threshold. To get the best quality of mesh the smoothing was set to high to try and improve orthogonal quality of the mesh. The span angle center was set to fine to accommodate the small angles of curvature on the airfoil portion of the blade to improve resolution. The curvature normal angle- the maximum angle an element can span on a curved surface- was set to three degrees to further improve resolution on the blade (ANSYS Inc., 2011). An example of the mesh generation is shown in Figures 25 and 26.

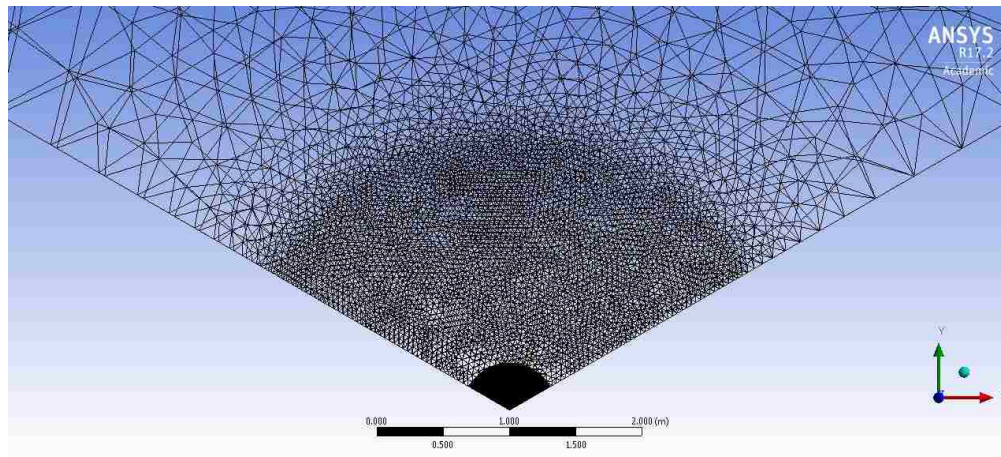


Figure 25: Front view of mesh

In Figure 25, the mesh is finest around the rotating blade zone, with the next finest setting being for the refinement zone, followed by the less fine outer region that it sized as such to eliminate edge effects.

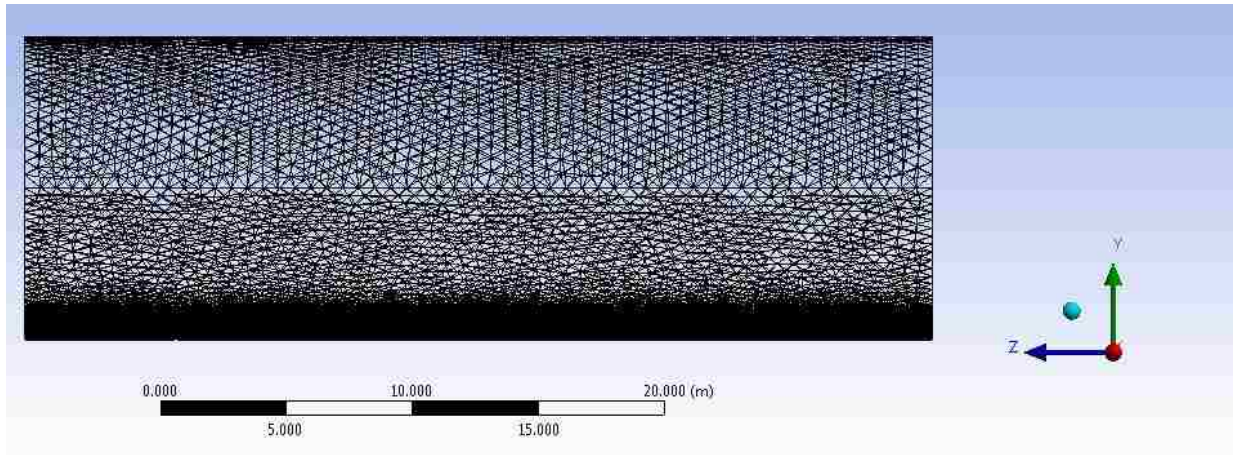


Figure 26: Side view of mesh

Figure 26 shows the side view of the mesh where the refinement zone leads into the less fine outer region. As mentioned, the refinement zone is to better capture the flow and the less fine region is to eliminate edge effects while reducing mesh node count.

3.5 Mesh Independent Study

The mesh study that was mainly done for a wind speed of 6 m/s, however refinement of the blade sizing as well as the inflation layer was done for all three wind speeds. For a wind speed of 6 m/s, three main factors of the mesh were chosen to investigate: the inflation layer, blade sizing, and refinement cylinder sizing. Six points were chosen to draw values of the velocity in the stationary frame in meters per second and the gauge pressure in Pascals. The torque for each mesh is also compared.

The location of the points is summarized in Figure 27. The point selection tried to incorporate multiple points in front, behind, and above the blade region.

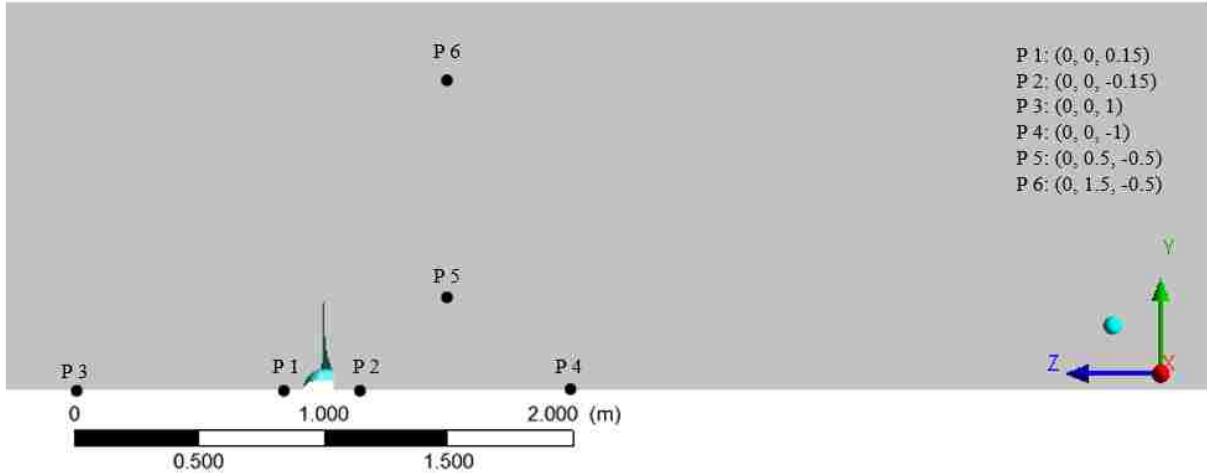


Figure 27: Points for mesh independent study

The mesh conditions that were investigated for a wind speed of 6 m/s are summarized in Table 5.

Table 5: Mesh investigation

Wind Speed (m/s)	Mesh Type	Node Count	Element Count
6	3 e-5 inflation, 0.05 m refinement, 3e-3 blade sizing	2,794,723	15,799,440
6	3 e-5 inflation, 0.05 m refinement, 9e-4 blade sizing	3,508,386	17,881,006
6	3 e-5 inflation, 0.05 m refinement, 7e-4 blade sizing	3,984,249	19,262,468
6	3 e-5 inflation, 0.04 m refinement, 7e-4 blade sizing	5,638,105	29,004,163
6	3 e-5 inflation, 0.035 m refinement, 7e-4 blade sizing	7,295,864	38,776,579
6	1.5 e-5 inflation, 0.04 m refinement, 7e-4 blade sizing	5,690,632	29,317,802

Two sizes were chosen for the first layer thickness of the inflation layer; 3e-5 m and 1.5e-5 m. The blade sizing was held constant for both runs at 7e-4 m as well as the refinement sizing that was set to 0.04 m. For the six points the results from the six points are summarized in Table 6.

Table 6: Point comparison 1.5e-5 m vs. 3e-5 m first layer thickness

Inflation Testing:	1.5e-5 m		3e-5 m		Percent differences	
Point	Velocity in Stationary Frame (m/s)	Gauge Pressure (Pa)	Velocity in Stationary Frame (m/s)	Gauge Pressure (Pa)	Velocity Percent Difference	Pressure Percent Difference
1	4.284	10.861	4.282	10.873	-0.054	0.111
2	2.121	-9.378	2.041	-9.345	-3.781	-0.350
3	5.908	0.721	5.907	0.723	-0.004	0.245
4	2.989	-3.534	2.915	-3.530	-2.485	-0.096
5	6.166	-1.202	6.166	-1.207	0.010	0.394
6	6.021	-0.112	6.021	-0.113	0.001	0.613

There is a slight difference in the values particularly downstream of the blade where the percent difference is 3.78% with the other values not exceeding 2.5%.

Three sizes were chosen for the blade sizing: 3e-5, 9e-4 , and 7e-4 m. As described in Section 3.4, the blade sizing indicates the front and back surface area of the airfoil of the turbine blade. The refinement sizing was held constant at 0.05 m and the first layer thickness was also constant at 3e-5 m. Initially, the blade sizing was reduced from 3e-3 m to 9e-4 m. The comparison results are shown in Table 7.

Table 7: Point comparison to 9e-4 m vs. 3e-3 m blade sizing

Blade Sizing Testing:	9e-4 m		3e-3 m		Percent Differences	
Point	Velocity in Stationary Frame (m/s)	Gauge Pressure (Pa)	Velocity in Stationary Frame (m/s)	Gauge Pressure (Pa)	Velocity Percent Difference	Pressure Percent Difference
1	4.270	10.954	4.268	10.965	0.050	-0.103
2	2.112	-9.300	2.004	-9.743	5.087	-4.766
3	5.907	0.723	5.907	0.726	0.007	-0.406
4	2.825	-3.298	2.568	-3.357	9.101	-1.778
5	6.165	-1.176	6.166	-1.182	-0.022	-0.513
6	6.021	-0.109	6.021	-0.110	0.000	-0.026

There is a noticeably large difference in downstream velocity that is as high as 9.1%. Due to the large difference, to get a better measure of mesh independency, another refinement was made.

The next blade size considered was 7e-4 m. Table 8 shows the point comparison results.

Table 8: Point comparison to 7e-4 m vs. 9e-4 m blade sizing

Blade Sizing Testing:	7e-4 m		9e-4 m		Percent Difference	
	Velocity in Stationary Frame (m/s)	Gauge Pressure (Pa)	Velocity in Stationary Frame (m/s)	Gauge Pressure (Pa)	Velocity Percent Difference	Pressure Percent Difference
1	4.270	10.956	4.270	10.954	-0.007	0.017
2	2.137	-9.318	2.112	-9.300	1.197	0.196
3	5.907	0.7243	5.907	0.723	-0.002	0.147
4	2.857	-3.266	2.825	-3.298	1.104	-0.981
5	6.166	-1.181	6.165	-1.176	0.011	0.451
6	6.021	-0.110	6.021	-0.109	0.001	0.251

The blade sizing refinement from 9e-4 m to 7e-4 m showed results that were much closer to each other with the highest percent difference in the point comparison being about 1.2%.

Three sizes were chosen for the element size of the refinement cylinder: 0.05, 0.04, and 0.035 m. For this series of tests, the blade sizing was held constant at 7e-4 m and the first layer thickness of the inflation layer was held at 3e-5 m. Initially, the refinement size was reduced from 0.05 m to 0.04 m, a 25% decrease in element size. The point values are summarized in Table 9.

Table 9: Point comparison 0.04 m vs. 0.05 m refinement sizing

Refinement Testing:	0.04 m		0.05m		Percent Difference	
Point	Velocity in Stationary Frame (m/s)	Gauge Pressure (Pa)	Velocity in Stationary Frame (m/s)	Gauge Pressure (Pa)	Velocity Percent Difference	Pressure Percent Difference
1	4.282	10.873	4.270	10.956	0.276	-0.760
2	2.041	-9.345	2.137	-9.318	-4.699	0.291
3	5.907	0.723	5.907	0.724	0.003	-0.111
4	2.915	-3.530	2.857	-3.266	1.996	7.472
5	6.166	-1.207	6.166	-1.181	0.008	2.091
6	6.021	-0.113	6.021	-0.110	0.005	2.637

There is a noticeable difference in the region behind the turbine blade with the percent difference being as high as 7.47%.

Since the differences behind the wind turbine were considerably different, another sizing choice was considered, 0.035 m, which is a decrease of about 14.3% from the previous size of 0.04 m. The results of the comparison are shown in Table 10.

Table 10: Point comparison 0.035 m vs. 0.04 m refinement sizing

Refinement Testing:	0.035 m		0.04 m		Percent Difference	
Point	Velocity in Stationary Frame (m/s)	Gauge Pressure (Pa)	Velocity in Stationary Frame (m/s)	Gauge Pressure (Pa)	Velocity Percent Difference	Pressure Percent Difference
1	4.289	10.879	4.282	10.873	0.161	0.052
2	2.050	-9.223	2.041	-9.345	0.451	-1.327
3	5.907	0.726	5.907	0.723	-0.007	0.354
4	2.833	-3.858	2.915	-3.530	-2.886	8.488
5	6.167	-1.215	6.166	-1.207	0.019	0.671
6	6.021	-0.113	6.021	-0.113	0.001	0.303

Excluding point 4, the other point values show consistency with the highest error being - 1.32% for those points. The error for point 4 however, shows a large difference in pressure of 8.49%.

Overall the mesh is considered dependent on refinement sizing in the wake region. The reason for this dependence is because the way the refinement sizing is set up. The entire wake region behind the turbine is changed and refined further to be able to catch more rotating effects in the flow.

The torque on the other hand is considered independent. The results of the mesh study show consistent values for torque across an increased node count for all three wind speeds of interest as described in Table 11.

Table 11: Torque percent difference per mesh tested

Wind Speed (m/s)	Mesh Type	Node Count	Element Count	Torque (N-m)	Actual Torque (N-m)	Torque % Difference
6	3 e-5 inflation, 0.05 m refinement, 3e-3 blade sizing	27,94,723	15,799,440	0.231	0.248	6.666
6	3 e-5 inflation, 0.05 m refinement, 9e-4 blade sizing	3,508,386	17,881,006	0.249	0.248	0.525
6	3 e-5 inflation, 0.05 m refinement, 7e-4 blade sizing	3,984,249	19,262,468	0.255	0.248	2.949
6	3 e-5 inflation, 0.04 m refinement, 7e-4 blade sizing	5,638,105	29,004,163	0.254	0.248	2.787
6	3 e-5 inflation, 0.035 m refinement, 7e-4 blade sizing	7,295,864	38,776,579	0.254	0.248	2.707
6	1.5 e-5 inflation, 0.04 m refinement, 7e-4 blade sizing	5,690,632	29,317,802	0.256	0.248	3.393

Aside from the 3e-3 blade sizing test, the rest of the values for torque are within 3.4% of the actual values. As witnessed by the torque percent difference and what will be seen in the contour

plots in the next section, the $3e-3$ m blade sizing was not fine enough to accurately represent the blade geometry.

It should be noted that the meshes for the 4 m/s and 8 m/s wind speeds are the same meshes from the 6 m/s testing for the two finer cases in the blade sizing testing and the $1.5e-5$ m first layer thickness mesh. The values are summarized in Figure 28.

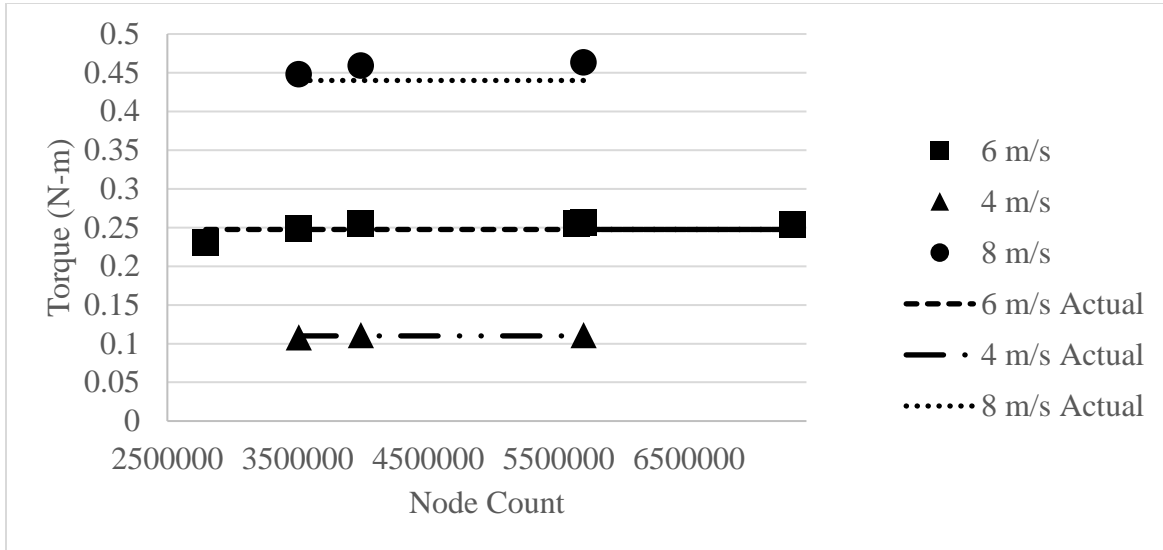


Figure 28: Torque vs. node count

The 6 m/s testing torques were referenced in Table 11. The $3e-3$ m blade sizing was omitted from testing for the 4 and 8 m/s tests due to its inability to accurately represent the blade. As shown in Figure 28, even when the speed is dropped or increased, the numerical model gives an accurate representation of torque.

Results and Discussions

4.1 Initial 6 m/s mesh testing

The geometry of the systems described in this section and for all sections in Chapter 4 is the same as shown in Section 3.2. The first testing was done for a wind speed of 6 m/s.

The initial sizing that was chosen had a first layer thickness of $3e-5$ m, a blade sizing of $3e-3$ m and a refinement sizing of 0.05 m. The mesh consisted of 15,799,440 elements and 2,794,723 nodes. The torque produced was 0.231 N-m creating 16.6 W of power. The actual torque and power should be 0.2475 N-m and 17.82 W- which the current simulation is 6.67% different.

The blade sizing was refined of 0.003 m to $9e-4$ m. The new mesh consists of 3,508,386 nodes and 17,881,006 elements, an increase by about 26% for nodes and 13% for elements. The new mesh produced a torque of 0.249 N-m producing 17.92 W of power. The values are fairly consistent with the actual torque and power of 0.2475 N-m and 17.82 W with a percent difference of 0.6%.

Next the mesh was refined even further. The same peripheral mesh sizing choices were not changed, however the blade sizing was refined further to $7e-4$ m. The new mesh consisted of 3,984,249 nodes and 19,262,468 elements- which is an increase of about 14% for the number of nodes and about 8% for the number of elements. The torque produced is 0.2548 N-m generating 18.35 W of power- which is 2.95% different from the actual torque and power of 0.2475 N-m and 17.82 W.

To gain an understanding of the flow and to check for any inconsistencies, for initial testing, the $y+$ contour is checked to ensure that it is around 1 with a maximum value of 5, the velocity and pressure contours are checked for a section 0.2 m above the x-z plane, and the velocity and pressure contour plots are checked in the y-z plane. Only the blade sizing variation tests are

shown, with the same refinement sizing of 0.05 m and first layer thickness of 3e-5 m for each of the mesh tests in this section.

As shown in Figure 29, the y^+ value was adjusted with the change of resolution in the blade from 2.179 to 3.047, which is a percent difference of 28.5%. The large difference furthers the claim that the previous mesh sizing on the blade surface was not adequate to accurately represent the blade.

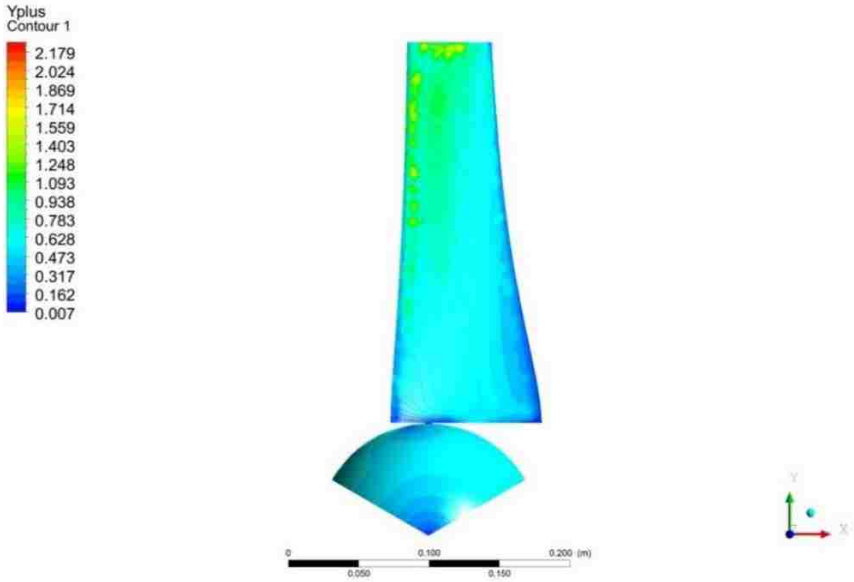


Figure 29: y^+ blade surface (3e-3 m)

The y^+ values on the blade surface shown in Figure 30 are consistent with the requirements of the $k-\omega$ SST turbulence model used with the maximum value being around 2.179- which is still less than five. Although not pictured, the maximum value occurs on the backside of the blade toward the tip.

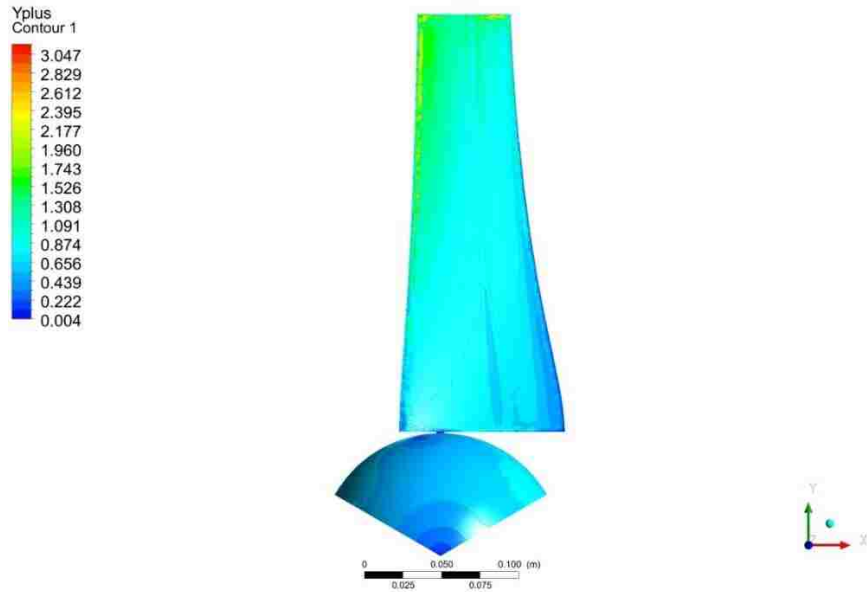


Figure 30: y^+ blade surface ($9e-4$ m)

The y^+ values shown in Figure 31 are very consistent between the $9e-4$ and $7e-4$ with minute differences with the maximum value being only 1.17% different from Figure 23. It should be noted that the points of maximum y^+ are more visible toward the blade tip with the improved resolution of the blade.

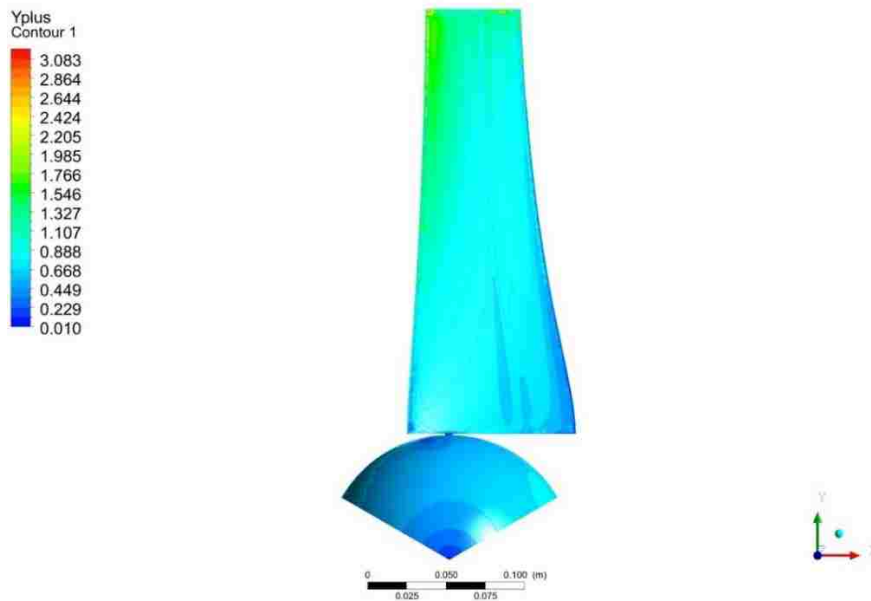


Figure 31: y^+ blade surface ($7e-4$ m)

The velocity in that stationary frame for the 3e-3 m blade size is shown in Figure 32. The velocity is consistent with a higher velocity in front of the blade and a lower velocity after it.

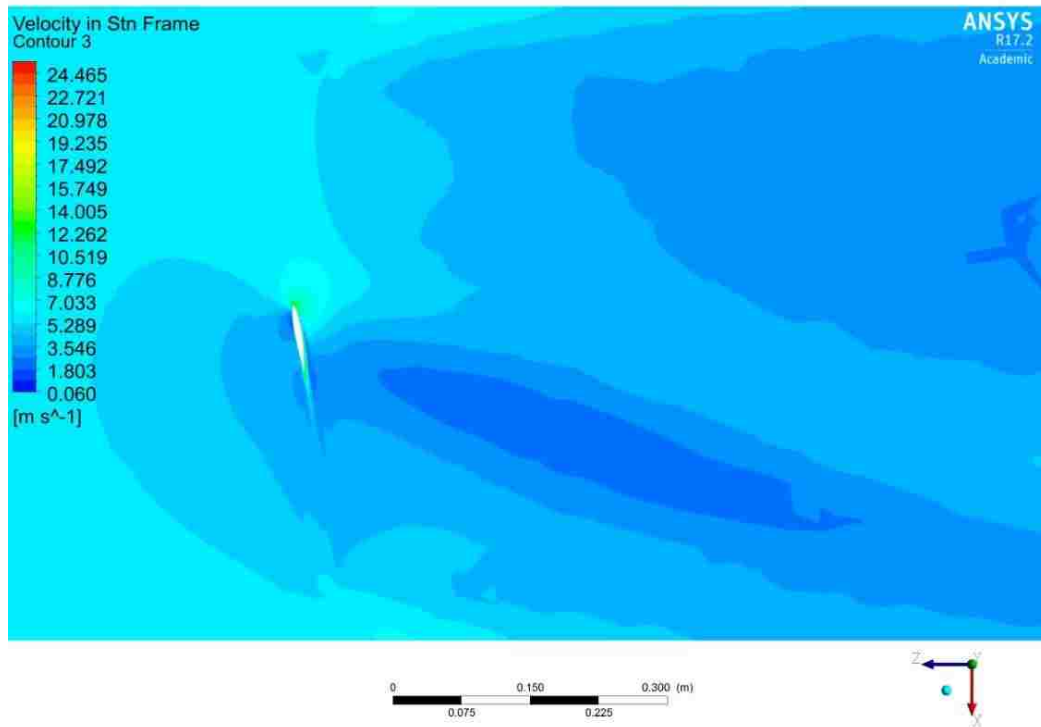


Figure 32: Velocity in stationary frame contour for 0.2 m slice in y-direction (3e-3 m)

The velocity in the stationary frame for the 9e-4 m blade sizing shown in Figure 33 shows the same major flow characteristics as previously shown leading to the idea that the blade resolution is less impactful on the flow. There is a noticeable change to the largest velocity magnitude being about 3 m/s larger. The higher velocity corresponds to the higher y^+ values being seen in Figure 30.

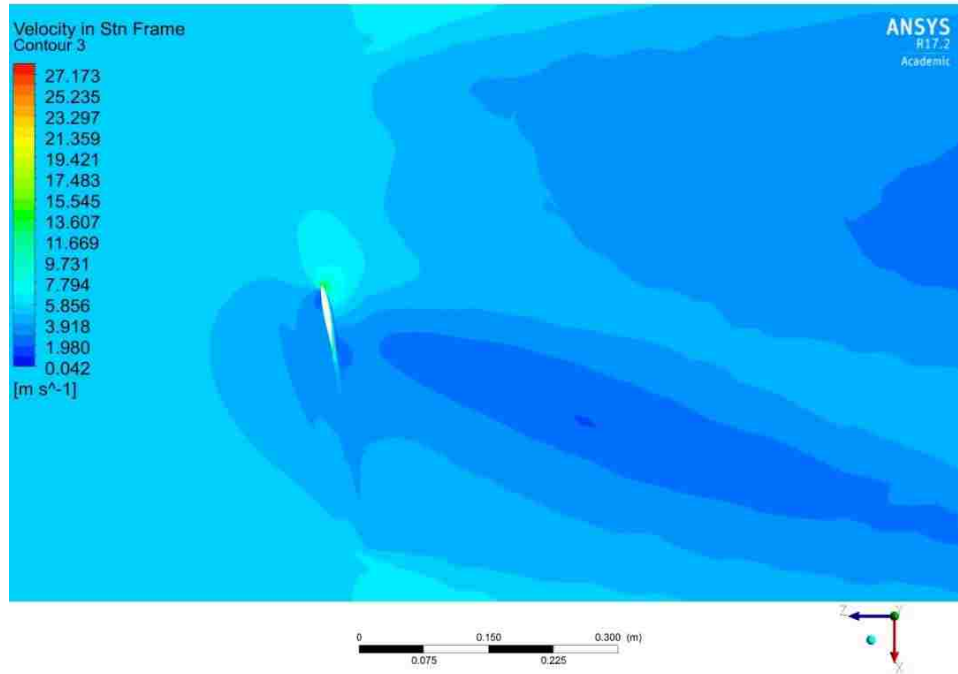


Figure 33: Velocity in stationary frame contour for 0.2 m slice in y-direction ($9e-4$ m)

The velocity in the stationary frame for the $7e-4$ m blade sizing shown in Figure 34 is also consistent with the previous blade sizing with only a slight different in maximum velocity.

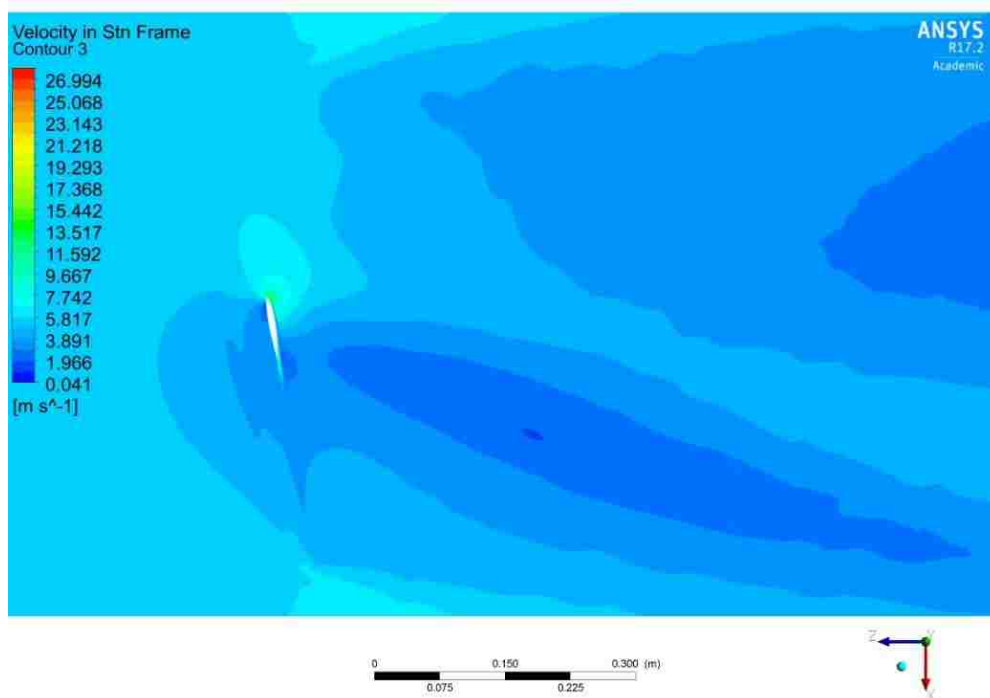


Figure 34: Velocity in stationary frame contour for 0.2 m slice in y-direction ($7e-4$ m)

The pressure contour shown in Figure 35 shows inconsistencies at the leading edge where the high pressure contour appears to have a chunk of the higher pressure region missing from it. As mentioned in the mesh independent study, it is believed that the 0.003 m sizing of the blade is not fine enough to adequately capture the leading edge of the turbine blade.

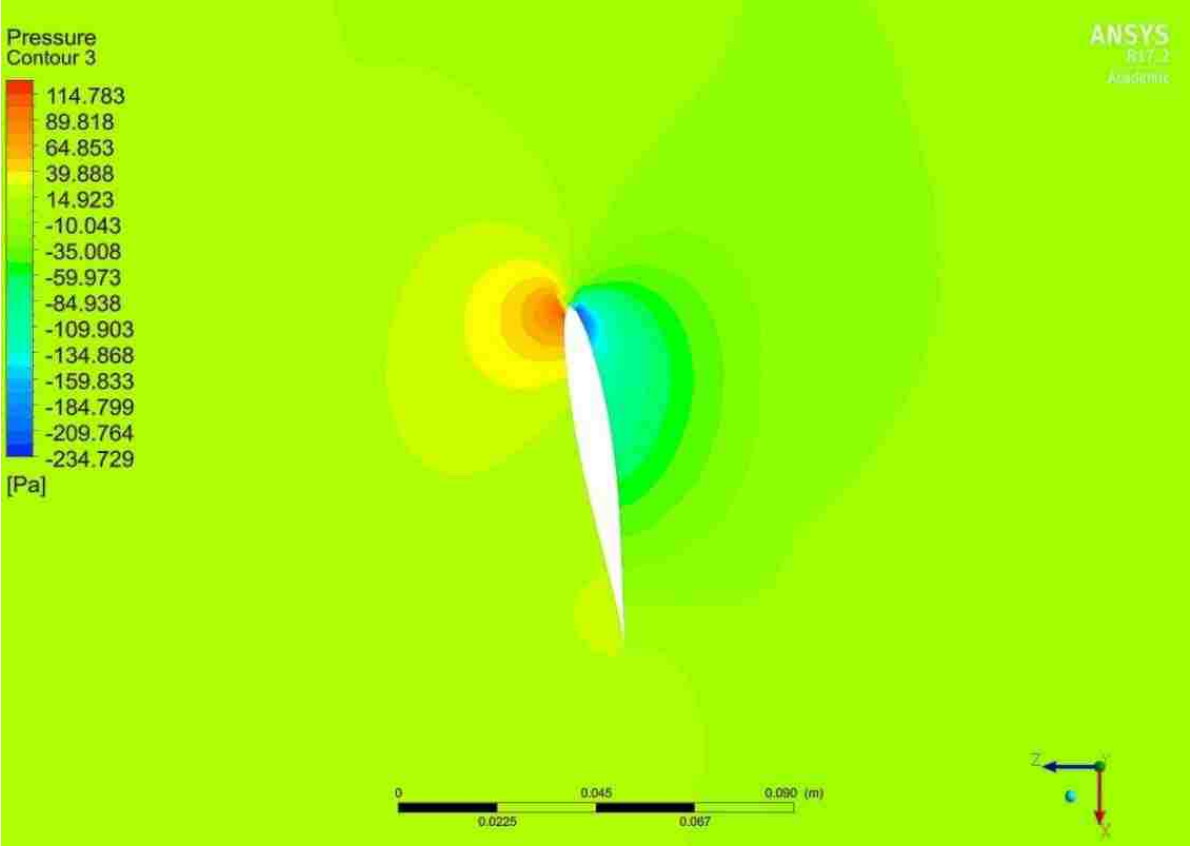


Figure 35: Pressure contour for 0.2 m slice in y-direction (3e-3 m)

The pressure contour for the 9e-4 m blade sizing shown in Figure 36 shows better resolution from the previous blade sizing especially at the leading edge where a noticeable chunk seemed to be missing in the high pressure portion. The bounds are noticeable different with an increase in the highest pressure by about 10 Pascals and a decrease in the lowest pressure by about 35 Pascals.

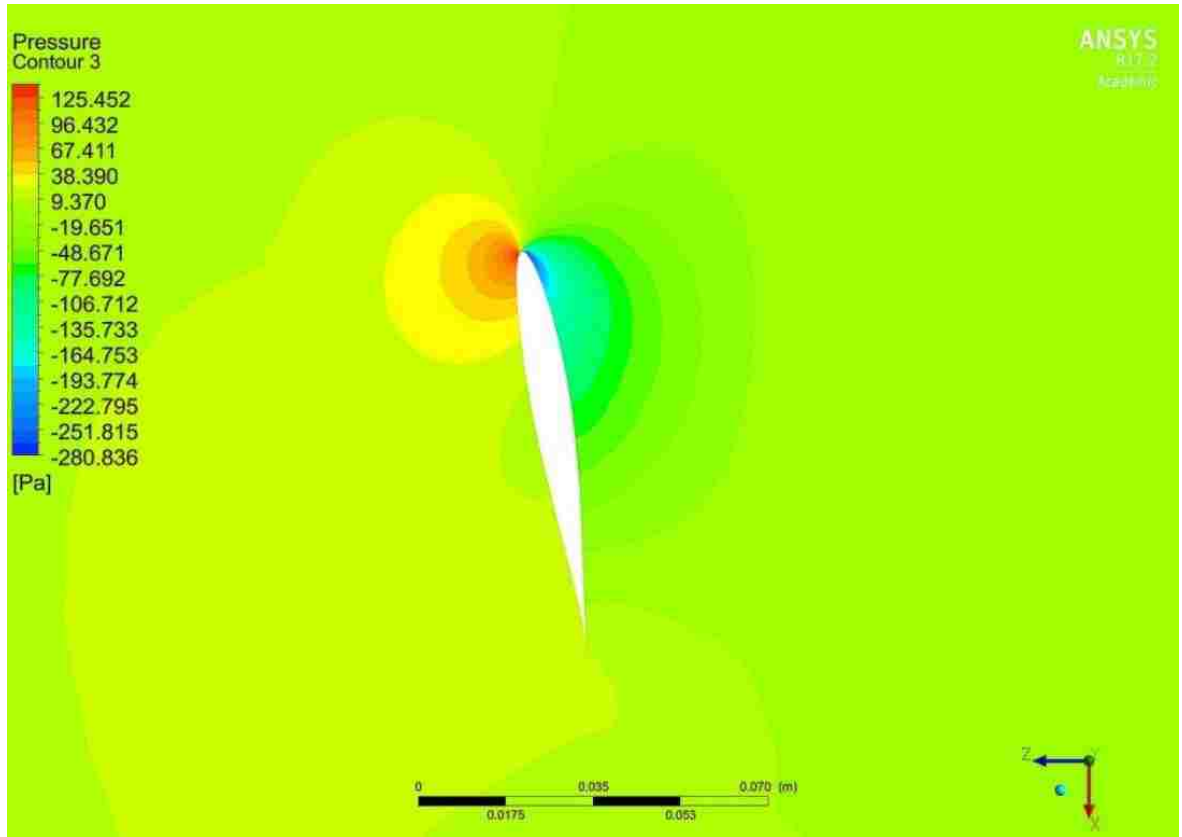


Figure 36: Pressure contour for 0.2 m slice in y-direction ($9e-4$ m)

The pressure contour for the $7e-4$ m blade sizing in Figure 37 shows a similar pattern overall, but the high pressure side of the blade appears to a more defined whereas before in Figure 25, the final exterior contour of it seemed to have a more cubic shape. There is also a difference in the lowest pressure by 13%. The flow looks more consistent with contour plots from another group around the half way point of the airfoil, however the blade is far bigger with a tip radius of 128 m and has a different airfoil (Zhu et al., 2014)

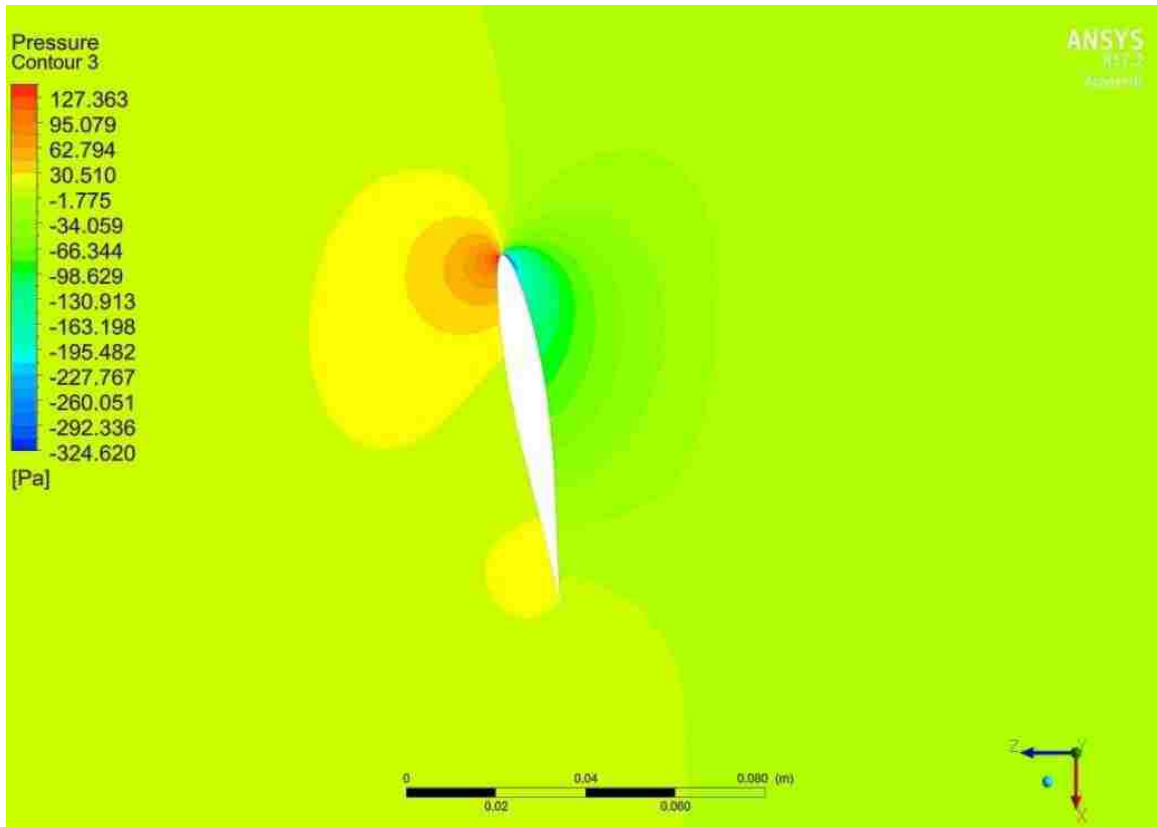


Figure 37: Pressure contour for 0.2 m slice in y-direction ($7e-4$ m)

The velocity in the stationary frame for a $3e-3$ m blade sizing shown in Figure 38 is consistent with a higher velocity before the blade and a lower velocity after with the extraction of power. The flow at the tip mixing with the freestream velocity also seems reasonable as the velocity in that region is still above the freestream velocity.

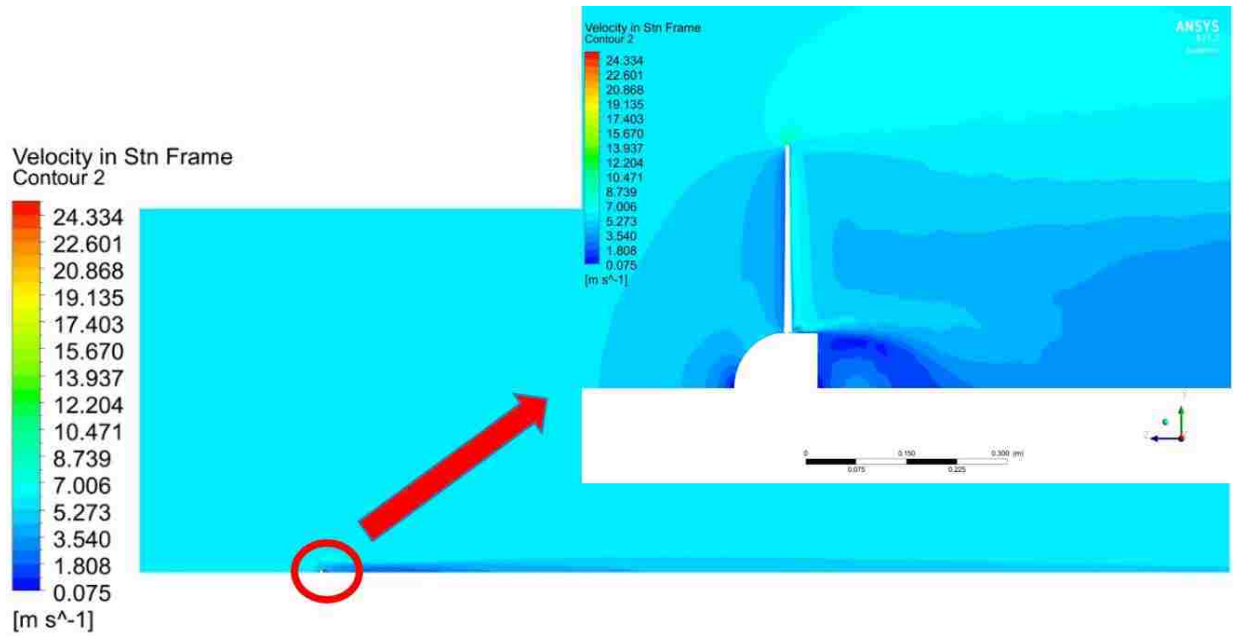


Figure 38: Velocity in stationary frame in y-z plane (3e-3)

The velocity in the stationary frame contour for the 9e-4 m blade sizing shown in Figure 39 compares very well for the different meshes with no real differences in flow path present furthering the idea that the blade sizing is less impactful on the overall flow of the system.

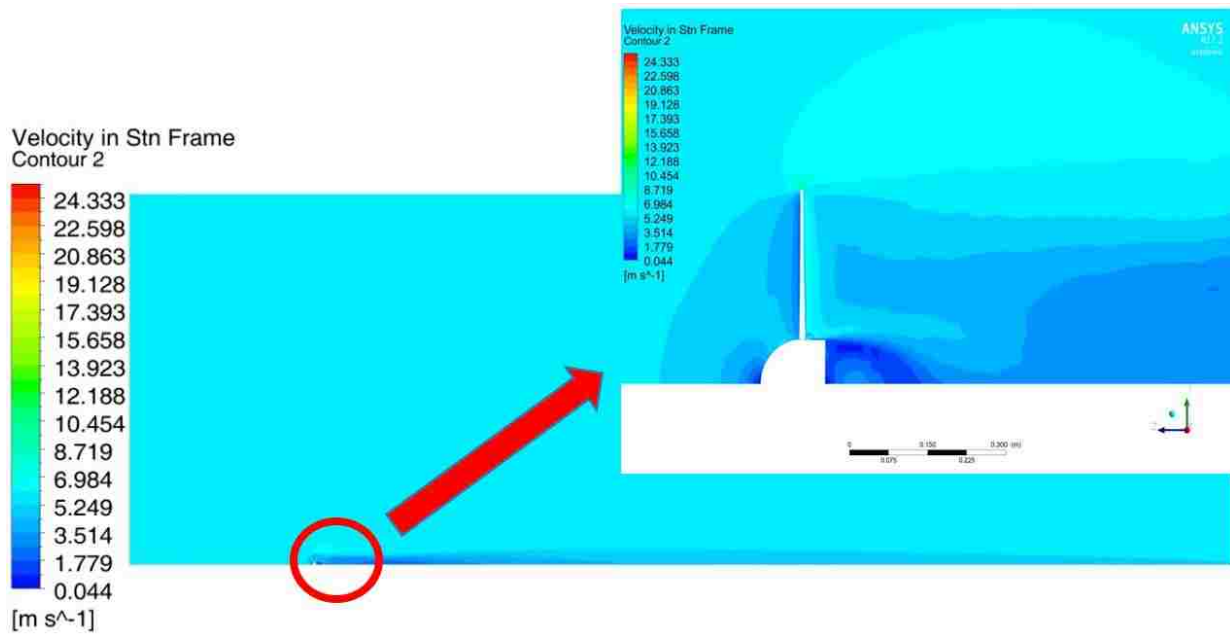


Figure 39: Velocity in stationary frame in y-z plane (9e-4)

The velocity in the stationary frame contour for the 7e-4 m blade sizing shown in Figure 40 is very similar to the previous two tests showing no real major changes to the flow path.

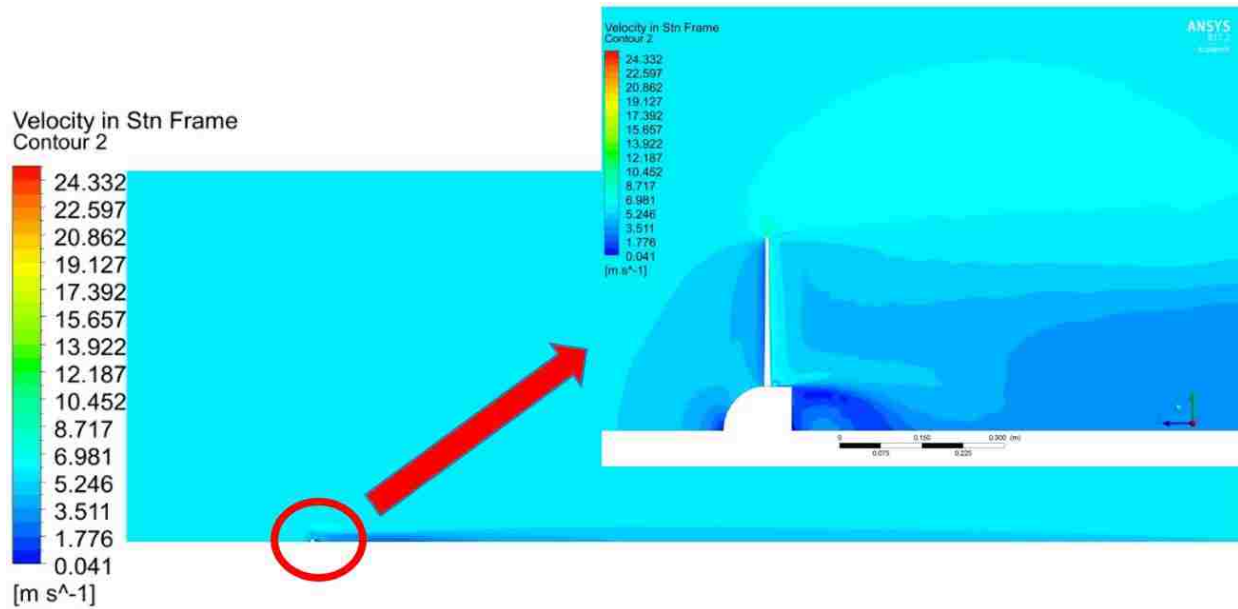


Figure 40: Velocity in stationary frame in y-z plane (7e-4 m)

The pressure contour for the 3e-3 m blade sizing shown in Figure 41 is consistent with the higher pressure being at the bottom of the airfoil and a lower pressure being at the top, driving the turbine in a counter clockwise direction.

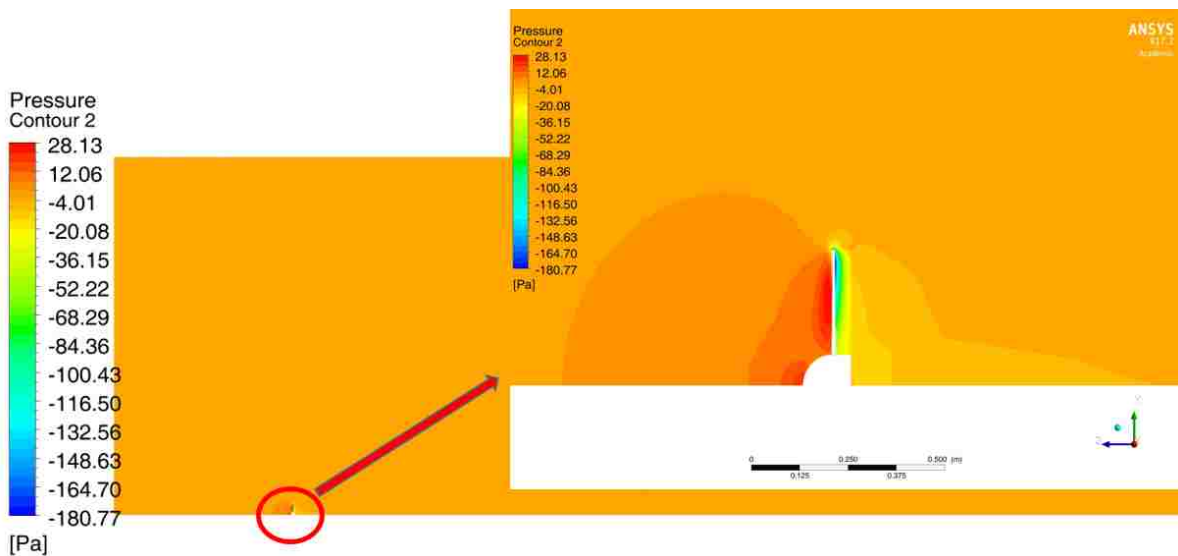


Figure 41: Pressure contour in y-z plane (3e-3 m)

The pressure contour for a blade sizing of $9e-4$ m shown in Figure 42 shows minute changes in pressure compared to Figure 41 and are essentially the same, but when zoomed in, the plot shows a slight low pressure zone behind the blade hub which is most likely due to a circulation caused by flow coming through the gap between the airfoil and hub. It appears that the blade only impacts the pressure along the blade making torque more dependent on blade sizing rather than the general flow path of the system.

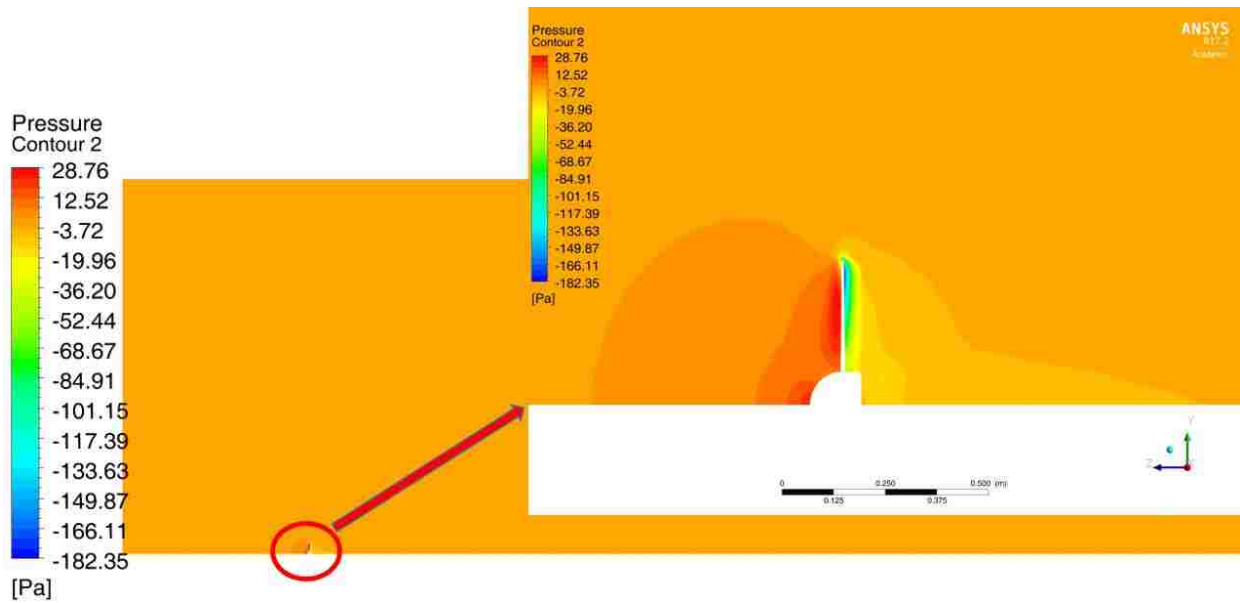


Figure 42: Pressure contour in y-z plane ($9e-4$ m)

The pressure contour for the $7e-4$ m blade sizing shown in Figure 43 is very similar to the previous sizing, but has a slightly larger circulation behind the blade hub. This is most likely due to the contour boundaries varying slightly.

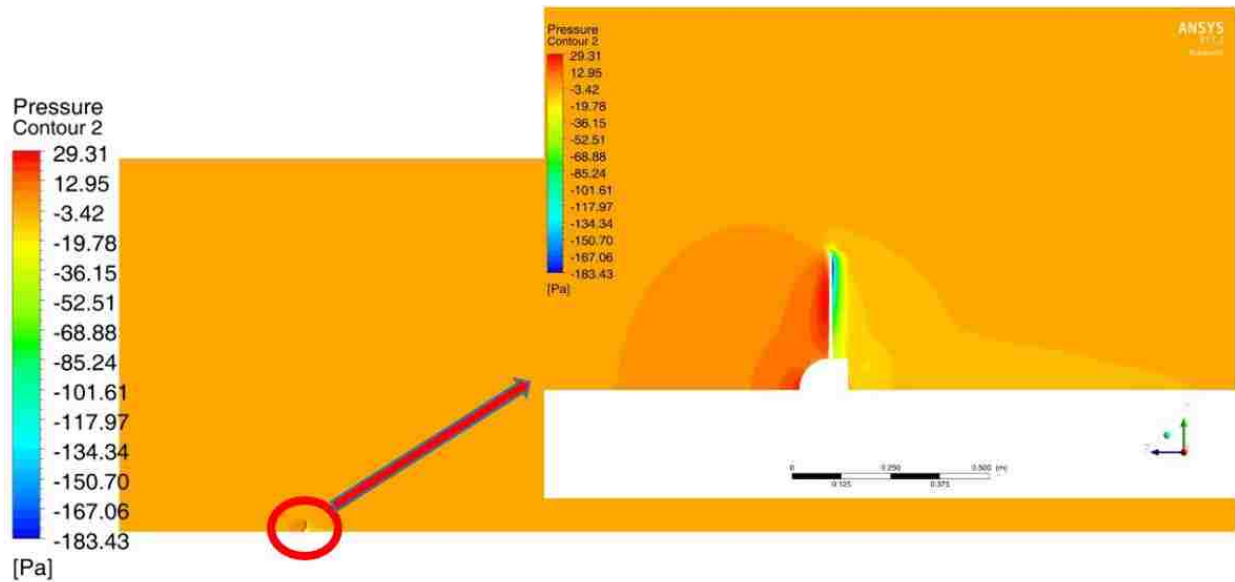


Figure 43: Pressure contour in y-z plane ($7e-4$ m)

Based on the information of the blade sizing tests, it was determined that the flow path is not really impacted by the blade resolution, but the torque is very much impacted because of its effect on the high and low pressure sides of the blade.

Other tests were done as mentioned in the mesh study in Section 3.5. The characteristics in the contour plots were very similar and were not shown for brevity. When the inflation layer was adjusted as described in Section 3.5, a net change of only 0.59% difference between the torques occurred with no major flow characteristics changed. A change in the refinement sizing also yielded no real dramatic changes to the flow contours, however the values behind the turbine would change as described in Section 3.5.

4.2 Initial 4 m/s Mesh Testing

The meshes used in section 4.1 were reused and tested for 4 m/s with the exception of the 3e-3 m blade sizing that clearly showed resolution issues.

For a blade sizing of $9e-4$ m, the torque produced was 0.108 N-m producing 5.19 W. The actual results for torque and power should be 0.11 N-m and 5.28 W respectively- a percent

difference of 1.81 %. As was done for the initial 6 m/s testing, contour plots were generated to describe the flow.

Next the $7e-4$ m blade sizing mesh was used. The torque equaled 0.111 N-m generating 5.31 W of power. The actual torque and power were 0.11 N-m and 5.28 W respectively making a percent difference of 0.91 %.

The y^+ contour plot for the $9e-4$ m blade sizing shown in Figure 44 were a maximum of 2.188 where the maximum is not pictured as it is on the back of the blade toward the tip.

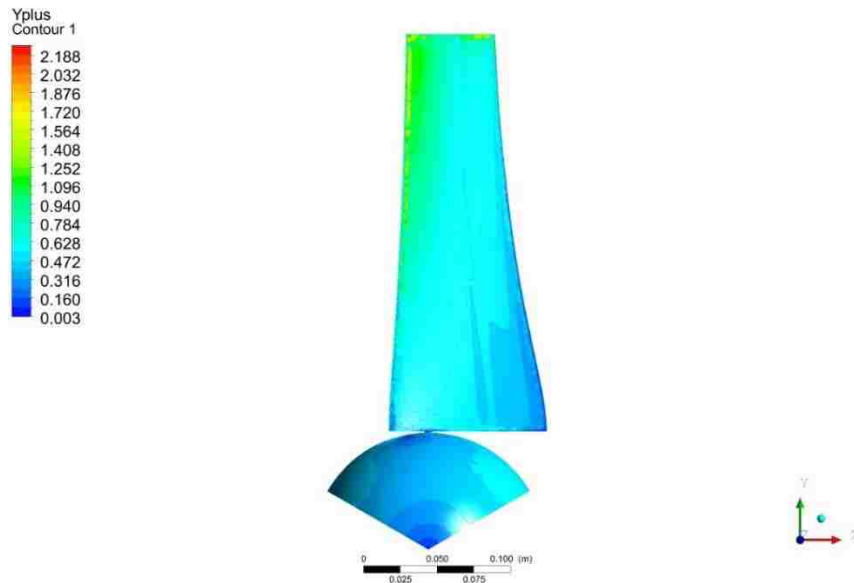


Figure 44: y^+ blade surface ($9e-4$ m)

The y^+ contour plot for the $7e-4$ m blade sizing shown in Figure 45 has a 2.93 percent difference compared to the maximum value in Figure 44. The percent difference between refinements is slightly higher than that of the 6 m/s by about 1.7% more.

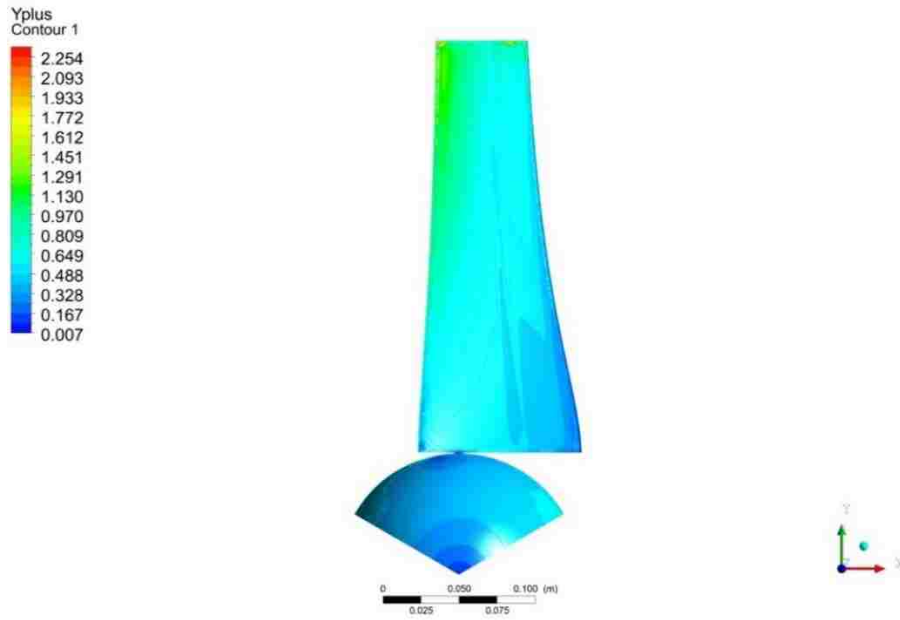


Figure 45: y^+ blade surface ($7e-4$ m)

The velocity in the stationary frame for the $9e-4$ m blade sizing shown in Figure 46 shows a similar flow path as the 6 m/s testing.

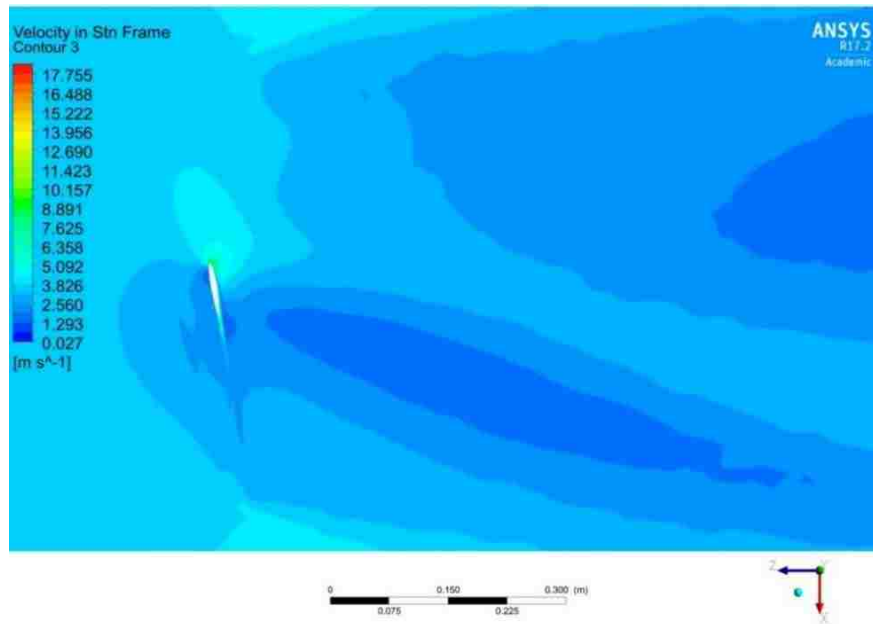


Figure 46: Velocity in stationary frame contour for 0.2 m slice in y-direction ($9e-4$ m)

The velocity in the stationary frame contour for the $7e-4$ m blade sizing shown in Figure 47 shows a similar flow path with a lower peak velocity compared to 6 m/s testing due to the lower inlet velocity.

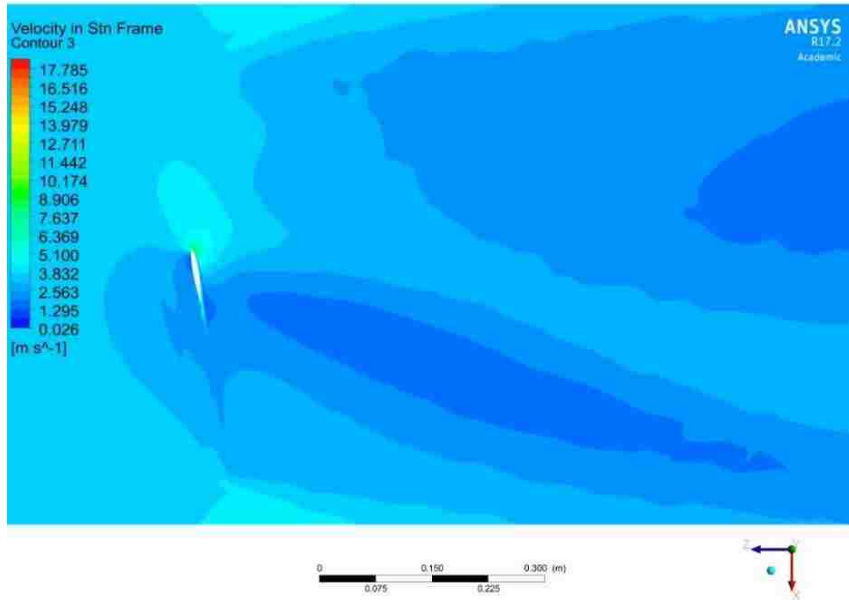


Figure 47: Velocity in stationary frame contour for 0.2 m slice in y-direction ($7e-4$ m)

The pressure contour for the $9e-4$ m blade sizing shown in Figure 48 shows very similar results as previously seen for the 6 m/s testing.

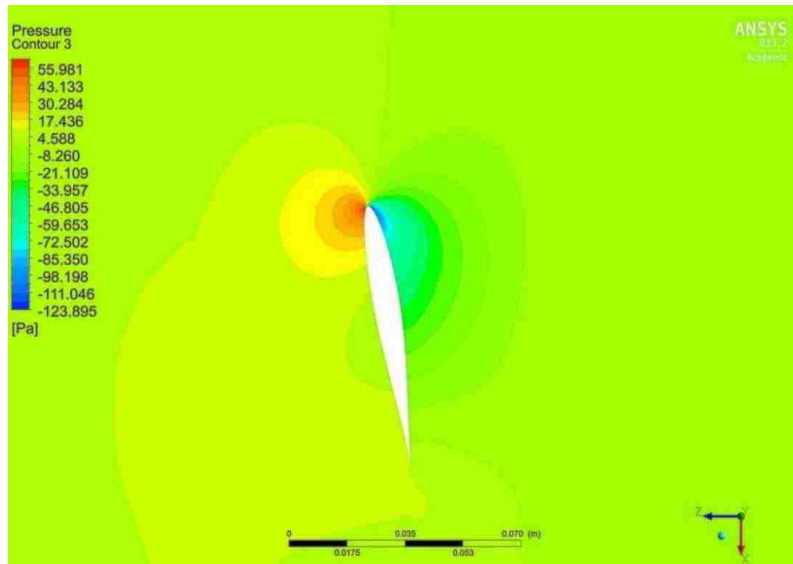


Figure 48: Pressure contour for 0.2 m slice in y-direction ($9e-4$ m)

The pressure contour for the $7e-4$ m blade sizing shown in Figure 47 has changes in the outer portion of the high pressure and suction side of the blade. There is also about a 10% difference between the lowest pressures between Figures 48 and 49. The presence of the pressure change was noted in the 6 m/s testing as well.

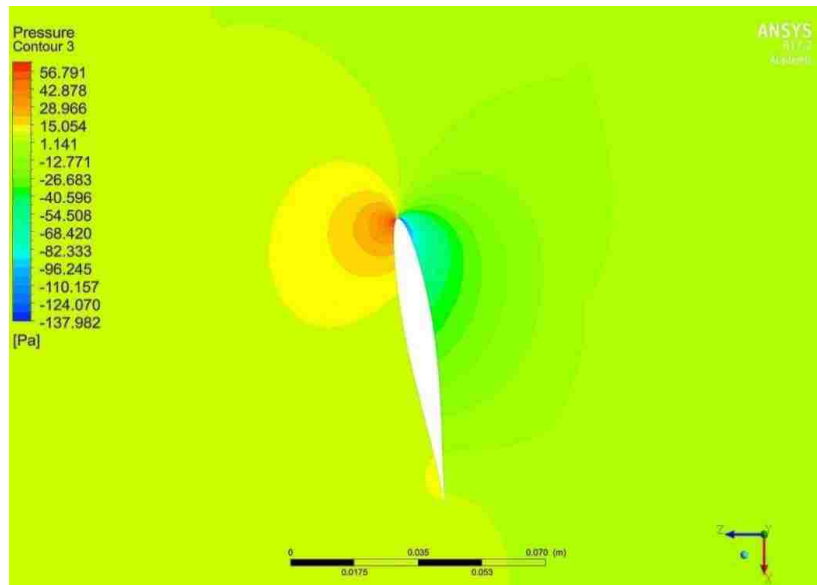


Figure 49: Pressure contour for 0.2 m slice in y-direction ($7e-4$ m)

The velocity in the stationary frame for the $9e-4$ m blade sizing shown in Figure 50 looks similar to the 6 m/s testing with lower peak values due to the decreased incoming wind speed.

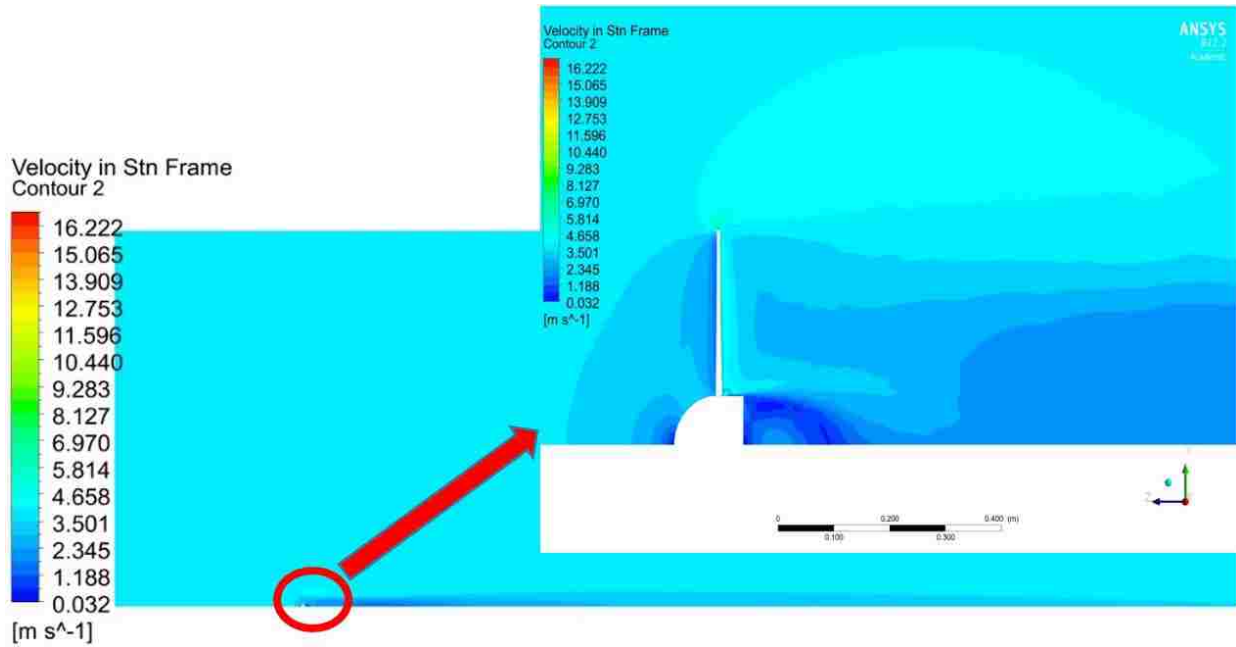


Figure 50: Velocity in stationary frame in y-z plane ($9e-4$ m)

The velocity in the stationary frame for the $7e-4$ m blade sizing shown in Figure 51 is consistent with the previous blade sizing with no real changes in the maximum and minimum velocities present.

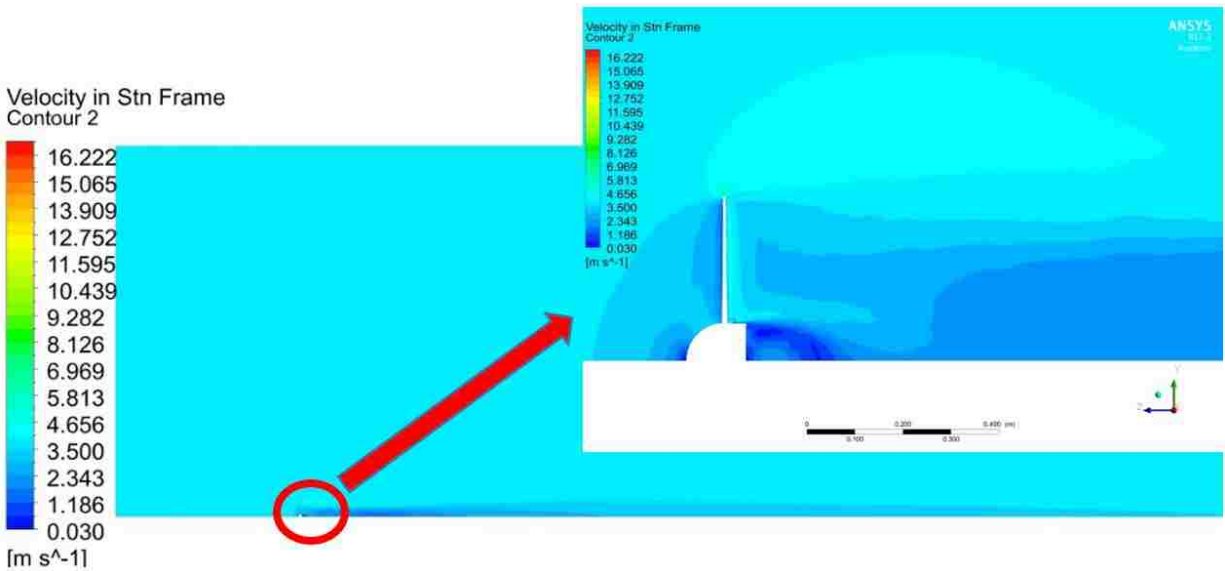


Figure 51: Velocity in stationary frame in y-z plane ($7e-4$ m)

The pressure contour for the $9e-4$ m blade sizing shown in Figure 52 is also similar to the 6 m/s testing with the circulation zone appearing behind the blade hub.

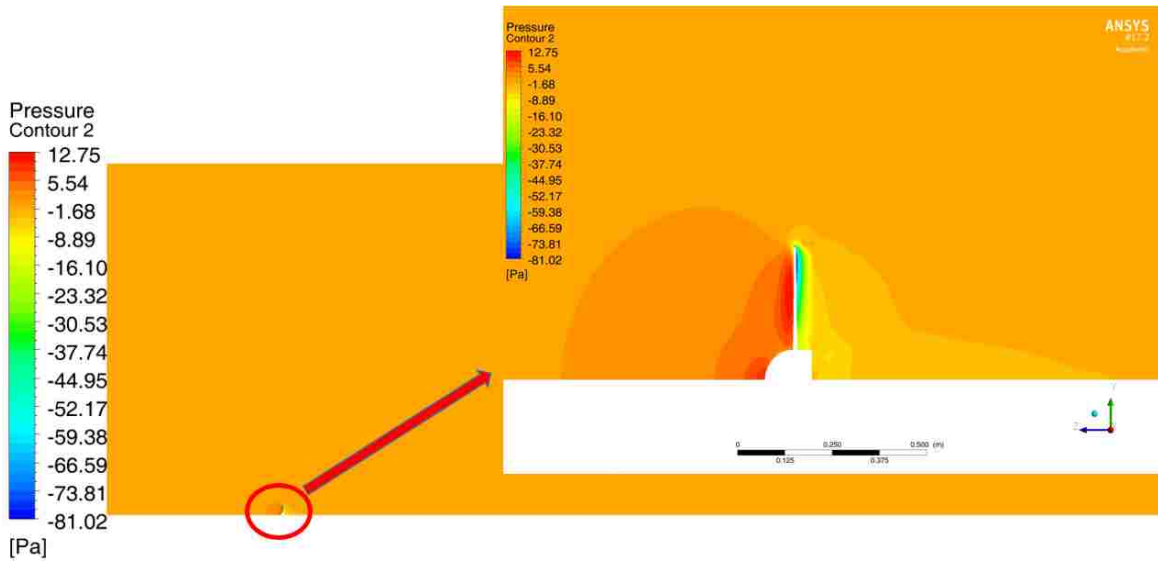


Figure 52: Pressure contour in y-z plane ($9e-4$ m)

The pressure contour shown in Figure 53 shows a slight difference from the previous 4 m/s test as there appears to be an increase in the low pressure zone behind the blade hub. The slight differences in the scale of the contour plot could explain part of it as well as the increased pressure difference seen in Figures 49 and 50.

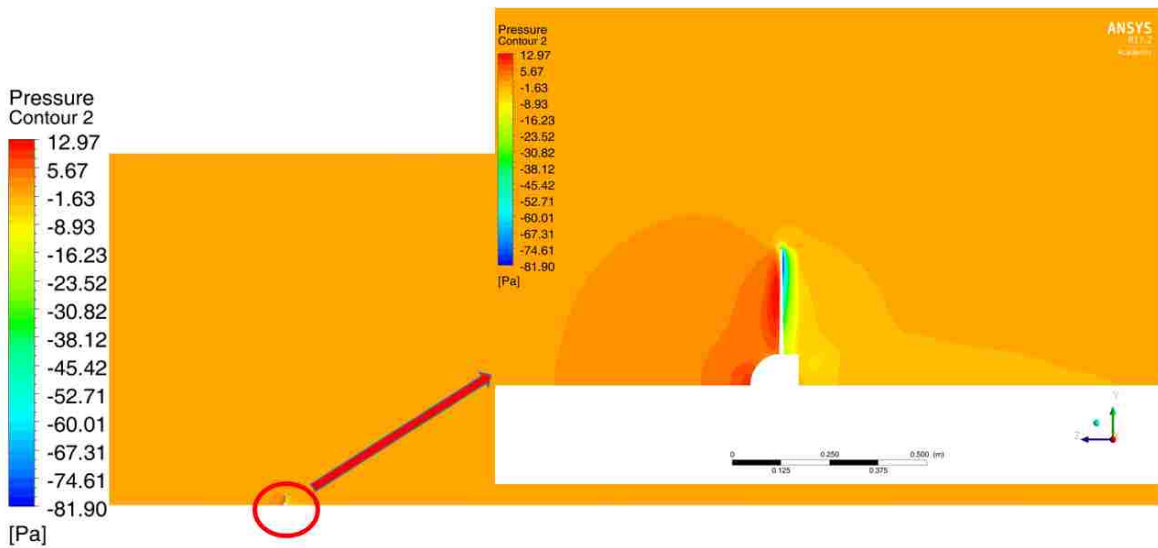


Figure 53: Pressure contour in y-z plane ($7e-4$ m)

Overall the results of 4 m/s testing are consistent with the previous 6 m/s testing with no major differences in velocity or pressure being reported.

4.3 Initial 8 m/s Mesh Testing

As with the 4 m/s testing, the two same meshes were used for the 8 m/s testing. For $9e-4$ m blade sizing, the torque produced is 0.448 N-m, producing 43.0 W of power. The actual value of the torque and power should be 0.44 N-m and 42.24 W- which is a percent difference of 1.82%.

Next the $7e-4$ m blade sizing mesh was run producing a torque of 0.459 N-m generating 44.07 W of power. The actual values of torque and power are 0.44 N-m and 42.24 W respectively- a percent difference of 4.32%.

Given the higher velocity, the y^+ value increased to a maximum of 3.844 for the $9e-4$ m blade sizing as shown in Figure 53. While a y^+ of one is preferred for the $k-\omega$ SST turbulence model, a value of up to about five is still acceptable. The value is still within the range, but a change in inflation thickness is required for further refinement and it will be discussed in Section 4.4.

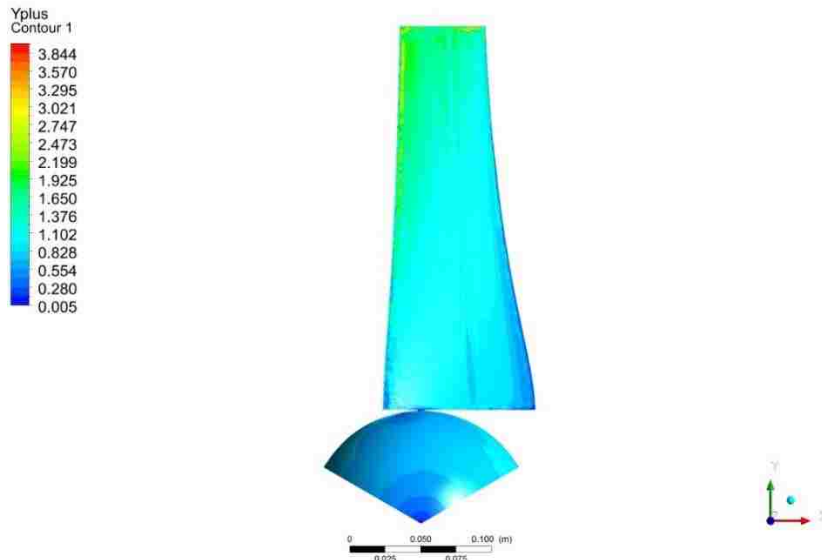


Figure 54: y^+ blade surface ($9e-4$ m)

The y^+ contour for the $7e-4$ m blade sizing shown in Figure 55 shows a value of almost 4, although acceptable for the model choice, the inflation layer needs to be refined to get a more trustable value.

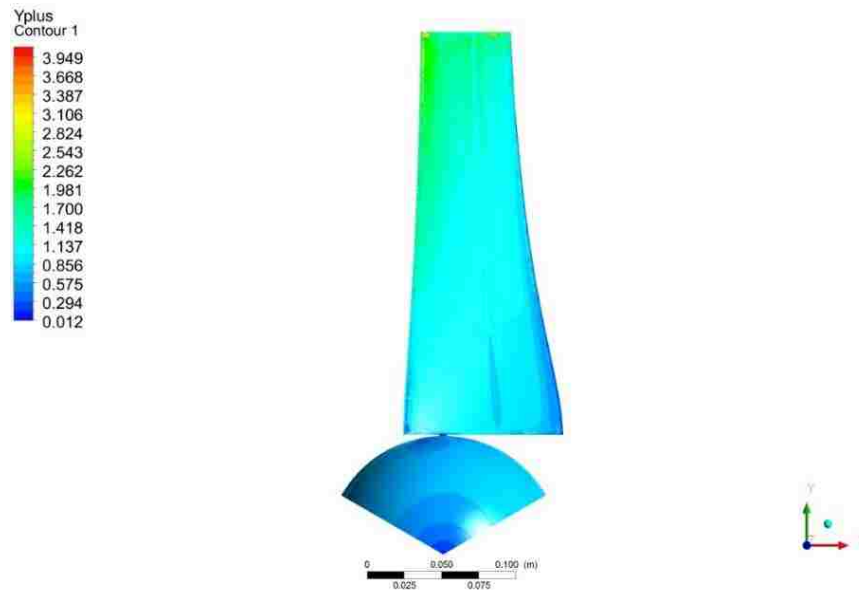


Figure 55: y^+ blade surface ($7e-4$ m)

The velocity in the stationary frame for the $9e-4$ m blade sizing as shown in Figure 56 is similar to the previous speeds tested with a larger low velocity zone on the suction side of the blade at the tip due to the higher velocity being tested.

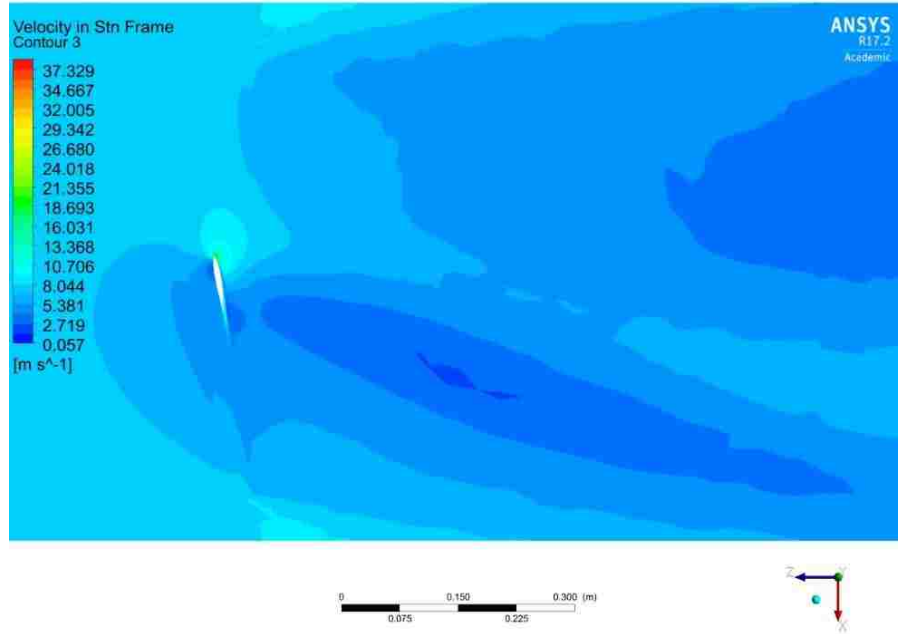


Figure 56: Velocity in stationary frame contour on 0.2 m slice in y-direction ($9e-4$ m)

The velocity in the stationary frame for the $7e-4$ m blade sizing shown in Figure 57 is consistent with the previous mesh and shows no radical changes in flow.

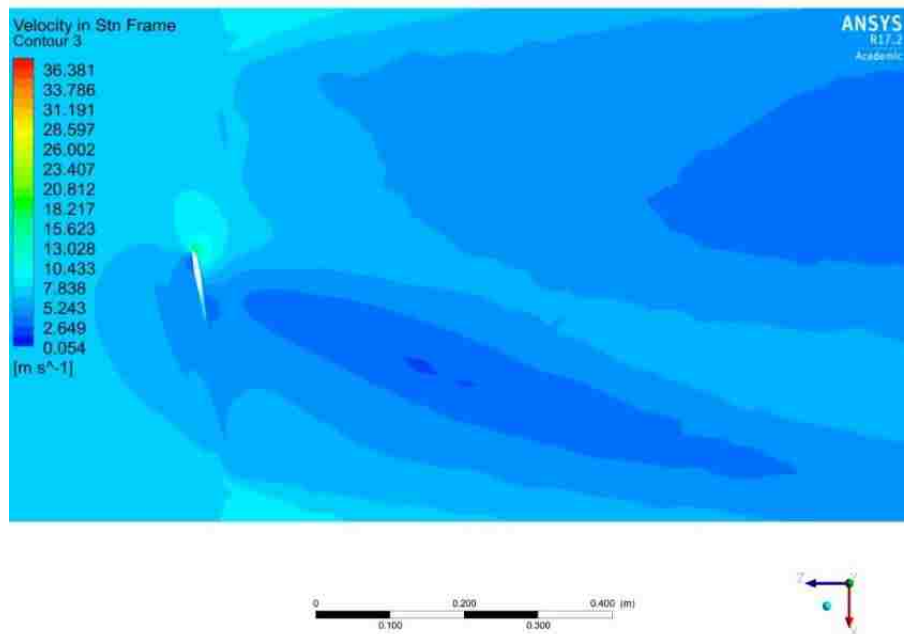


Figure 57: Velocity in stationary frame contour on 0.2 m slice in y-direction ($7e-4$ m)

The pressure contour for the 9e-4 m blade sizing shown in Figure 58 shows magnitude increases consistent with the higher wind speeds.

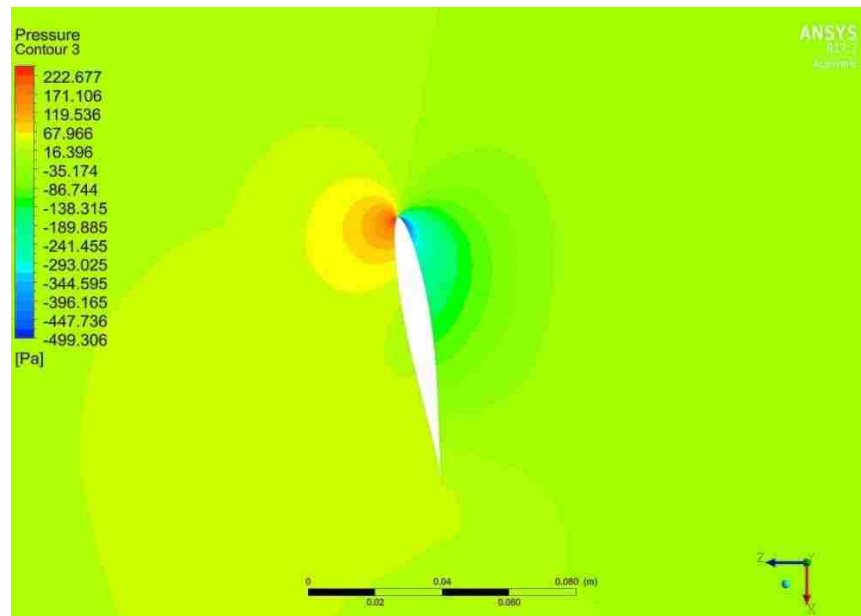


Figure 58: Pressure contour on 0.2 m slice in y-direction (9e-4 m)

The pressure contour for the 7e-4 m blade sizing shown in Figure 59 shows a much higher negative pressure than the previous 8 m/s testing by a difference of about 15%, higher than the 6 m/s testing by about 2%. The higher percent difference could be explained by the higher wind velocities being discovered by resolving the mesh on the blade.

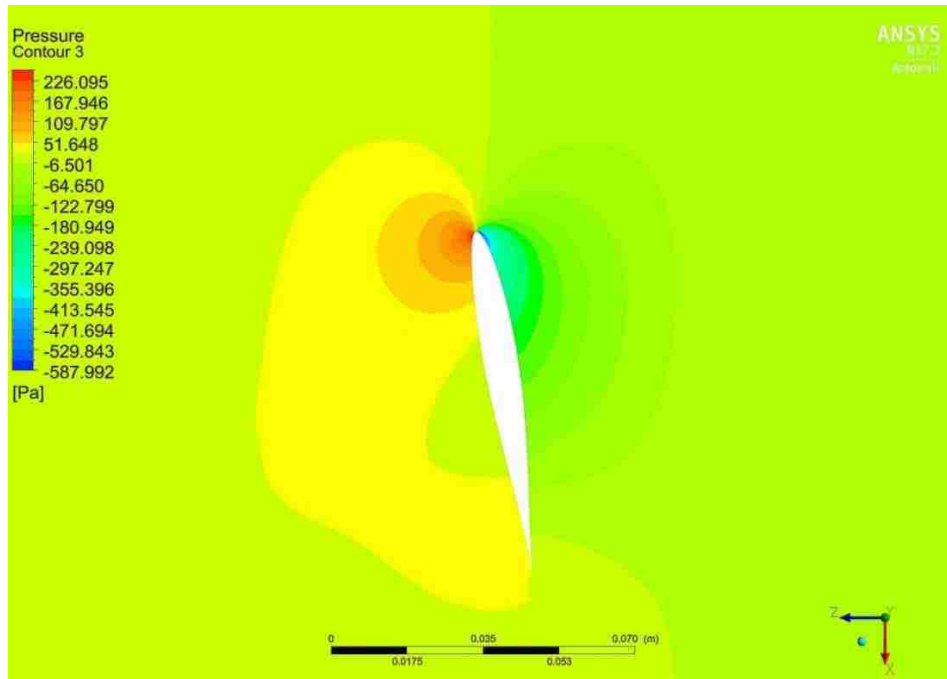


Figure 59: Pressure contour on 0.2 m slice in the y-direction ($7e-4$ m)

The velocity in the stationary frame for the $9e-4$ m blade sizing shown in Figure 60 has no major differences in flow path aside from larger velocity magnitudes that accompany the higher incoming wind speed and subsequent increased rotating speed.

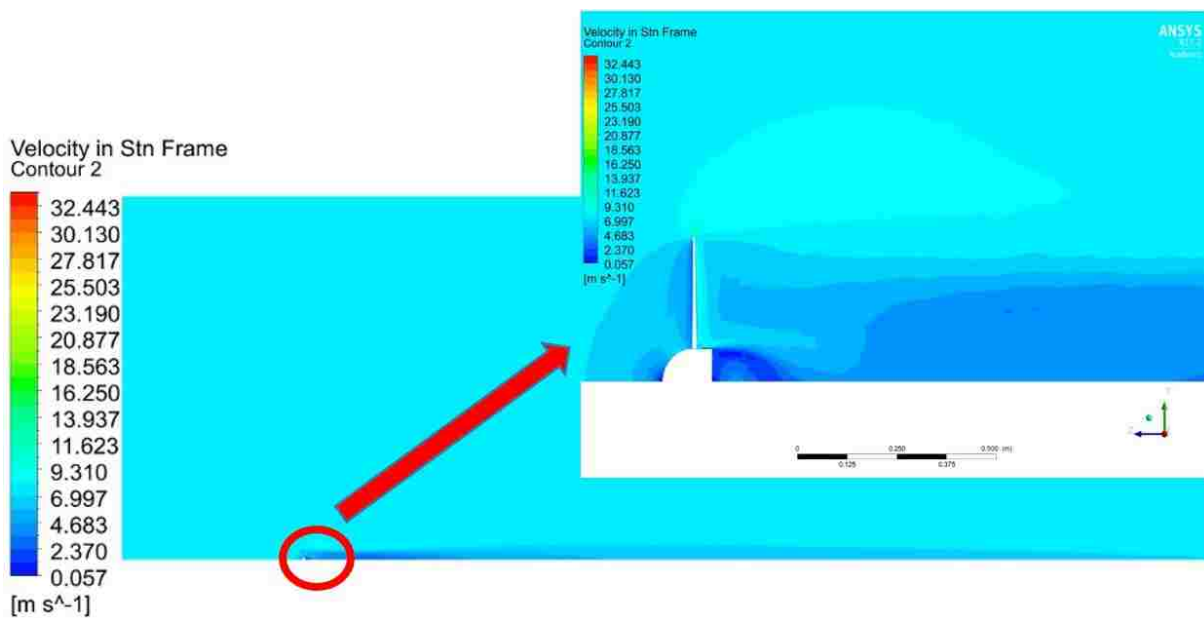


Figure 60: Velocity in the stationary frame in y-z direction ($9e-4$ m)

The velocity in the stationary frame for the 7e-4 m blade sizing shown in Figure 61 is almost the same as the previous mesh with no major differences in the flow even when zoomed in.

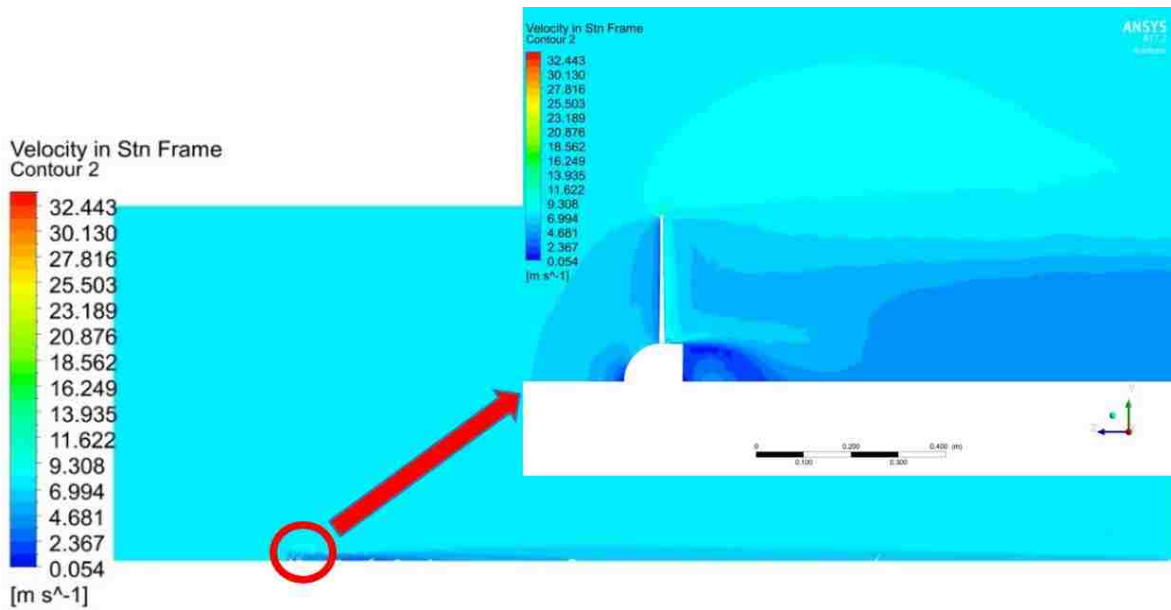


Figure 61: Velocity in the stationary frame in the y-z plane (7e-4 m)

The pressure contour for the 9e-4 m blade sizing shown in Figure 62 is very similar to previous tests and demonstrates no real differences aside from a large magnitude increase caused by the higher wind velocity.

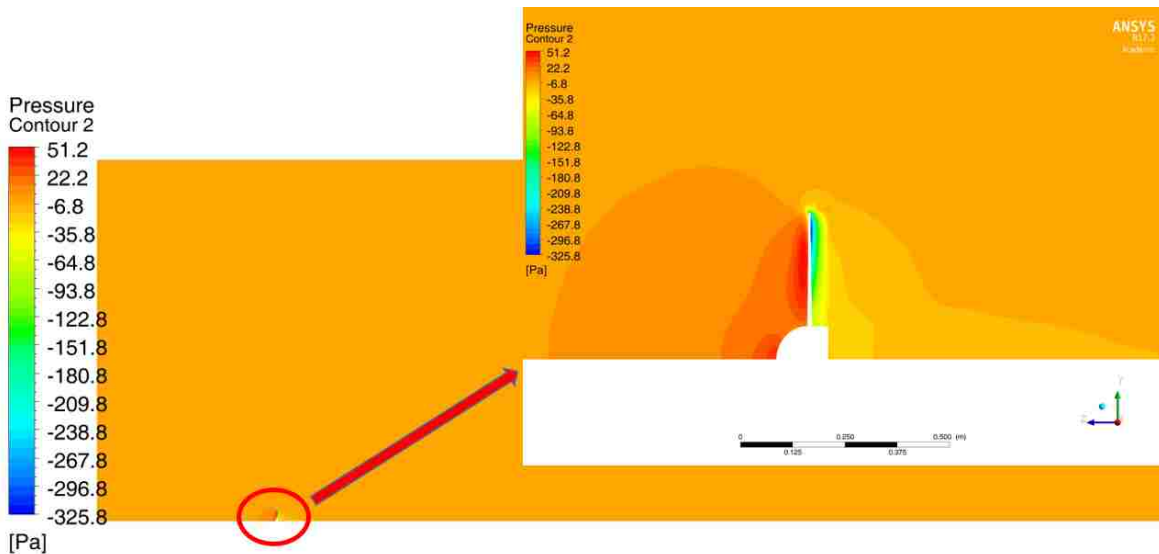


Figure 62: Pressure contour in y-z plane (9e-4 m)

No real major difference in pressures can be seen with the increase in blade sizing resolution as seen in Figure 63 for the $7e-4$ m blade sizing.



Figure 63: Pressure contour in y-z plane ($7e-4$ m)

Overall the mesh that was used previously for both 4 and 6 m/s wind speeds produces reasonable values for 8 m/s wind speeds, however as will be discussed in the next section, the higher y^+ values should be reduced.

4.4 Final Results for All Wind Speeds

Although there was a finer mesh option-0.035 m refinement- available it was decided that the added computational expense did not show enough difference to be used for all wind speeds. The mesh choice that was chosen to simulate the three wind speeds was the setting with a $1.5e-5$ m first layer thickness, a $7e-4$ m blade sizing, and a 0.04 m refinement sizing. The mesh consisted of 5,690,632 nodes and 29,317,802 elements.

For a wind speed of 4 m/s, the torque was 0.111 N-m generating a power of 5.32 W, the percent difference compared to the actual value is 0.82%.

Next, the same mesh was used with a wind speed of 6 m/s. The torque produced was 0.256 N-m generating 18.43 W of power. Compared to the actual values of 0.2475 N-m and 17.82 W, the results are only 3.43 % different.

During the 6 m/s test, the lift to drag was calculated using ANSYS-Fluent[®] ratio for the blade was found to be about 13.3 very crudely assuming the average chord length between the tip and largest portion of the airfoil near the base of 0.08915 m. The only way to test the lift and drag was including the hub in the calculation that will add a lot of drag to the system. Between the large uncertainty of the BEMT method, the inclusion of the hub and the averaging of the chord ratio, the result of 13.3 compared to the BEMT prediction of 23 appears reasonable.

Next the 8 m/s tests were run using the same mesh as the previous 4 and 6 m/s tests in this section. The torque from the simulation equals 0.462516 N-m producing a power of 44.4 W. Compared to the actual value of torque and power of 0.44 N-m and 42.24 W, the percent difference is 5.23%. The highest speed tested demonstrates the largest percent difference in power.

The results of torque across wind speeds are summarized in Table 12. The values compare really well to the actual torque values from experimental data with the highest percent difference being 5.227%.

Table 12: Summary of torque for multiple wind speeds

Wind Speed (m/s)	Torque (N-m)	Actual Torque (N-m)	Power (Watts)	Actual Power (Watts)	Torque Percent Difference
4	0.111	0.110	5.323	5.280	0.818
6	0.255	0.247	18.424	17.82	3.393
8	0.463	0.440	44.448	42.24	5.227

Figure 64 shows the general streamlines of the flow for 4 m/s. The Figures of the streamlines are not intended to show velocity differences in fine detail, but more of a picture showing the general fluid flow around the blade. The streamlines only impact the blade surface so that the blade effects can be seen easier, especially the tip vortices at the tips of the blades.

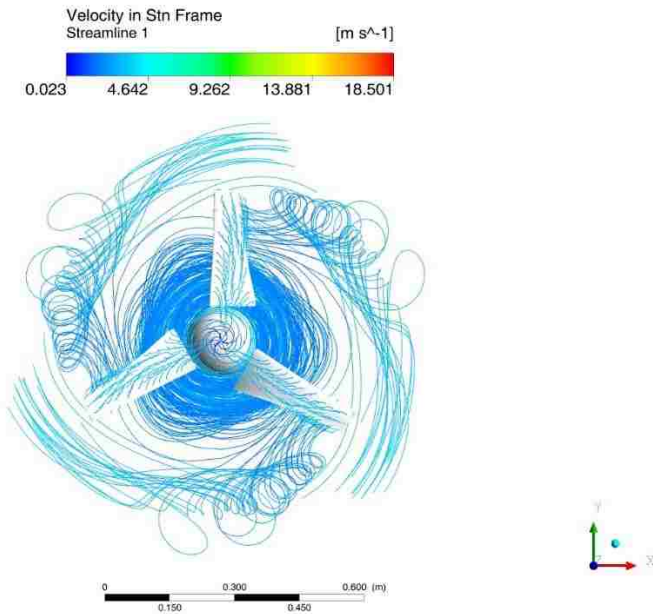


Figure 64: Streamline of velocity in stationary frame for 4 m/s

Figure 65 shows the streamlines of the velocity in the stationary frame for 6 m/s. The flow is very similar to the 4 m/s testing with higher magnitudes of velocity present due to the higher rotating speed and higher wind speed.

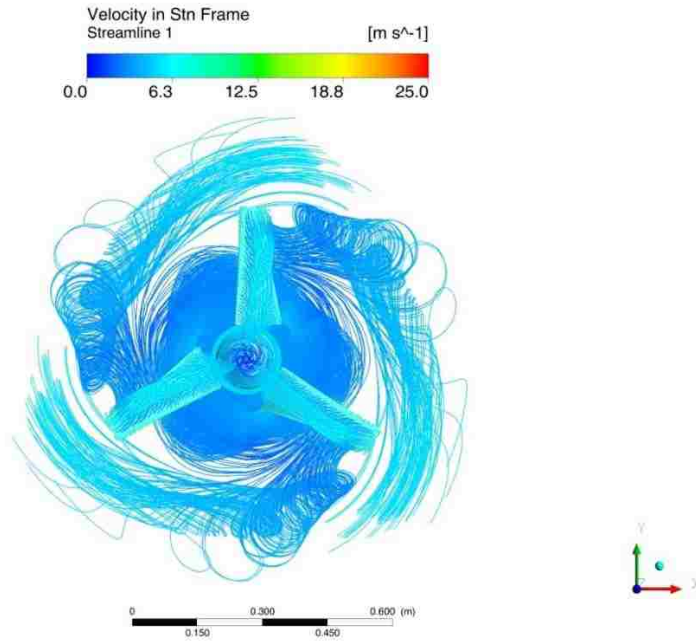


Figure 65: Streamline of velocity in stationary frame for 6 m/s

The streamlines for the 8 m/s wind speed are shown in Figure 66. The tip vortices are consistent with the other simulations.

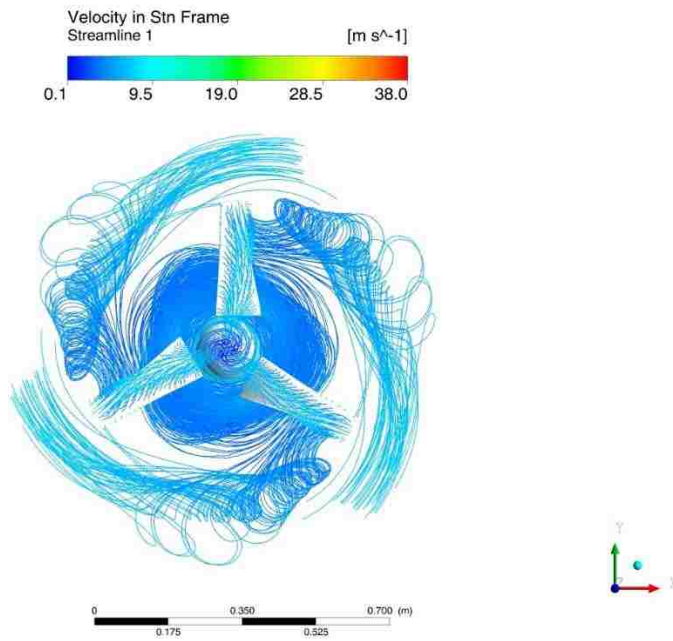


Figure 66: Streamline of velocity in stationary frame for 8 m/s

The y^+ values shown in Figure 67 for 4 m/s and are improved from the previous inflation sizing that had a value of greater than two with the maximum value for the blade tip being reduced to about 1.3.

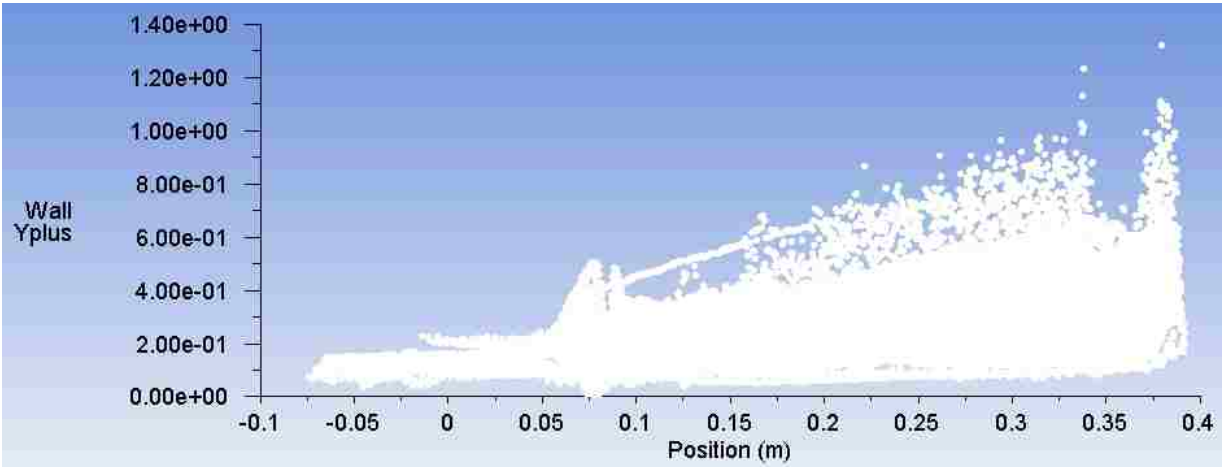


Figure 67: y^+ blade surface in x, y, and z directions (4 m/s)

Figure 68 shows that the maximum y^+ value is about 1.9 for a wind speed of 6 m/s, an improvement over the previous 6 m/s testing as the previous value was over 3.

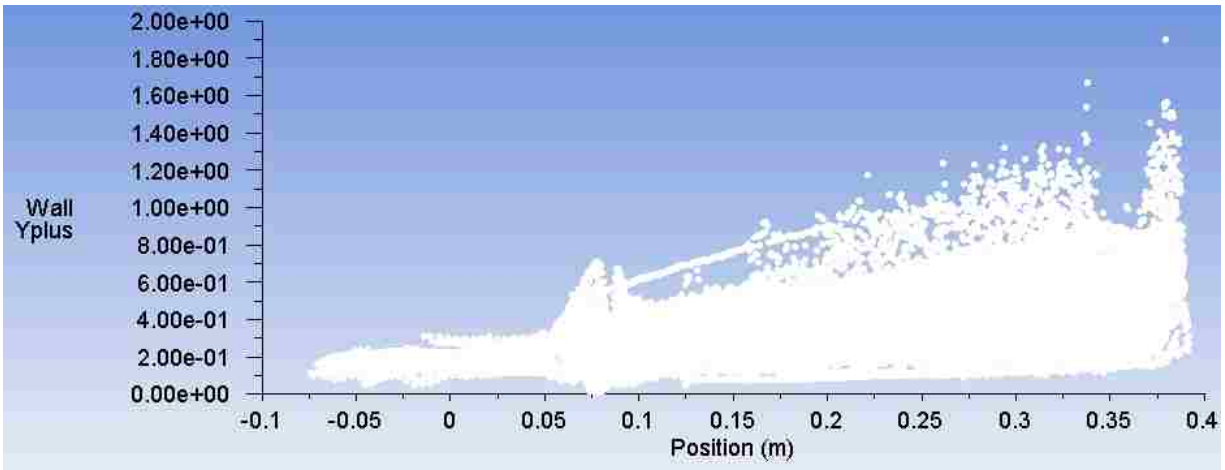


Figure 68: y^+ blade surface in x, y, and z directions (6 m/s)

The y^+ plot shown in Figure 69 for a wind speed of 8 m/s shows an improved y^+ of about 2.5, a reduction by almost 60% compared to the highest refinement from Section 4.3.

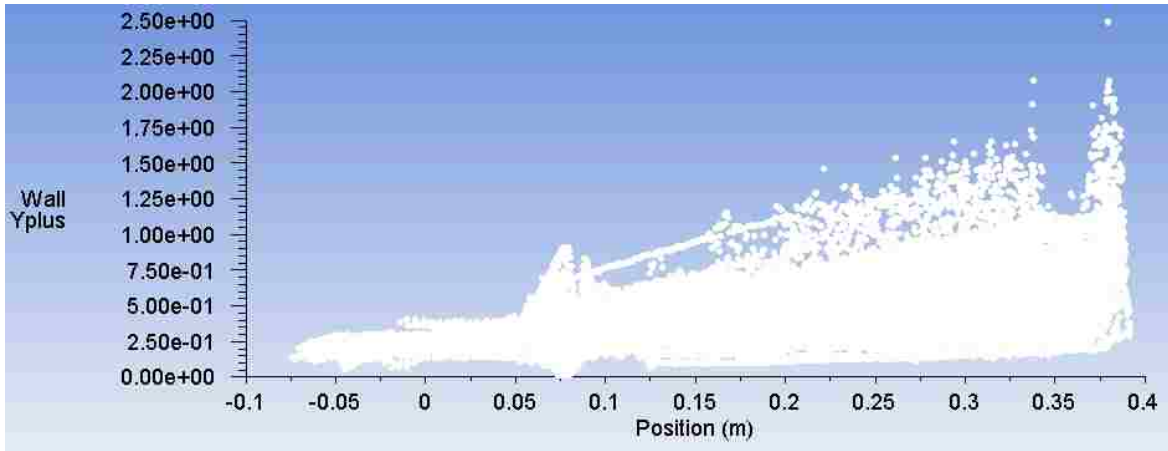


Figure 69: y^+ plot for blade surface in x, y, and z, directions (8 m/s)

The velocity in the stationary frame slice shown in Figure 70 for a wind speed of 4 m/s is almost identical to the previous tests described in Section 4.2.

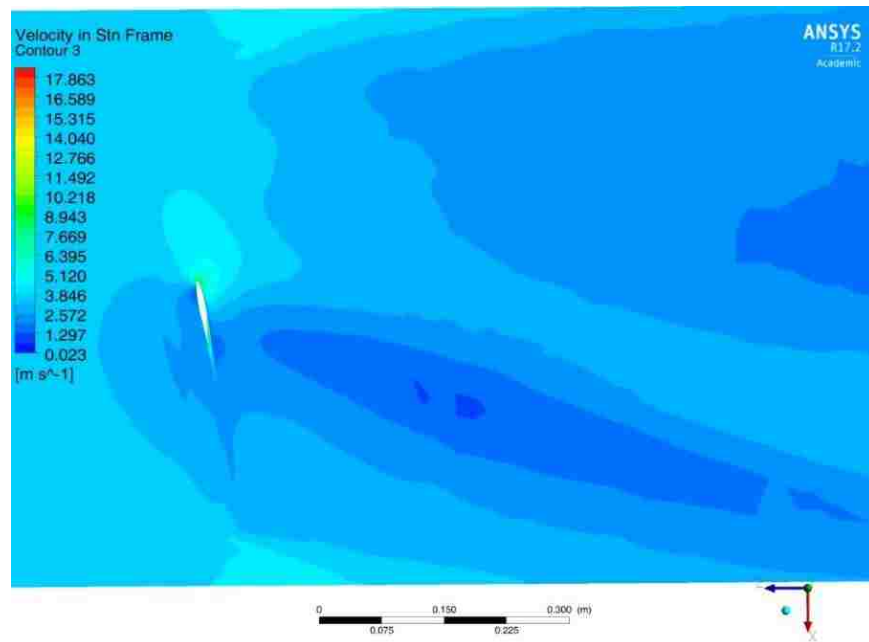


Figure 70: Velocity in stationary frame contour on 0.2 m slice in y-direction (4 m/s)

The velocity contour shown in Figure 71 for a wind speed of 6 m/s shows a similar profile compared to the highest refinement for 6 m/s in Section 4.1, with better resolution shown with a more defined center to the wake behind the blade, which is much smaller for the previous test.

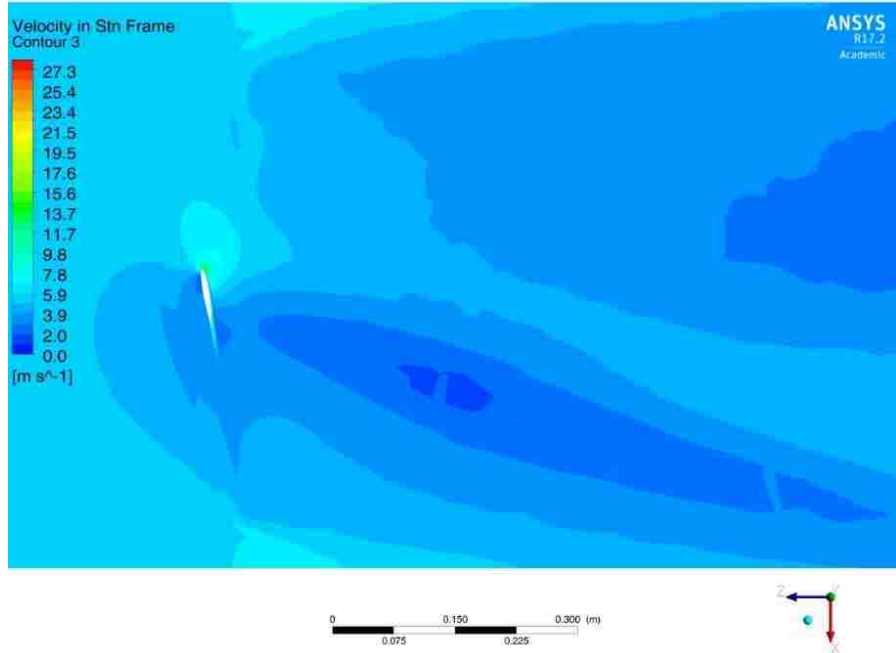


Figure 71: Velocity in stationary frame contour on 0.2 m slice in y-direction (6 m/s)

The velocity contour shown in Figure 72 for a wind speed of 8 m/s shows similar characteristics to other 8 m/s tests with improved resolution due the 0.04 m refinement sizing.

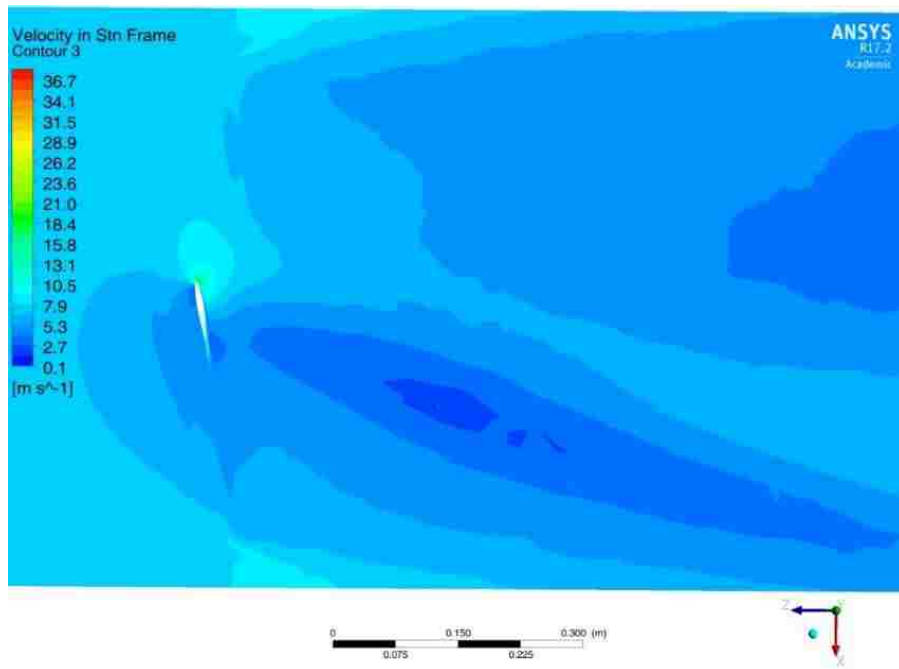


Figure 72: Velocity in stationary frame contour on 0.2 m slice in y-direction (8 m/s)

The pressure contour shown in Figure 73 for the 4 m/s wind speed exhibits a larger negative pressure than previous testing by about 6.8%. There are also more color bands present than were present in the previous test due to the larger difference in pressure present.

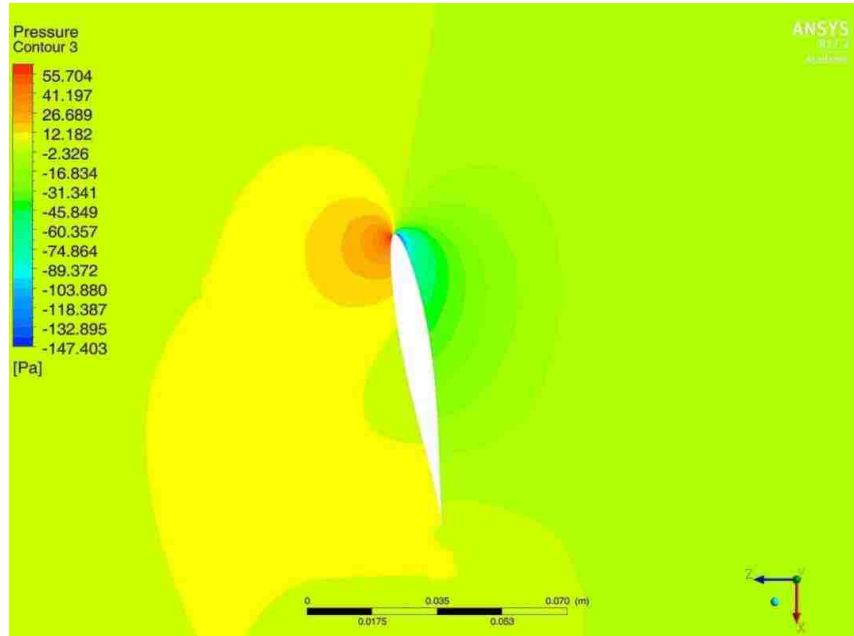


Figure 73: Pressure contour on 0.2 m slice in y-direction (4 m/s)

The pressure contour shown in Figure 74 for a 6 m/s wind speed has a difference of about 3% for the lowest pressure compared to the $7e-4$ m blade sizing, $3e-5$ m first layer thickness, and 0.05 m refinement.

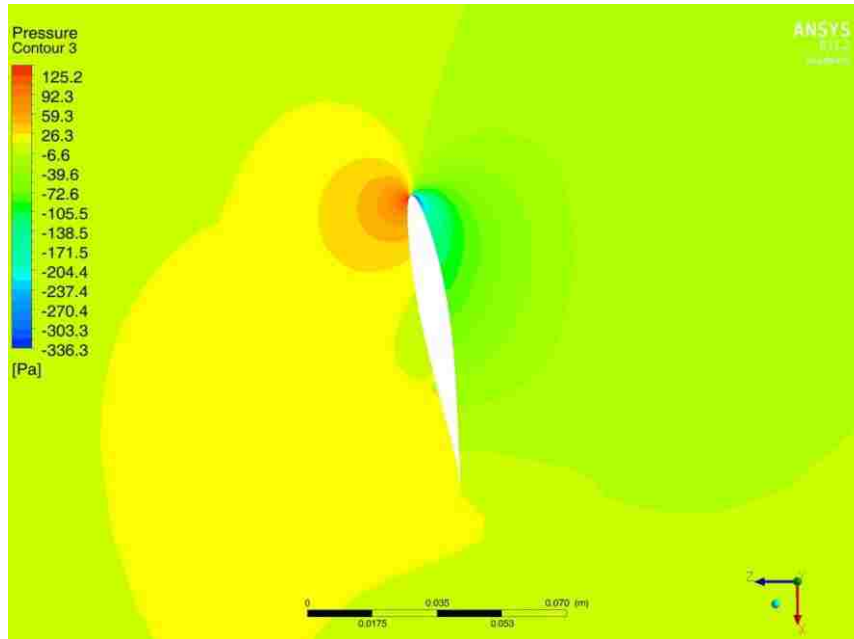


Figure 74: Pressure contour of 0.2 m slice in y- direction (6 m/s)

The pressure contour in Figure 75 for a wind speed of 8 m/s shows a percent difference compared the highest refinement testing in Section 4.3 of about 2.65%.

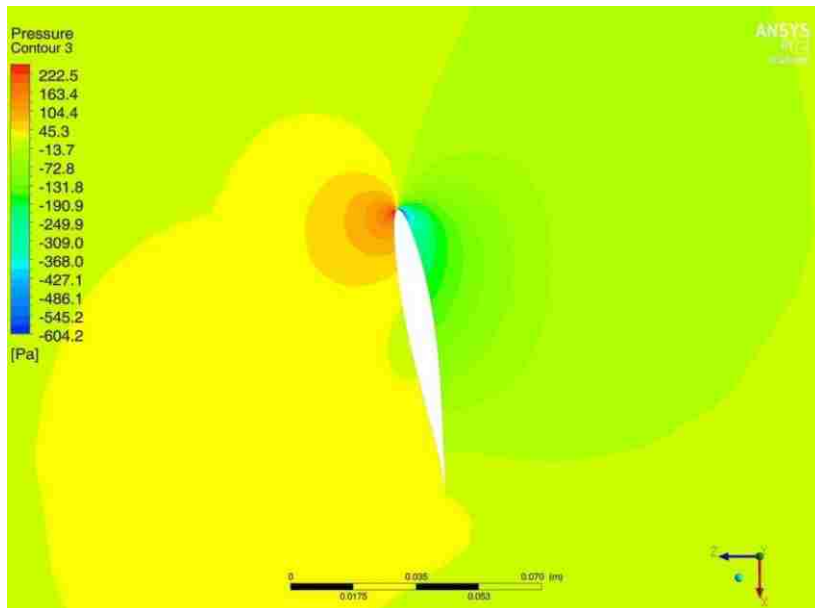


Figure 75: Pressure contour of 0.2 m slice in y-direction (8 m/s)

The velocity in the stationary frame shown in Figure 76 for a wind speed of 4 m/s presents the same general characteristics as previously described in Section 4.2.

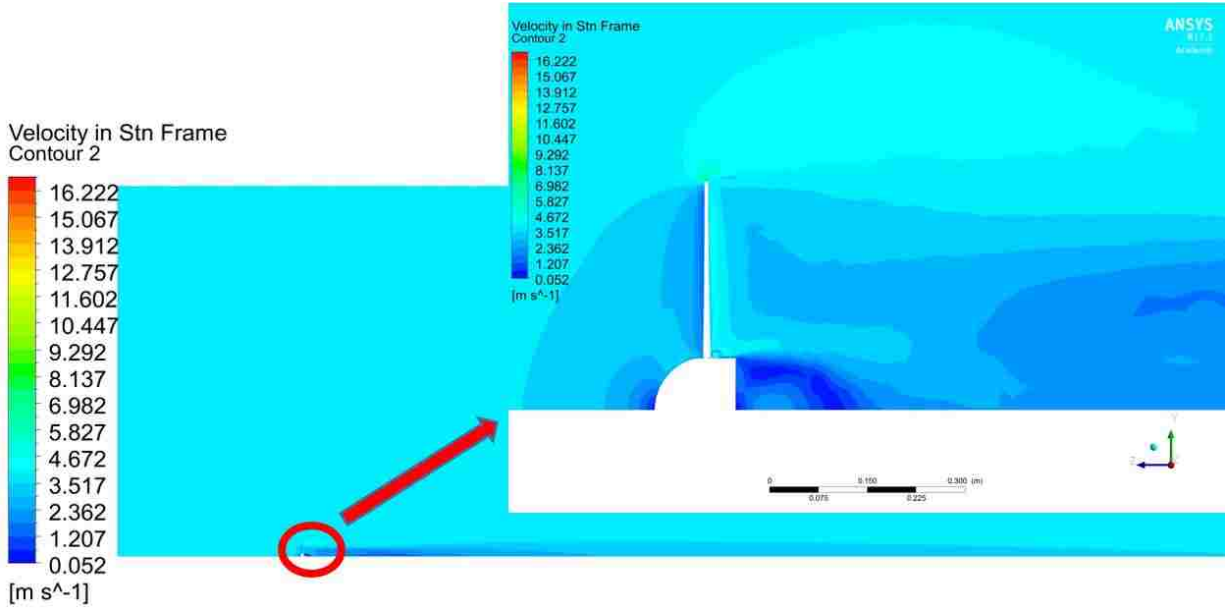


Figure 76: Velocity in stationary frame contour in y-z plane (4 m/s)

The velocity contour shown in Figure 77 for a wind speed of 6 m/s shows the same consistent flow path that has been seen throughout testing in Section 4.1.

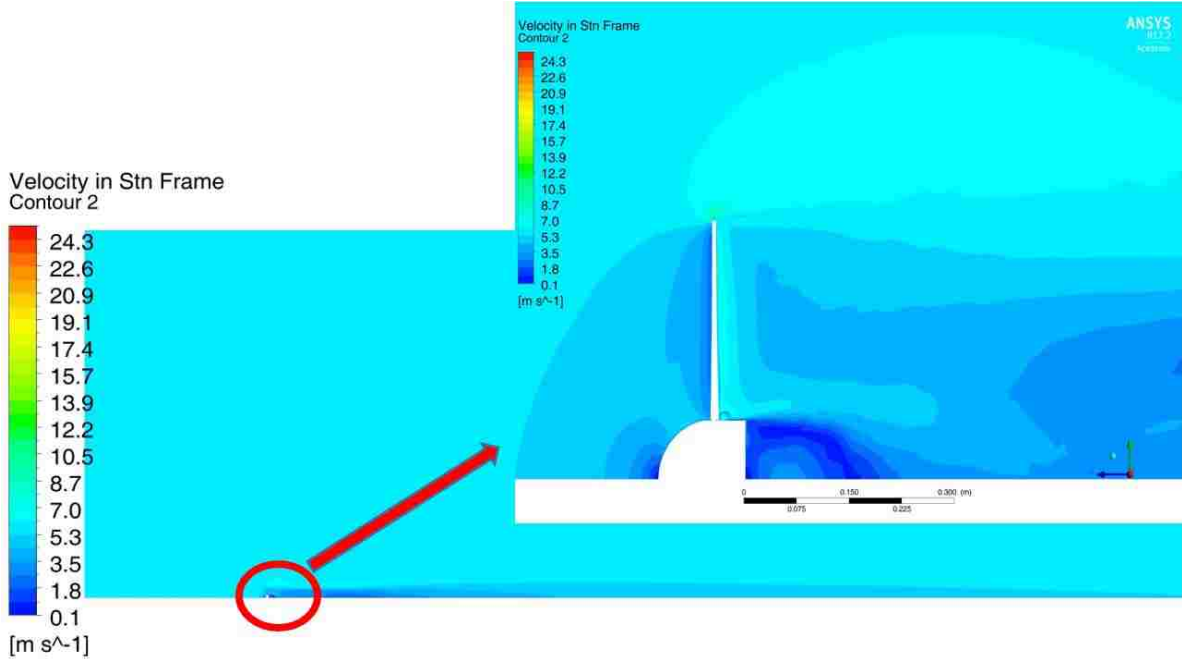


Figure 77: Velocity in stationary frame contour in y-z plane (6 m/s)

The velocity contour for Figure 78 for a wind speed of 8 m/s is similar to previous tests and they have remained consistent throughout all testing for 8 m/s. The improvement in resolution of the refinement setting to 0.04 m shows better refinement in the contour, especially behind the blade.

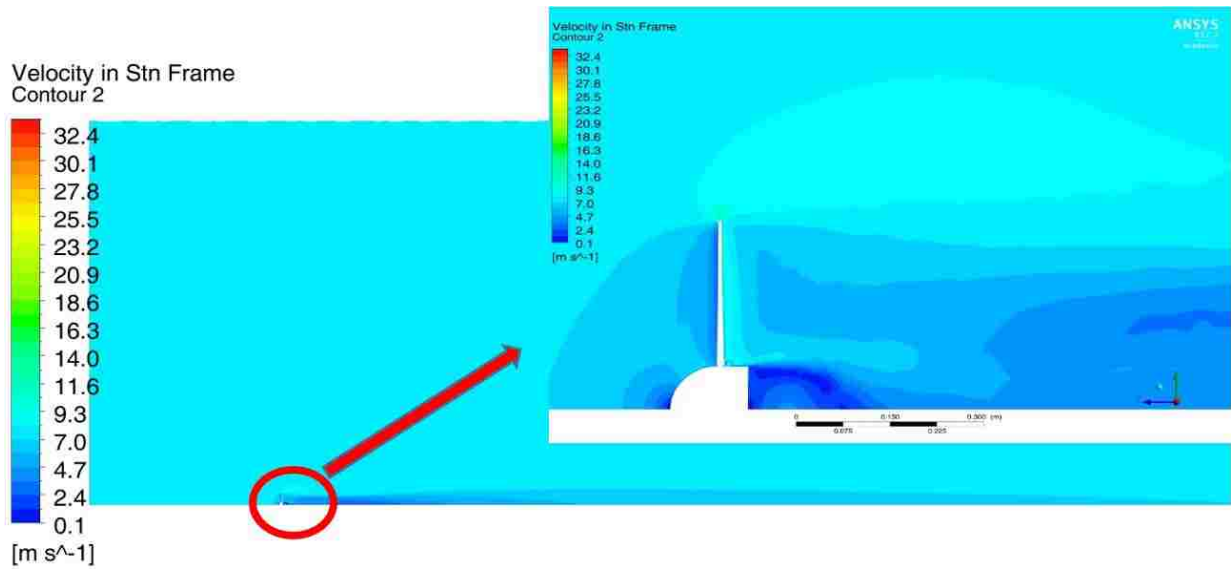


Figure 78: Velocity in stationary frame contour in y-z plane (8 m/s)

The pressure contour for a 4 m/s wind speed shown in Figure 79 shows similar characteristics to the previous tests in Section 4.2.

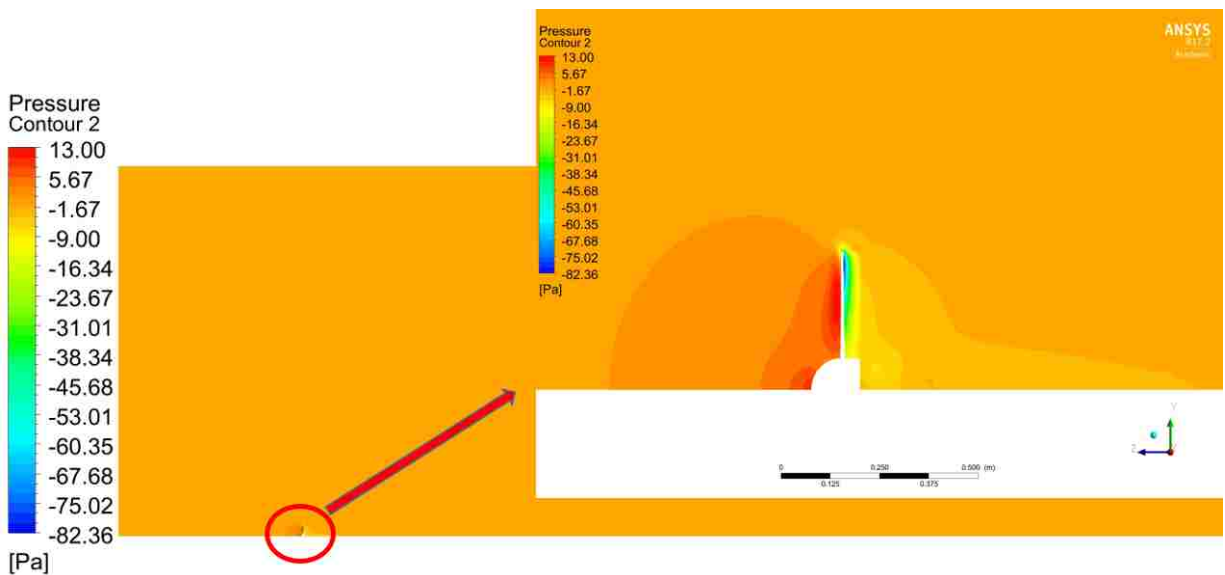


Figure 79: Pressure contour in y-z plane (4 m/s)

The pressure contour shown in Figure 80 shows consistent trends as previously shown in Section 4.1.

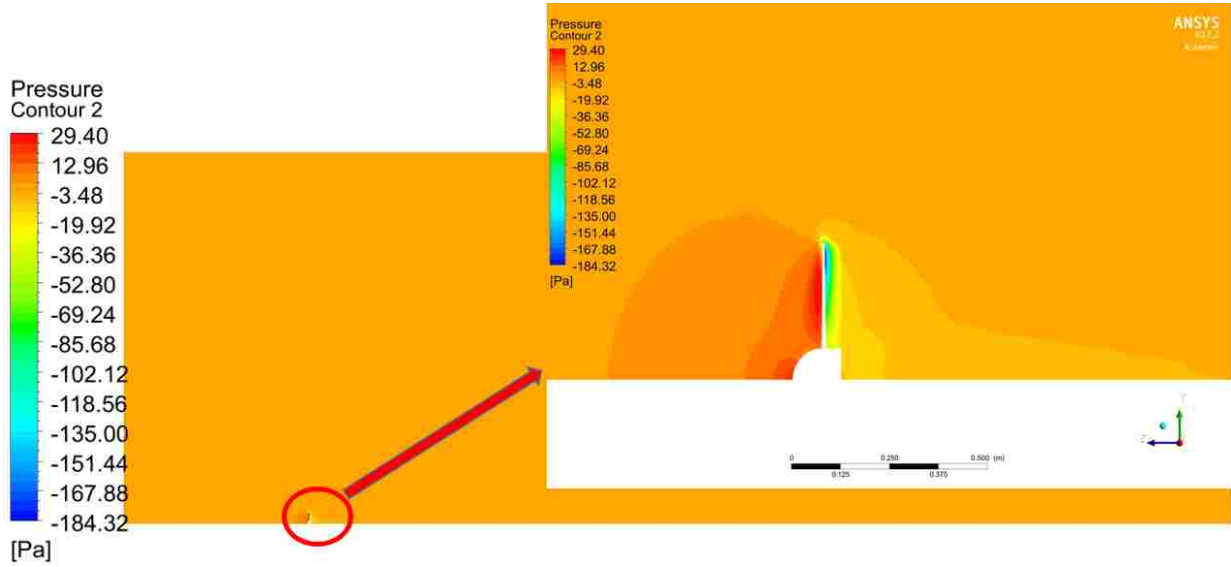


Figure 80: Pressure contour in y-z plane (6 m/s)

The pressure contour for a wind speed of 8 m/s shown in Figure 81 shows the pressure characteristics as the previously seen for the 7e-4 m blade sizing testing for 8 m/s in section 4.3.



Figure 81: Pressure contour in y-z plane (8 m/s)

Conclusions and Future Work

5.1 Conclusions

Ultimately, it was found that while the BEMT method can produce reasonable results, its uncertainty is so high that its values produced need to be compared to numerical methods to get accurate results.

Numerical simulations are heavily reliant on good meshes as to why so many sizing tests were done. Even at different speeds, the numerical simulation produced values that were very close to the actual output of the system. Due to the nature of unstructured meshes there are still some changes when refinements are made, but from refinement to refinement all within 10% for velocity and 13% for pressure.

In the case of the bare wind turbine testing, the results compared very well, with the torque being 0.818% different for 4 m/s, 3.393% different for 6 m/s, and 5.227% different for 8 m/s compared with the torque from Ohya et al. (2008) bare wind turbine results.

5.2 Future Work

As previously mentioned, it is the hope that this work is continued in the future to incorporate shrouding to the bare wind turbine provided in this work with the ultimate goal of improving shrouded wind turbines.

To improve mesh independency, future work could be to develop a structured mesh to better capture the flow downstream of the wind turbine. Other ideas on future work recommended for this project are as follows. Having fluid-structure interaction (FSI) within the model for the turbine blade. Adding a pitch control in the model to optimize flows better would also be beneficial. The static stall and dynamic stall flow speeds were not investigated in this simulation

given the low speeds of operation and difficulties of RANS solvers, for future work they can be investigated further with other numerical methods such as LES solvers.

Appendix A: BEMT MATLAB[®] Code

Shown below is a code developed in MATLAB[®] to create a wind turbine blade using the blade element and momentum theory (BEMT).

```
clc
clear
format long
%% Variable Design Parameters
N=50; %number of blade segments
% Air Characteristics
uinf=6; %Free stream velocity (m/s)
ulow=uinf-2; % Lower Boundary (m/s)
uhigh=uinf+2; %Higher Boundary (m/s)
p=1.225; %Density in kg/m^3 (back calculated from comparison paper)
nu=1.7894e-5/p; %Kinematic Viscosity of air (m^2/s)
Tol=1e-6; %tolerance
%% Shroud Amplification Factor
K=1.59; % Wind Velocity amplification from shroud (just before rotor)
u_blade=K*uinf;
%% Fixed Design Parameters
Dr=.7; %Rotor diameter (m)
Rtip=Dr/2; %Tip Radius (m)
D_Dif=0.72; %Shroud Diameter near blades
Dh=0.22*D_Dif; %Hub Diameter (m)
Rhub=(Dh/2)+1e-3 ; %Hub Diameter (m)
lambda=4.2; %tip-speed ratio;
Zb=3; %number of blades
A=pi*Rtip^2; %blade Area (m^2)
w=u_blade*lambda/Rtip; %expected angular velocity (rad/s)
r=linspace(Rhub,Rtip,N); %local radius (m)
r_R=r./Rtip; %local radius to tip radius
lambdar=lambda*r_R; %local lambda values depending on radius
%% Initalize Iterative Design Parameters
phi = zeros(2,N);
a=zeros(2,N);
aprime=zeros(2,N);
Cw_bare=zeros(2,N);
dQ=zeros(2,N);
dT=zeros(2,N);
F=zeros(2,N);
Final_Blade=zeros(51,3*N);
%% AOA for NACA 63210
%Blade Data for RE= 50000
```



```

alpha_data=[-2.5,-2.25,-2,-1.75,-1.5,-1.25,-1,-0.75,-0.5,-
0.25,0,0.25,0.5,0.75,1,1.25,1.5,1.75,2,2.25,2.5,2.75,3,...
3.25,3.5,3.75,4,4.25,4.5,4.75,5,5.25,5.5,5.75,6,6.25,6.5,6.75,7,7.25,7.5,7.75,8,8.25,8.5,8.75,9,9.2
5,9.5,9.75];
Cl_data=[-0.1089,-0.0414,-0.0165,-0.0247,-0.0371,-0.0517,-0.0676,-0.0841,-0.0975,-0.0972,-
0.0843,-0.0664,-0.0469,...
-0.0268,-
0.0064,0.0138,0.0362,0.0811,0.1239,0.1645,0.2042,0.2424,0.2801,0.3172,0.3544,0.3945,0.4421,
0.4708,...

0.5236,0.5772,0.6805,0.6853,0.6752,0.6915,0.7183,0.7524,0.7863,0.8188,0.844,0.867,0.8884,0.
9068,0.9222,...
0.9398,0.9294,0.9361,0.9094,0.9018,0.8494,0.8109];
Cd_data=[0.02203 0.02096 0.02043 0.02034 0.02028 0.02018 0.01999 0.01972 0.0194
0.01926 0.01934 0.01958 0.01991...
0.02031 0.02077 0.02129 0.02191 0.02305 0.02415 0.02521 0.02626 0.02728 0.02829
0.02928 0.03025 0.0312 0.0321...
0.03292 0.03334 0.03295 0.02243 0.02044 0.02437 0.02659 0.02844 0.03046 0.03262
0.03548 0.03781 0.04047 0.04369...
0.04733 0.05134 0.05604 0.06054 0.0659 0.07169 0.07775 0.0842 0.09392];
%Optimal value for AOA
G=(Cl_data./Cd_data);
G1=max(G); G2=find(G==G1);
alpha_optimal=alpha_data(G2); %max Cl/Cd ratio
%Chosen Initial AOA for throughout the blade
alpha(1,1:N)=linspace(6.5,.95*alpha_optimal,N);
% Curve fit Cl and Cd for RE=50,000(6th order polynomial)
cl(1,:)=1E-06.*alpha(1,:).^6 - 3E-05.*alpha(1,:).^5 - 0.0001.*alpha(1,:).^4 + 0.002.*alpha(1,:).^3
+ 0.0068.*alpha(1,:).^2 + 0.0697.*alpha(1,:) - 0.0365;_
cd(1,:)=3E-08.*alpha(1,:).^6 + 2E-07.*alpha(1,:).^5 + 9E-06.*alpha(1,:).^4 - 8E-
05.*alpha(1,:).^3 + 3E-05.*alpha(1,:).^2 + 0.0018.*alpha(1,:) + 0.0216;
%% Initial Design Parameters (phi, a and a')
% Initial Guess for Phi
Phi_initial=lambdar.^-1;
phi(1,:)=(2/3).*atand(Phi_initial); %Initial relative flow angle
pitch=phi(1,:)-alpha(1,:); %Pitch
Twist=pitch(1)-pitch(N); %Total Twist of Blade
c=8.*pi.*r.*(1-cosd(phi(1,:)))./(Zb.*cl(1,:)); %Theoretical Chord Distribution for blade with
wake rotation
re_chord=(c)*u_blade./nu; %check to make sure reynolds number is around 50,000
RE_blade=sum(re_chord)/N; %average reynolds number of blade
sp(1,:)=Zb.*c./(2.*pi.*r); %Local blade solidity (ideally, solidity is between 0.01 and 0.7)
%Initial Guesses for a and a'
a1=4.*((sind(phi(1,:))).^2); a2=sp.*cl(1,:).*cosd(phi(1,:));
a(1,:)=1/3; %initial guess for a equal to ideal axial induction factor

```

```

a(2,:)=1./(1+(a1./a2)); %initial calculated guess for axial induction factor
aprime(2,:)=(((1-3*a(2,:))./(4*a(2,)-1)));
%% Loop
maxit=5000;
i=1;
while (1)
    i = i + 1;
    %New Phi Value
    phi(i,:)=atand((1-a(i,:))./(lambdar.*(1+aprime(i,:))));
    phi(i,N)=(1-1/N)*phi(i,N-1);
    phi(i,1)=(1+2.2/N)*phi(i,2);

    %New Alpha Value
    alpha(i,:)=phi(i,:)-pitch;

    %Find New Cl, Cd Values
    %RE=50,000 (6th order polynomial)
    cl(i,:)=1E-06.*alpha(i,:).^6 - 3E-05.*alpha(i,:).^5 - 0.0001.*alpha(i,:).^4 + 0.002.*alpha(i,:).^3
+ 0.0068.*alpha(i,:).^2 + 0.0697.*alpha(i,:) - 0.0365; %RE=50000_
    cd(i,:)=3E-08.*alpha(i,:).^6 + 2E-07.*alpha(i,:).^5 + 9E-06.*alpha(i,:).^4 - 8E-
05.*alpha(i,:).^3 + 3E-05.*alpha(i,:).^2 + 0.0018.*alpha(i,:) + 0.0216; %RE=50000

    %Hub and Tip losses
    f1=0.5*Zb*(1-r_R)./(r_R.*sind(phi(i,:))); %Tip Loss
    f2=0.5*Zb*(r-Rhub)./(r.*sind(phi(i,:))); %Hub Loss
    F(i,:)=(2/pi).*acos(exp(-f1)).*((2/pi).*acos(exp(-f2)));

    %Find local thrust coefficient
    Ct(i,:)=(sp.*((1-a(i,:)).^2).*(cl(i,:).*cosd(phi(i,:)) + cd(i,:).*sind(phi(i,:))))./((sind(phi(i,:))).^2);
    for T=1:N
        if Ct(i,T)<=0.96
            %disp('Ct<0.96')
            a(i+1,T)=real((1./((4.*F(i,T)).*((sind(phi(i,T))).^2)./(sp(1,T).*cl(i,T).*cosd(phi(i,T))))+1)));
        elseif Ct(i,T)>0.96
            %disp('Ct is greater than or equal to 0.96')
            a(i+1,T)=real((1./F(i,T)).*(0.143 + sqrt(0.0203 -(0.6427.*(0.889-Ct(i,T))))));
        end
    end
    aprime(i+1,:)=real(1./((4.*F(i,:).*cosd(phi(i,:))./(sp(1,:).*cl(i,:)) - 1)));
%% Performance
%% Power coefficient for a bare wind turbine
    Cw_i=F(i,1:N).*((sind(phi(i,1:N))).^2).*(cosd(phi(i,1:N))-
lambdar(1:N).*sind(phi(i,1:N))).*(sind(phi(i,1:N)) + lambdar(1,1:N).*cosd(phi(i,1:N))).*(1-
(cd(i,1:N)...
./cl(i,1:N)).*cotd(phi(i,1:N))).*(lambdar(1,1:N).^2);
    Cw_bare=(8./(lambdar.*N)).*sum(Cw_i);

```

```

%% Torque (bare)
for T=1:N-1
    % Torque per segment
    dQ_bare(i,T)=F(i,T).*(w/K)*pi*(uinf/k)*p.*aprime(i+1,T).*(1-a(i+1,T)).*(r(1,T+1).^4 -
r(1,T).^4);
    end
    Q_bare=sum(dQ_bare(i,:)); % Total torque of bare wind turbine
    % Power
    BEM_Power_Bare=(w/K)*Q_bare;
%% Thrust, Torque Amplified for Current Wind Speed
    % for T=1:N-1
    % dT(i,T)=2*F(i,T)*p*(u_blade^2)*pi.*a(i+1,T).*(1-a(i+1,T)).*((r(1,T+1).^2)-r(1,T).^2);
    % Thrust per segment
    % dQ(i,T)=F(i,T).*(w)*pi*(u_blade)*p.*aprime(i+1,T).*(1-a(i+1,T)).*(r(1,T+1).^4 -r(1,T).^4);
    % Torque per segment
    % end
    % Thrust=sum(dT(i,:)); % Total Thrust Force
    % Q=sum(dQ(i,:)); % Total Torque of blade
    % Power_Shroud=w*Q;
    % Cw_shroud=Power_Shroud/(0.5*p*A*(uinf^3));
%% Averaged Axial and Angular Induction Factors (for improved convergence)
    a(i+1,:)=(a(i,:)+a(i-1,:))./2;
    aprime(i+1,:)=(aprime(i,:)+aprime(i-1,:))./2;
%% Convergence Checks and Breaks
    aTol=abs((a(i+1,1:N)-a(i,1:N))); aTol_all=all(aTol<Tol);
    aprimeTol=abs(aprime(i+1,1:N)-aprime(i,1:N)); aprimeTol_all=all(aprimeTol<Tol);
    phi_imaginary=not(isreal(phi(i,:)));
    Ct_Tol=Ct(i,:); CtTol=any(Ct_Tol<0);
    if aTol_all==1 && aprimeTol_all==1 || CtTol==1 || isreal(phi(i,:))<1 || i >= maxit, break,end
end
%% BEM Figures
figure(1)
subplot(1,3,1)
plot(r_R(1:N),phi(i,1:N),r_R(1:N),alpha(i,1:N),'--',r_R(1:N),pitch(1,1:N))
%title('Angles of Blade')
ylabel('Phi, Alpha, Pitch (degrees)')
xlabel('r/R')
legend('Phi','Alpha','Pitch')
subplot(1,3,2)
plot(r_R(1:N-1),a(i,1:N-1),r_R(1:N-1),aprime(i,1:N-1),r_R(1:N-1),Ct(i,1:N-1))
%title('Design Parameters of Blade')
ylabel('a, aprime, Ct')
xlabel('r/R')
legend('a','aprime','Ct')
subplot(1,3,3)
plot(r_R(1:N-1),cl(i,1:N-1),r_R(1:N-1),cd(i,1:N-1),'--')

```

```

%title('Lift and Drag Coefficients')
ylabel('Lift, Drag')
xlabel('r/R')
legend('Lift','Drag')
%% Power Comparison
Urange=linspace(4,8);
%Bare
Power_Bare=Cw_bare.*0.5.*p*A.*(Urange.^3);
Power_Bare_Actual=0.35.*0.5.*p*A.*(Urange.^3);
figure(2)
subplot(1,2,1)
plot(Urange,Power_Bare,Urange,Power_Bare_Actual)
%title('Power')
ylabel('Power (Watts)')
xlabel('Wind Speed (m/s)')
legend('Bare Wind Turbine BEMT Calculation','Experimental')
%Shroud
%Power_Shroud_BEM=Cw_shroud.*0.5.*p*A.*(Urange).^3;
%Power_Actual= 2.5888.*Urange.^2 + 7.8225.*Urange - 46.299;
%subplot(1,2,2)
%plot(Urange,Power_Shroud_BEM,Urange,Power_Actual)
%title('Power')
%ylabel('Power (Watts)')
%xlabel('Wind Speed (m/s)')
%legend('Shrouded BEMT with SAF','Experimental')
%% Wind Speed Related Calculation Values
disp('iteration of convergence is'); disp(i)
%Bare
disp('For a bare wind turbine at a speed of'); disp(uinf)
disp('w for a bare wind turbine is'); disp(w/K)
disp('BEM Torque is'); disp(Q_bare)
disp('BEM Power is'); disp(BEM_Power_Bare)
%Shroud at multiple speeds
%disp('For a shrouded wind turbine at a wind speed of'); disp(uinf)
%disp('w is'); disp(w)
%disp('BEM Torque is'); disp(Q)
%disp('BEM Power is'); disp(Power_Shroud)
dr=r(1,2)-r(1,1); disp('segment thickness is'); disp(dr)
%% Generate Plot of Blade Coordinates
figure(3)
x_63210_coordinates=[0 0.0057 0.00831 0.01338 0.02602 0.05114 0.07618 0.10118 0.1511
0.20098 0.25083 0.30067 0.35049 0.40032 0.45015 0.5 0.54987 0.58976 0.64968 0.69964
0.74962 0.79964 0.8497 0.89979 0.9499 1 0.9501 0.90021 0.8503 0.80036 0.75038 0.70036
0.65032 0.60024 0.55013 0.5 0.44985 0.39968 0.34951 0.29933 0.24917 0.19902 0.1489
0.09882 0.07382 0.04886 0.02398 0.01162 0.00669 0.0043 0];

```

```

y_63210_coordinates=[0 -0.00776 -0.00967 -0.01165 -0.01567 -0.02121 -0.02524 -
0.02843 -0.03319 -0.03648 -0.03857 -0.03966 -0.0397 -0.03867 -0.03671 -0.03393
-0.03045 -0.02644 -0.02204 -0.0174 -0.01271 -0.00822 -0.00415 -0.00087 0.0012
0 0.0053 0.01212 0.01761 0.02414 0.03061 0.03684 0.04264 0.04786 0.05235 0.05599
0.05861 0.06009 0.0603 0.0591 0.05647 0.0524 0.04665 0.03877 0.03372 0.02753 0.01939
0.01379 0.01107 0.00876 0];
JJ=size(x_63210_coordinates);
ZZZZ=JJ(1,2);
%Generate Points of blade
TTT1=1;
TTT2=2;
TTT3=3;
for T=1:N
    if T==1
        TTT1=1;
        TTT2=2;
        TTT3=3;
    else
        TTT1=TTT1+3;
        TTT2=TTT2+3;
        TTT3=TTT3+3;
    end
    X(T,:)=c(1,T).*x_63210_coordinates -.25.*c(1,T); %align blade center according to 0.25 chord
length
    Y(T,:)=c(1,T).*y_63210_coordinates;
    Z(T,:)=r(1,T).*ones(1,ZZZZ);
    X1(T,:)=X(T,:).*cosd(-pitch(1,T))+Y(T,:).*sind(-pitch(1,T));
    Y1(T,:)=X(T,:).*sind(-pitch(1,T)) +Y(T,:).*cosd(-pitch(1,T));
    Z1(T,:)=Z(T,:);
    scatter3(X1(T,:),Y1(T,:),Z1(T,:),'black')
    Final_Blade(:,TTT1:TTT3)=[transpose(X1(T,:)),transpose(Y1(T,:)),transpose(Z1(T,:))];
    hold on
    axis([-0.05 .1 -0.05 .05 0 .36])

%Create text files
File_name = ['Segment_lower' sprintf('%1.0f',T) '.txt'];
Segment_Coordinates_lower=Final_Blade(1:26,TTT1:TTT3);
dlmwrite(File_name,Segment_Coordinates_lower,'delimiter','\t', 'newline','pc')
File_name = ['Segment_upper' sprintf('%1.0f',T) '.txt'];
Segment_Coordinates_upper=Final_Blade(26:51,TTT1:TTT3);
dlmwrite(File_name,Segment_Coordinates_upper,'delimiter','\t', 'newline','pc')
end

```

System Output:

iteration of convergence is 19

For a bare wind turbine at a speed of 6

w for a bare wind turbine is

72.000000000000014

BEM Torque is 0.2358815395

BEM Power is 16.9837084

segment thickness is 0.005506122448980

Output plots are included in Chapter 2 section 2.2.

Bibliography

- Abbott, Ira, Von Doenhoff, Albert, Stivers, L. (1945). *Report No. 824 Summary of Airfoil Data*. Langley Field. Retrieved from <https://ntrs.nasa.gov/archive/nasa/casi.ntrs.nasa.gov/19930090976.pdf>
- Abe, K. I., & Ohya, Y. (2004). An investigation of flow fields around flanged diffusers using CFD. *Journal of Wind Engineering and Industrial Aerodynamics*, 92(3–4), 315–330. <https://doi.org/10.1016/j.jweia.2003.12.003>
- Abe, K., Nishida, M., Sakurai, A., Ohya, Y., Kihara, H., Wada, E., & Sato, K. (2005). Experimental and numerical investigations of flow fields behind a small wind turbine with a flanged diffuser. *Journal of Wind Engineering and Industrial Aerodynamics*, 93(12), 951–970. <https://doi.org/10.1016/j.jweia.2005.09.003>
- Alam, F., & Golde, S. (2013). An aerodynamic study of a micro scale vertical axis wind turbine. *Procedia Engineering*, 56, 568–572. <https://doi.org/10.1016/j.proeng.2013.03.161>
- Ali, A., Alam, F., Djamovski, V., Watkins, S. (2011). A review of power generation from wind in Australia. *Proceedings of the 9th International Conference of Mechanical Engineering (ICME2011)*.
- ANSYS Inc. (2011). ANSYS-FLUENT Theory Guide, 15317(November), 724–746.
- Aranake, A. C., Lakshminarayan, V. K., & Duraisamy, K. (2015). Computational analysis of shrouded wind turbine configurations using a 3-dimensional RANS solver. *Renewable Energy*, 75, 818–832. <https://doi.org/10.1016/j.renene.2014.10.049>
- Balduzzi, F., Bianchini, A., Carnevale, E. A., Ferrari, L., & Magnani, S. (2012). Feasibility analysis of a Darrieus vertical-axis wind turbine installation in the rooftop of a building. *Applied Energy*, 97, 921–929. <https://doi.org/10.1016/j.apenergy.2011.12.008>

- Barth, T. , Jespersen, D. (1989). The design and application of upwind schemes on unstructured meshes. *27th Aerospace Sciences Meeting*. <https://doi.org/10.2514/6.1989-366>
- Bazilevs, Y., Hsu, M.-C., Akkerman, I., Wright, S., Takizawa, K., Henicke, B., ... Tezduyar, T. E. (2011). 3D simulation of wind turbine rotors at full scale. Part I: Geometry modeling and aerodynamics. *International Journal for Numerical Methods in Fluids*, *65*(1–3), 207–235. <https://doi.org/10.1002/flid.2400>
- Bet, F., & Grassmann, H. (2003). Upgrading conventional wind turbines. *Renewable Energy*, *28*(1), 71–78. [https://doi.org/10.1016/S0960-1481\(01\)00187-2](https://doi.org/10.1016/S0960-1481(01)00187-2)
- Bird, R. Byron, Warren E. Stewart, E. N. L. (2007). *Transport Phenomena: Revised Second Edition*. *Transport Phenomena: Revised Second Edition*.
- Chen, J., Yang, H., Yang, M., Xu, H., & Hu, Z. (2015). A comprehensive review of the theoretical approaches for the airfoil design of lift-type vertical axis wind turbine. *Renewable and Sustainable Energy Reviews*, *51*, 1709–1720. <https://doi.org/10.1016/j.rser.2015.07.065>
- De Kooning, J. D. M., Vandoorn, T. L., Van de Vyver, J., Meersman, B., & Vandeveldel, L. (2016). Displacement of the maximum power point caused by losses in wind turbine systems. *Renewable Energy*, *85*, 273–280. <https://doi.org/10.1016/j.renene.2015.06.052>
- Drela, M., Youngren, H. (2000). XFOIL Airfoil Development System. Retrieved January 8, 2017, from <http://web.mit.edu/drela/Public/web/xfoil/>
- Eriksson, S., Bernhoff, H., & Leijon, M. (2008). Evaluation of different turbine concepts for wind power. *Renewable and Sustainable Energy Reviews*, *12*(5), 1419–1434. <https://doi.org/10.1016/j.rser.2006.05.017>
- Gaden, D. L. F., & Bibeau, E. L. (2010). A numerical investigation into the effect of diffusers on

- the performance of hydro kinetic turbines using a validated momentum source turbine model. *Renewable Energy*, 35(6), 1152–1158. <https://doi.org/10.1016/j.renene.2009.11.023>
- Gilbert, B.L., Oman, R.A., Foreman, K. M. (1978). Fluid dynamics of diffuser-augmented wind turbines. *Journal of Energy*, 2(No. 6), 368–374.
- Gilbert, B. L., & Foreman, K. M. (1983). Experiments With a Diffuser-Augmented Model Wind Turbine. *Journal of Energy Resources Technology*, 105(1), 46.
<https://doi.org/10.1115/1.3230875>
- Global Wind Energy Council. (2018). *Global Wind Statistics 2017*. Brussels. Retrieved from http://gwec.net/wp-content/uploads/vip/GWEC_PRstats2017_EN-003_FINAL.pdf
- Grauers, A. (1996). Efficiency of three wind energy generator systems. *IEEE Transactions on Energy Conversion*, 11(3), 650–655. <https://doi.org/10.1109/60.537038>
- Hansen, M., Sorensen, J., Michelsen, J., Sorensen, N., Hansen, M., Sorensen, J., ... Sorensen, N. (1997). A global Navier-Stokes rotor prediction model. *35th Aerospace Sciences Meeting and Exhibit*. <https://doi.org/10.2514/6.1997-970>
- Hsiao, F.-B., Bai, C.-J., & Chong, W.-T. (2013). The Performance Test of Three Different Horizontal Axis Wind Turbine (HAWT) Blade Shapes Using Experimental and Numerical Methods. *Energies*, 6(6), 2784–2803. <https://doi.org/10.3390/en6062784>
- Igra, O. (1981). Research and development for shrouded wind turbines. *Energy Conversion and Management*, 21(1), 13–48. [https://doi.org/10.1016/0196-8904\(81\)90005-4](https://doi.org/10.1016/0196-8904(81)90005-4)
- Ilk, R. (1947). *High-speed aerodynamic characteristics of four thin naca 63-series airfoils*. Moffett Field.
- Innovations | Offshore Wind Turbines | MHI Vestas™. (2018). Retrieved March 5, 2018, from <http://www.mhivestasoffshore.com/innovations/>

- Inoue, M., Sakurai, A., & Ohya, Y. (2002). A Simple Theory of Wind Turbine with Brimmed Diffuser. *Turbomachinery International*, 30(8), 497–502 (in Japanese).
- Jonkman, J., Butterfield, S., Musial, W., & Scott, G. (2009). Definition of a 5-MW Reference Wind Turbine for Offshore System Development, (February).
<https://doi.org/10.2172/947422>
- Kosasih, B., & Tondelli, A. (2012). Experimental study of shrouded micro-wind turbine. *Procedia Engineering*, 49, 92–98. <https://doi.org/10.1016/j.proeng.2012.10.116>
- Krishnan, A., & Paraschivoiu, M. (2016). 3D analysis of building mounted VAWT with diffuser shaped shroud. *Sustainable Cities and Society*, 27, 160–166.
<https://doi.org/10.1016/j.scs.2015.06.006>
- Lanzafame, R., Mauro, S., & Messina, M. (2016). Numerical and experimental analysis of micro HAWTs designed for wind tunnel applications. *International Journal of Energy and Environmental Engineering*, 7(2), 199–210. <https://doi.org/10.1007/s40095-016-0202-8>
- Launder, B. E. (1972). The Prediction of Laminarization With A Two-Equation Model of Turbulence, 15, 301–314.
- Launder, B. E., & Spalding, D. B. (1972). Lectures in Mathematical Modeling of Turbulence. *Academic Press, London England*.
- Leonard, B., & Mokhtari, S. (1990). ULTRA-SHARP nonoscillatory convection schemes for high-speed steady multidimensional flow. *NASA Technical Memorandum*, (April).
- Lilley, G. M., & Rainbird, W. J. (1956). *A Preliminary Report on the Design and Performance of a Ducted Windmill. Report No. 102*. Crainfield, England.
- Liu, S., & Janajreh, I. (2012). Development and application of an improved blade element momentum method model on horizontal axis wind turbines. *International Journal of Energy*

- and Environmental Engineering*, 3(1), 30. <https://doi.org/10.1186/2251-6832-3-30>
- Malalasekera, W., & Versteeg, H. K. (2006). *An Introduction to Computational Fluid Dynamics - The Finite Volume Method*. *AIAA Journal* (Vol. 44). <https://doi.org/10.2514/1.22547>
- Mansour, K., & Meskinkhoda, P. (2014). Computational analysis of flow fields around flanged diffusers. *Journal of Wind Engineering and Industrial Aerodynamics*, 124, 109–120. <https://doi.org/10.1016/j.jweia.2013.10.012>
- Manwell, J.F., McGowan, J.G., Rogers, A. L. (2002). *Wind Energy Explained* (Vol. 2). Amerst: John Wiley & Sons, Ltd.
- Menter, F. R. (1994). Two-equation eddy-viscosity turbulence models for engineering applications. *AIAA Journal*, 32(8), 1598–1605. <https://doi.org/10.2514/3.12149>
- Menter, F. R., Kuntz, M., & Langtry, R. (2003). Ten Years of Industrial Experience with the SST Turbulence Model. *Turbulence Heat and Mass Transfer* 4, 4, 625–632. <https://doi.org/10.4028/www.scientific.net/AMR.576.60>
- Mertens, S. (2003). The Energy Yield of Roof Mounted Wind Turbines. *Wind Engineering*, 27(6), 507–518. <https://doi.org/10.1260/030952403773617472>
- Millennium Wind Turbine. (2015). Retrieved April 9, 2018, from <http://hallmarkemporium.com/>
- NACA 63-210 AIRFOIL (n63210-il). (2018). Retrieved March 5, 2017, from <http://airfoiltools.com/airfoil/details?airfoil=n63210-il>
- Nini, M., Motta, V., Bindolino, G., & Guardone, A. (2014). Three-dimensional simulation of a complete Vertical Axis Wind Turbine using overlapping grids. *Journal of Computational and Applied Mathematics*, 270, 78–87. <https://doi.org/10.1016/j.cam.2014.02.020>
- Ohya, Y., Karasudani, T., Sakurai, A., Abe, K. ichi, & Inoue, M. (2008). Development of a shrouded wind turbine with a flanged diffuser. *Journal of Wind Engineering and Industrial*

- Aerodynamics*, 96(5), 524–539. <https://doi.org/10.1016/j.jweia.2008.01.006>
- Ohya, Y., Karasudani, T., Sakurai, A., & Inoue, M. (2004). Development of High-Performance Wind Turbine with a Brimmed-Diffuser : Part 2. *Journal of the Japan Society for Aeronautical and Space Sciences*, 52(604), 210–213. Retrieved from <http://ci.nii.ac.jp/naid/10012934634>
- PEXELS. (2018). PEXELS. Retrieved September 4, 2018, from <https://www.pexels.com/photo/renewable-energy-wind-generator-wind-turbine-environment-8546/>
- Phillips, D. G., Flay, R. G. J., & Nash, T. A. (1999). Aerodynamic analysis and monitoring of the Vortec 7 diffuser-augmented wind turbine. *IPENZ Transactions*, 26(1/EMCh), 13–19.
- Pope, K., Rodrigues, V., Doyle, R., Tsopeles, A., Gravelins, R., Naterer, G. F., & Tsang, E. (2010). Effects of stator vanes on power coefficients of a zephyr vertical axis wind turbine. *Renewable Energy*, 35(5), 1043–1051. <https://doi.org/10.1016/j.renene.2009.10.012>
- Riegler, H. (2003). HAWT versus VAWT. *Refocus*, 4(4), 44–46. [https://doi.org/10.1016/S1471-0846\(03\)00433-5](https://doi.org/10.1016/S1471-0846(03)00433-5)
- Sky Harvest to acquire vertical axis wind turbine technology and manufacturing facilities. (2013). Retrieved April 9, 2018, from <http://theprospectornews.com/?p=3591>
- Snel, H. (2003). Review of aerodynamics for wind turbines. *Wind Energy*, 6(3), 203–211. <https://doi.org/10.1002/we.97>
- Song, Y., & Perot, J. B. (2015). CFD Simulation of the NREL Phase VI Rotor. *Wind Engineering*, 39, 299–310. <https://doi.org/10.1260/0309-524X.39.3.321>
- Sorensen, N., & Hansen, M. (1998). Rotor performance predictions using a Navier-Stokes method. *1998 ASME Wind Energy Symposium*. <https://doi.org/10.2514/6.1998-25>

- Spalart, P., & Allmaras, S. (1992). A one-equation turbulence model for aerodynamic flows. *30th Aerospace Sciences Meeting and Exhibit*. <https://doi.org/10.2514/6.1992-439>
- Tamura, J. (2012). Wind Energy Conversion Systems. <https://doi.org/10.1007/978-1-4471-2201-2>
- Thé, J., & Yu, H. (2017). A critical review on the simulations of wind turbine aerodynamics focusing on hybrid RANS-LES methods. *Energy*, *138*, 257–289. <https://doi.org/10.1016/j.energy.2017.07.028>
- The Benefits of the Helix Wind Turbine - UAT Group. (n.d.). Retrieved April 9, 2018, from <http://uatgroup.com/the-benefits-of-the-helix-wind-turbine/>
- Tu, J., Yeoh, G. H., & Liu, C. (2012). *Computational fluid dynamics : a practical approach*. Elsevier/Butterworth-Heinemann.
- University of Illinois at Urbana-Champaign. (2018). UIUC Airfoil Data Site. Retrieved March 5, 2018, from <http://m-selig.ae.illinois.edu/ads/coord/n63210.dat>
- White, F. M. (2003). *Fluid mechanics*. McGraw-Hill.
- Wilcox, D. C. (1998). *Turbulence modeling for CFD*. Aiaa (2nd ed., Vol. 93). <https://doi.org/0963605151>
- You, J., Yu, D., & Kwon, O. (2013). Effect of turbulence models on predicting HAWT rotor blade performances. *Journal of Mechanical Science and Technology*. Retrieved from <http://link.springer.com/article/10.1007/s12206-013-0916-y>
- Zhu, W. J., Shen, W. Z., & Sørensen, J. N. (2014). Integrated airfoil and blade design method for large wind turbines. *Renewable Energy*, *70*, 172–183. <https://doi.org/10.1016/j.renene.2014.02.057>

Curriculum Vitae

Andrew L. Poland

andrewliampoland@gmail.com

EDUCATION

- 8/25/15-05/15/18 **Master of Science in Mechanical Engineering**
University of Nevada Las Vegas
- 8/23/10-12/16/14 **Bachelor of Science, Mechanical Engineering,**
University of Nevada Las Vegas

SKILLS & CERTIFICATES

- Passed Fundamentals of Engineering Exam
- Microsoft Office products
- MATLAB[®], SolidWorks[®]
- ANSYS (Certificate from Cornell University for ANSYS Course)

EXPERIENCE

- 8/28/17-05/15/18 **Graduate Assistant, University of Nevada, Las Vegas**
- ME 337 Lab instructor
 - ME 421 Lab instructor, grader and tutor for ME 453
- 6/05/17-7/10/17 **Graduate Assistant, University of Nevada, Las Vegas**
- Former instructor for a CAD course using SolidWorks[®]
- 1/19/16-5/19/17 **Graduate Assistant, University of Nevada, Las Vegas**
- Former instructor for two Engineering Measurements Lab courses
 - Former instructor for an Automatic Controls Lab.
 - Graded and tutored for Vibrations and Aerodynamics courses.
- 4/06/15-12/18/15 **Engineering Intern, IMI Precision Engineering-Norgren Kloehn**
- Created diagrams and tools in support of engineers.
 - Developed work instructions for an assembly line.
 - Assisted with design and product performance calculations.
 - Participated in the creation of processes and documentation for production projects.
 - Involved in design verification and validation activities.

ENGINEERING PROJECTS

Senior Design Project, Axial Toothbrush

- The project consisted of designing and fabricating a toothbrush that rotates in an axial direction.
- In charge of design and fabrication of the device. Most of the parts were made with the use of a 3D printer. Some parts needed to be machined using a lathe, drill press, and band saw.

Mechanical Engineering Design Project, Robotic Lift Mechanism

- The group project consisted of designing a robot that could compete in a 2013-2014 FTC robotics competition and constructing the main scoring element of the robot.
- In charge of design and fabrication of the device and involved with the cad modeling of the robot.

ORGANIZATIONS

Tau Beta Pi Engineering Honor Society

- Current Graduate Advisor, former Vice President
- Involved in helping organize multiple member events.

American Society of Mechanical Engineers

- Former Treasurer
- Volunteer for various events including ASME EFest West 2017 that was held at UNLV.
- Intimately involved in fundraising for the ASME student chapter at UNLV where I helped raised \$5700 in funds for a human powered vehicle project that competed in an ASME HPVC West Competition.

PRESENTATIONS

4-24-17

College of Engineering Graduate Celebration Poster Competition